國 立 交 通 大 學

電信工程研究所

博 士 論 文

使用超穎材質以降低特定吸收比及交互方向內隱式時域有限差分法之穩定度改善

SAR Reduction with Metamaterials and Stability Improvement of ADI-FDTD

研 究 生：黃 竣 南

指導教授：鍾世忠

中 華 民 國 100 年 10 月

使用超穎材質以降低特定吸收比及交互方向內隱式時域有限差分法之穩定度改善

SAR Reduction with Metamaterials and Stability Improvement of ADI-FDTD

研究生： 黃竣南　　Student: Jiunn-Nan Hwang

指導教授：鍾世忠 博士　Advisor: Dr. Shyh-Jong Chung

國立交通大學

電信工程研究所

博士論文

A Dissertation
Submitted to Department of Communication Engineering
College of Electrical and Computer Engineering
National Chiao Tung University
in Partial Fulfillment of the Requirements
for the Degree of Doctor of Philosophy
in
Communication Engineering
Hsinchu, Taiwan

2011 年 10 月

摘要

目前行動通訊裝置使用人數日與俱增，而人們也開始關心手機電磁輻射對人體的影響。其中，藉由特定吸收效率可以瞭解人頭電磁能量吸收的多寡。目前，時域有限差分法已應用於人頭特定吸收效率的計算。最近，超穎材質由於具有特殊物理特性而引起研究人員對其興趣。超穎材質為人造材質，由於其介電係數與導磁係數為負值，因此超穎材質電磁傳輸特性不同於一般材質。

在本研究中，我們將使用超穎材質以減低人頭與天線間交互電磁現象。首先，我們利用時域有限差分法結合 Drude 模型來模擬超穎材質。在模擬中，超穎材質置於天線與人頭間。從模擬結果可知，藉由擺放超穎材質可以有效減低人頭的特定吸收效率。我們也探討擺放超穎材質對於天線影響。藉由適當擺放超穎材質，超穎材質對於天線輻射能量和天線場型影響不大。而我們進一步探討擺放位置，尺寸大小，超穎材質介質係數對於減低特定吸收效率的影響。超穎材質可以藉由設計分離式環形共振器來實現。在本研究中，我們設計分離式環形共振器，使其工作頻率為 900 MHz 和 1800 MHz。設計流程也將詳細描述。我們將設計的分離式環形共振器置於天線與介質體中間，從結果可以發現介質體的特定吸收效率將會減低。此研究可以提供減低特定吸收效率的方法。

在研究中，我們也發展無條件穩定 ADI-FDTD 模擬方法。我們發現，當使用吸收邊界於 ADI-FDTD 時，可能會造成演算法不穩定問題。首先，我們探討 Mur 吸收邊界於 ADI-FDTD 的數值穩定分析。在此演算法中，電磁波傳播方向將會影響該演算法穩定度。從模擬結果可知，該演算法只有在波行進方向為 0 度，45 度，90 度時會穩定。我們也推導出該演算法數值色散關係式。發現此演算法數值不穩定是無法改善。接著，我們探討應用分離場完美匹配層於 ADI-FDTD 的穩定度分析。穩定度理論分析可以藉由推導穩定矩陣實現。我們發現應用分離場完美匹配層於 ADI-FDTD 會造成數值不穩定結果。完美匹配層中電導會影響該演算法穩定度。因此，我們提出改良完美匹配層電導，以改善該演算法穩定度。最後藉由數值模擬可以驗證分離場完美匹配層和 Mur 吸收邊界於 ADI-FDTD 的數值不穩定效應。CN-FDTD 為另一種無條件穩定演算法。ADI-FDTD 與 CN-FDTD 差別只是二階近似項。在本研究中，我們將分析分離場完美匹配層，非分離場完美匹配層，複數頻率轉換完美匹配層對於 ADI-FDTD 與 CN-FDTD 的影響。我們發現 ADI-FDTD 不穩定是二階近似項所造成。藉由此研究可以提供未來發展應用於 ADI-FDTD 簡潔穩定的完美匹配層。由於在 ADI-FDTD 中，其時間步階不受穩定法則限制，故該演算法非常適合模擬超大型積體電路。藉由改良完美匹配層，我們發現所提出的演算法可以有效率以及準確模擬超大型積體電路時域與頻域電磁特性。

在多天線系統中，增加天線隔絕度為重要參數。在本研究中，藉由在兩天線間增加一耦合元件，可以有效增加隔絕度。此耦合元件優點為不增加額外天線面積。在研究中，耦合元件尺寸對於天線隔絕度效率與共振頻率也將做進一步探

討，經由天線量測結果，所提出的耦合元件可以增加天線 15dB 的隔絕度，增加耦合元件對於天線場型亦只有減少 1dB 增益以內的影響

Abstract

The use of the mobile devices has been growing rapidly in the global communities. The influence of electromagnetic (EM) waves from cellular phones on the human head has been widely discussed recently. The specific absorbing rate (SAR) is a defined parameter for evaluating power deposition in human tissue. The finite-difference time-domain (FDTD) is widely used to study the peak SAR in the human head. Recently, metamaterials have inspired great interests in their unique physical properties and novel application. Metamaterials denote artificially constructed materials having electromagnetic properties not general found in nature. Two important parameters, electric permittivity and magnetic permeability determine the response of the materials to the electromagnetic propagation.

In this work, we use the metamaterials to reduce the EM interaction between the antenna and human head. Preliminary simulation of metamaterials is performed by FDTD method with lossy Drude model. The metamaterials are placed between the antenna and human head. From the simulation result, it is found that the peak SAR in the human head can be reduced with the placement of metamaterials. We also study the antenna performance with metamaterials. The antenna radiated power and antenna pattern can be less affected with placement of metamaterials properly. The effects of placement position of metamaterials, metamaterials size, and the medium parameters of metamaterials on the SAR reduction effectiveness are investigated. The metamaterials can be constructed from split ring resonators (SRRs). In this work, we also design the SRRs operated at 900 MHz and 1800 MHz. The design procedure of the SRRs is described. The designed SRRs are placed between the antenna and a dielectric cube. It is found that the peak SAR in the dielectric cube is reduced significantly. This study can provide useful methodology for SAR reduction.

In this work, we develop the alternating direction implicit (ADI) finite-difference time-domain (FDTD) method. However, when employing the absorbing boundary conditions (ABCs) for ADI-FDTD method, this scheme can lead to instability. First, the stability analysis of the Mur's ABC for ADI-FDTD method is also studied. The effect of the wave propagation direction on the stability of this scheme is investigated. It is found that this scheme can be stable only when the incident wave directions are 0 degree, 45 degree, and 90 degree. We also derive the dispersion relation of this scheme. The instability of this scheme can not be avoided. Then, the stability analysis of split-field perfectly matched layer (PML) for ADI-FDTD is studied. The theoretical stability analysis of this scheme is performed by deriving the amplification matrix. It is found that the split-field PML scheme for ADI-FDTD method will be unstable. The effect of the PML conductivity profile on the stability of this scheme is studied. We

propose the modified PML conductivity profile to improve the stability of this scheme. Finally, numerical simulations are performed to validate the instability of the split-field PML and Mur's ABC for ADI-FDTD method.

The Crank-Nicolson FDTD (CN-FDTD) is also an unconditionally stable scheme. The difference between the ADI-FDTD and CN-FDTD is the second order perturbation term. In this work, the stability analysis of split-field PML and unsplit-field PML for ADI-FDTD and CN-FDTD are studied. It is found that the instability of PML schemes for ADI-FDTD is due to the perturbation term. This study can provide information to develop a simple and stable PML scheme for ADI-FDTD in future work.

The ADI-FDTD can simulate the VLSI circuits effectively since the time step is not restricted by the Courant stability condition. The modified PML scheme for ADI-FDTD method is employed to simulate the VLSI circuits. It is found that the proposed scheme can model the time domain and frequency domain electromagnetic characteristics of VLSI circuits accurately and effectively.

A coupling element to enhance the isolation between two closely packed antennas for 2.4 GHz wireless local area network (WLAN) application is introduced. The proposed structure occupies two antenna elements and a coupling element in between. By putting a coupling element which artificially creates an additional coupling path between the antenna elements, the antenna isolation can be enhanced. The advantage of this design is that no extra space is needed for antenna elements. With the proposed design, more than 15 dB isolation can be achieved for two parallel individual planar inverted F antennas (PIFAs) with 5 mm spacing. Parametric studies for the design are also included to show how to increase isolation bandwidth and control the isolation frequency.

誌謝

首先感謝指導教授鍾世忠博士。在研究遇到瓶頸時，老師總能點出問題的關鍵，以整體觀念分析問題，而老師研究謹慎的態度，追根究柢的精神，讓我更瞭解自己的不足，與老師討論總讓我獲益良多。在這裡也要特別感謝陳富強教授。在第三章和第四章的內容中，對於超穎材質的特性研究與時域有限差分法的穩定性分析，陳老師皆提供許多建議與方向，在超穎材質研究中，在眾多超穎材質中，陳老師根據經驗提出可能應用於電磁吸收降低的超穎材質，進一步也協助人頭模型取得，使研究能順利進行。在第四章 ADI-FDTD 穩定度研究中，與陳老師討論過程釐清數值不穩定的原因，並建議用 VLSI 電感做驗證，使研究更據說服力。而在論文後續修改中，陳老師也提供許多寶貴意見，使論文能順利發表，特別感謝陳老師的幫助。在此也感謝口試委員對於論文建議與指導，使本論文能更加完整。

在這邊特別感謝老婆肖真一路支持與天主的同在,使學業得以完成。

Contents

List of Figures

List of Tables

Chapter 1

Introduction

1.1 SAR Reduction with Metamaterials

The use of the cellular phones has been growing rapidly in the global communities. The absorption of EM energy emitted from cellular phone has been discussed in recent years. Exposure guidelines for protecting the human body from EM exposure have been issued in many countries. More and more people concern the absorption of electromagnetic radiation from cellular phone in the human head.

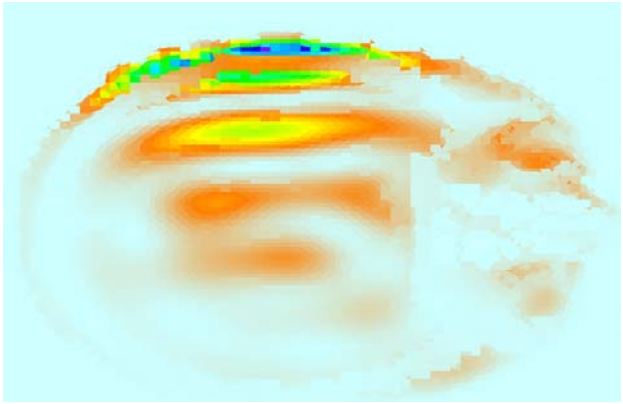

Figure 1.1.1 The SAR distribution in the human head

The specific absorption rate (SAR) is a defined parameter for evaluating power deposition in human tissue, as shown in Fig. 1.1.1. For the cellular phone compliance, the SAR value must not exceed the exposure guidelines [1, 2]. Some numerical results have implied that the peak 1 g averaged SAR value (SAR_{1g}) may exceed the exposure guidelines when a portable telephone is placed extremely close to the head [3, 4]. Therefore, many researchers are working on reducing the SAR values. In [5], a ferrite sheet was proposed to use as a protection attachment between the antenna and a head. It was found that a ferrite sheet can result in SAR reduction and the radiation pattern of the antenna can be less affected. In [6], a PEC reflector was arranged between a human head and the driver of a folded loop antenna. Numerical results showed that the radiation efficiency can be enhanced and the peak SAR value can be reduced. In [7], a study on the effects of attaching conductive materials to cellular phone for SAR reduction has been presented. It indicated that the position of the shielding material is

an important factor for SAR reduction effectiveness.

Recently, metamaterials have inspired great interests due to their unique physical properties and novel application [8, 9]. Metamaterials denote artificially constructed materials having electromagnetic properties not generally found in nature. Two important parameters, electric permittivity and magnetic permeability determine the response of the materials to the electromagnetic propagation. Mediums with negative permittivity can be obtained by arranging the metallic thin wires periodically [10]. On the other hand, an array of split ring resonators (SRRs) can exhibit negative effective permeability [11]. The metallic thin wires and split ring resonators are narrow-banded and lossy materials, as shown in Fig. 1.1.2.

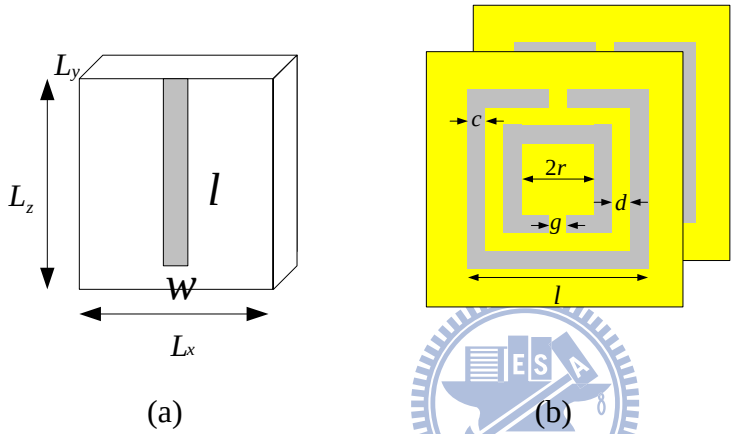

Figure 1.1.2 (a) thin wire structure (b) split-ring resonator (SRR).

When one of the effective medium parameters is negative and the other is positive, the medium will display a stop band. The metamaterials is on a scale less than the wavelength of radiation and uses low density of metal. The structures are resonant due to internal capacitance and inductance. The stop band of metamaterials can be designed at operation bands of cellular phone while the size of metamaterials is similar to that of cellular phone. In [12], the designed SRRs operated at 1.8 GHz were used to reduce the SAR value in a lossy material. The metamaterials are designed on circuit board so it may be easily integrated to the cellular phone. Simulation of wave propagation into metamaterials was proposed in [13]. The authors developed the FDTD method with lossy Drude models for metamaterials simulation. This method is a useful approach to study the wave propagation characteristics of metamaterials [14] and has been further developed with the perfectly matched layer and extended to three-dimension problem [15].

In this work, we will use metamaterials for SAR reduction. An anatomically based human head model and a dipole antenna are assumed. The metamaterials are placed between the antenna and a human head. Preliminary study of SAR reduction with

metamaterials is performed by 3-D FDTD method with lossy Drude model. In order to study SAR reduction of antenna operated at the GSM 900 band, the effective medium parameter of metamaterials is set to be negative at 900 MHz. Different positions, sizes, and negative medium parameters of metamaterials for SAR reduction effectiveness are also analyzed. To investigate the influence of metamaterials on the antenna, the peak SAR_{1g} and antenna performances are demonstrated. The use of metamaterials is also compared with other SAR reduction techniques. We design the metamaterials from periodically arrangement of split ring resonators (SRRs). By properly designing structure parameters of SRRs, the effective medium parameter can be negative around 900 MHz and 1800 MHz bands. The SAR value in a simplified muscle cube with the presence of SRRs is studied. Numerical results are demonstrated to validate the effect of SAR reduction with metamaterials.

1.2 Stability Analysis of Absorbing Boundary Conditions for ADI-FFDTD

Finite-Difference Time-Domain (FDTD) method has been widely used to analyze the electromagnetic problems [16, 17]. Due to the explicit nature of this method, the time step size is restricted by the Courant, Friedrichs, and Lewy (CFL) stability condition. Recently, a stable alternating direction implicit (ADI) scheme was introduced for the FDTD method. The ADI-FDTD method is an attractive method due to its unconditionally stability with large CFL number [18-21]. The flowchart of ADI-FDTD is shown in Fig. 1.2.1.

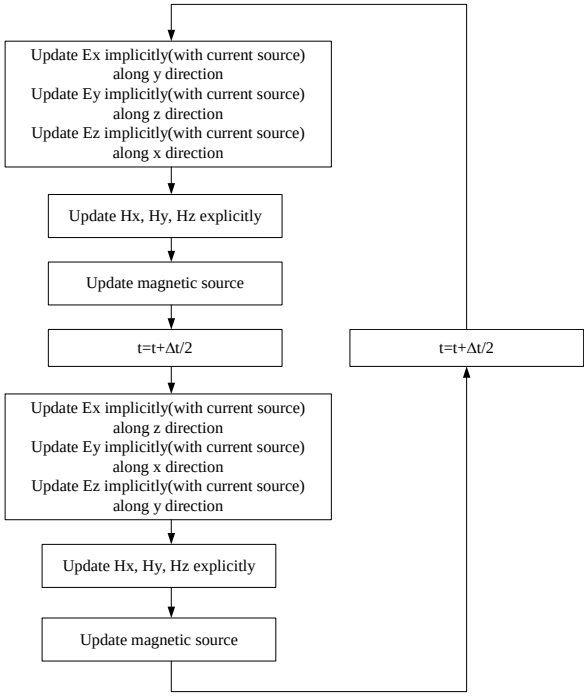

Figure 1.2.1 Flow chart of ADI-FDTD.

When the ADI-FDTD method is used to simulate unbounded region problems, efficient absorbing boundary conditions (ABCs) must be employed. The commonly used ABCs are Mur's first order ABC and perfectly matched layer (PML) medium. In [22, 23], the Mur's first order ABC was implemented in the ADI-FDTD method to simulate microstrip circuits. A split field PML [24] was employed for the ADI-FDTD method [25, 26]. However, the implementation of ABCs in the ADI-FDTD method can affect the stability of this scheme. For analytical ABCs, it is found that the implementation of the third order Higdon's ABC in the ADI-FDTD method will cause instability in the simulation results [27]. In [28, 29], it is found that the ADI-FDTD method with split-field PML will lead to late-time instability from numerical simulations. In [28], the authors indicate that the instability from the split-field PML equations can be prevented by using an unsplit form PML implementation. However, the split-field PML formulation is less complicated and more straightforward compared to the unsplit form PML implementation. Therefore, a more stable PML implementation for ADI-FDTD method is highly desirable.

It is important to analyze the stability of the absorbing boundary condition for the ADI-FDTD method. In this work, first, the stability analysis of the Mur's first order ABC in the ADI-FDTD method is demonstrated. The theoretical stability analysis of this scheme also is studied by deriving the amplification matrix. The effect of the wave propagation direction on the stability of this scheme is investigated. From the stability analysis, it is found that the ADI scheme of the Mur's first order ABC is unstable. Since we focus on analyzing the stability of the Murs' ABC at the boundary and do not consider the stability of the total computation domain, the proposed stability analysis is approximate. The stability analysis of the total computational domain can be accomplished by numerical simulation with a large number of time steps. In this work, the numerical tests of the ADI-FDTD method with Mur's ABC are performed. Numerical results of this scheme with different time step size will be demonstrated to validate the instability of this scheme.

Then, the theoretical stability analysis of the ADI-FDTD method with split-field PML will be studied through deriving the amplification matrix. The amplification matrix is derived using the actual updating equations of the field components. From the stability analysis, it is found that this scheme will be unstable at the PML interface and inside the PML regions. The effect of the PML conductivity profile on the stability of this scheme will be investigated [30]. We find that the instability of this scheme is due to the conductivities within the PML medium. The instability of this scheme inside the PML regions can be improved significantly with the modified PML conductivity profile. Numerical results of the 3-D ADI-FDTD method with split-field PML will be demonstrated to validate the theoretical results.

The ADI-FDTD method is an attractive method since the time step size is not restricted by the CFL condition. Therefore, this method can model the electromagnetic effects of the VLSI circuits efficiently. The frequency domain characteristics of the VLSI circuit can be obtained from the Fourier transform of the transient time domain waveform and it requires a large number of time steps to complete the simulation by FDTD method. This study will be difficult or even impossible due to the late-time instability of ADI-FDTD method with PML absorbing boundary condition. It is not apparent in the literature that anyone has studied the frequency domain characteristics of the VLSI circuits by the ADI-FDTD method with PML absorbing boundary condition.

The Crank-Nicolson FDTD (CN-FDTD) is found to be another alternative unconditionally stable FDTD method. The ADI-FDTD can be seen as an approximation of the CN-FDTD scheme [31]. In [32, 33], the CN -FDTD with split-field PML and nearly PML (NPML) were proposed. It is shown that the CN-FDTD can remain unconditionally stable with PML implementation. The stability analysis of the PML schemes for the CN-FDTD and ADI-FDTD will be studied. The Von Neumann analysis is used to determine the stability of these schemes. The difference between the CN-FDTD and ADI-FDTD is the Δt^2 perturbation term. From this study, it is found that the perturbation term will affect the stability of PML schemes for ADI-FDTD method. This study can provide information to improve the PML scheme for ADI-FDTD method.

In previous study [30], it is found that the PML conductivity profile will affect the stability of the ADI-FDTD method with Berenger's PML absorber. The modified PML conductivity profile is employed in this work to investigate the electromagnetic effects of the VLSI circuits in time domain and frequency domain. From the simulation results, it is found that the instability of this scheme can be improved with the modified PML conductivity profiles. Numerical simulations of the VLSI interconnect and RF inductor will be performed to show the efficiency and accuracy of the proposed scheme

1.3. Coupling element for antenna isolation enhancement

The isolation between antennas is a critical parameter in many practical applications such as antenna arrays, diversity antennas and also multiple input multiple output (MIMO) communication systems. However, when antennas are closely packed, strong mutual coupling will degrade radiation patterns and decrease antenna efficiency, which will cause deterioration in signal-to-noise ratio and signal to-interference-plus-noise ratio of the systems

In this work, we propose a new coupling element between the antennas in order to

create an additional coupling path for enhancing the isolation. The coupling element is placed between antennas and therefore no extra space is needed with this design. This coupling element is not physically connected to the antenna elements and is flexible for controlling the center frequency, bandwidth, and level of isolation. To demonstrate the idea, two antenna elements for using in 2.4 GHz WLAN band are studied. From this study, it is found that the design can achieve more than 15 dB isolation improvement with 5 mm antenna spacing. The detail parametric studies are provided, which show the design of the proposed structure.

1.4 Organization of the Dissertation

This dissertation is organized as follows: First, we will discuss FDTD modeling method and its algorithm in Chapter 2. The FDTD method can use to simulate the metamaterials, calculate the radiation pattern of the antenna affected by the metamaterials, and calculate the SAR values in the human head. In Chapter 3, we will employ the Drude model into FDTD to investigate the effect of the metamaterials on SAR reduction. The design concept of split ring resonators (SRRs) is introduced. With the use of periodical boundary condition and total field / scatter field FDTD schemes, we will design the SRRs to operate at 900MHz and 1800MHz. The SAR reduction with the designed SRRs will be demonstrated. In Chapter 4, the stability analysis of the absorbing boundary conditions (ABCs) for ADI-FDTD will be demonstrated. Theoretical stability analysis and numerical simulation of the split-field PML and Mur's ABC for ADI-FDTD method will be studied. The modified PML conductivity profile is proposed to improve the stability of the split-field PML scheme for ADI-FDTD. The CN-FDTD can remain stable with PML scheme. The difference between the ADI-FDTD and CN-FDTD is the perturbation term. With this modified PML scheme, the time domain and frequency domain characteristics of VLSI circuits will be investigated. In Chapter 5, a coupling element to enhance the isolation between two closely packed antennas for 2.4 GHz wireless local area network (WLAN) application is introduced. The proposed structure occupies two antenna elements and a coupling element in between. The advantage of this design is that no extra space is needed for antenna elements. The proposed coupling element for antenna isolation will be discussed. Conclusions are drawn in Chapter 6.

Chapter 2

FDTD Method

The finite difference time domain (FDTD) is widely used to simulate the electromagnetic problems. In this chapter, the basic FDTD algorithm is described. To simulate open region problems, the absorbing boundary condition (ABC) is employed for FDTD method. The commonly used ABCs include Mur's ABC and perfect matched layer (PML). With the implementation of near field to far field transformation algorithm, the FDTD method can simulate the radiation pattern of the antenna. The modeling of the lumped elements by FDTD method will also be discussed. Finally, the flow of the FDTD computation will be described.

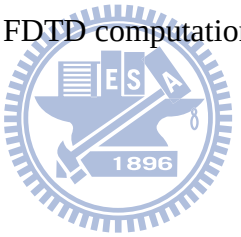

2.1 From Maxwell's Equations to FDTD Method.

We will derive the 3-D time domain Maxwell's equations to develop FDTD method. In this study, we consider the source free region with lossy electric and lossy magnetic mediums. To calculate the magnetic loss, the magnetic current density M is defined as

$$M = \rho' H \tag{2.1.1}$$

To calculate electric loss, we define the equivalent electric current J

$$J = \sigma E \tag{2.1.2}$$

The ρ' is magnetic resistivity and σ is the electric conductivity. From Maxwell's equations, we can obtain

$$\frac{\partial H}{\partial t} = -\frac{1}{\mu}\nabla \times E - \frac{\rho'}{\mu} H \tag{2.1.3}$$

$$\frac{\partial E}{\partial t} = \frac{1}{\varepsilon}\nabla \times H - \frac{\sigma}{\varepsilon} E \tag{2.1.4}$$

2.1.1 Three-dimension Electric and Magnetic Field Equations

Based on the equations (2.1.3) and (2.1.4), we can derive the 3-D electric and magnetic field equations.

$$\frac{\partial H_x}{\partial t} = -\frac{1}{\mu}\left(\frac{\partial E_y}{\partial z} - \frac{\partial E_z}{\partial y} - \rho' H_x\right) \tag{2.1.5}$$

$$\frac{\partial H_y}{\partial t} = -\frac{1}{\mu}\left(\frac{\partial E_z}{\partial x} - \frac{\partial E_x}{\partial z} - \rho' H_y\right) \tag{2.1.6}$$

$$\frac{\partial H_z}{\partial t} = -\frac{1}{\mu}\left(\frac{\partial E_x}{\partial y} - \frac{\partial E_y}{\partial x} - \rho' H_z\right) \tag{2.1.7}$$

$$\frac{\partial E_x}{\partial t} = \frac{1}{\varepsilon}\left(\frac{\partial H_z}{\partial y} - \frac{\partial H_y}{\partial z} - \sigma E_x\right) \tag{2.1.8}$$

$$\frac{\partial E_y}{\partial t} = \frac{1}{\varepsilon}\left(\frac{\partial H_x}{\partial z} - \frac{\partial H_z}{\partial x} - \sigma E_y\right) \tag{2.1.9}$$

$$\frac{\partial E_z}{\partial t} = \frac{1}{\varepsilon}\left(\frac{\partial H_y}{\partial x} - \frac{\partial H_x}{\partial y} - \sigma E_z\right) \tag{2.1.10}$$

The six field partial differential equations form the basic FDTD algorithms.

2.1.2 Finite Difference Method and Yee Algorithm

In this section, we will derive the FDTD method based on Yee algorithm [16]. In Yee algorithm, the derivatives of space and time are expressed by centre difference method. By applying the Yee algorithm for Maxwell's equations, the FDTD method

can be obtained. To begin the development of FDTD, we consider 1-D lossless condition as an example.

$$\frac{\partial H_y}{\partial t} = \frac{1}{\mu}\frac{\partial E_z}{\partial x} \tag{2.1.11}$$

According to a derivative definition, (2.1.11) can be written as

$$\lim_{\Delta t\to 0}\frac{\Delta H_y}{\Delta t} = \frac{1}{\mu}\lim_{\Delta x\to 0}\frac{\Delta E_z}{\Delta x} \tag{2.1.12}$$

We can note that the exact solution of (2.1.12) is (x, t)

Based on the Maxwell's equation, the derivatives of time and space in (2.1.12) are discretized by using centre difference expression, therefore we can obtain

$$\left.\frac{H_y(t_n+\Delta t/2)-H_y(t_n-\Delta t/2)}{\Delta t}\right|_{x_i} = \frac{1}{\mu}\left.\frac{E_z(x_i+\Delta x/2)-E_z(x_i-\Delta x/2)}{\Delta x}\right|_{t_n} \tag{2.1.13}$$

The solution of (2.1.13) is (x_i, t_n) and (x_i, t_n) will be close to (x, t).

Based on the FDTD method, the magnetic field $H_y(t_n+\frac{\Delta t}{2})$ can be expressed as

$$H_y(t_n+\Delta t/2)\big|_{x_i} = H_y(t_n-\Delta t/2)\big|_{x_i} + \frac{\Delta t}{\mu\Delta x}\left[E_z(x_i+\Delta x/2)-E_z(x_i-\Delta x/2)\right]\Big|_{t_n} \tag{2.1.14}$$

We denote i and n to express the space and time position, respectively. (2.1.14) can be further modified as

$$H_i^{n+1/2} = H_i^{n-1/2} + \frac{\Delta t}{\mu\Delta x}\left[E_{i+1/2}^{n} - E_{i-1/2}^{n}\right] \tag{2.1.15}$$

From (2.1.15), in order to calculate the magnetic field $H_i^{n+1/2}$, we need to obtain the same magnetic field in the earlier time step at the same location and the electric fields located at $\pm\Delta x/2$. Similarly, the electric field can be obtained as follow

$$E_{i+1/2}^{n+1} = E_{i+1/2}^{n} + \frac{\Delta t}{\varepsilon\Delta x}\left[H_{i+1}^{n+1/2} - H_i^{n+1/2}\right] \tag{2.1.16}$$

From (2.1.15) and (2.1.16), the electric and magnetic fields in the FDTD can be obtained from the fields in the earlier time step. The fields in space and time can be expressed as shown in Fig. 2.1.1.

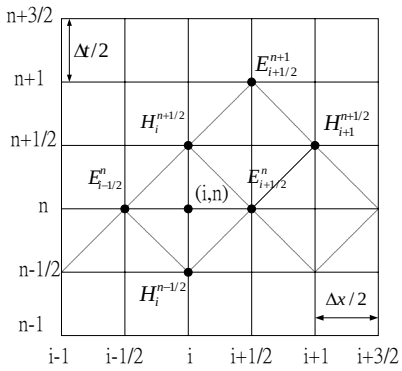

Figure 2.1.1 The fields in the space cell.

In (2.1.16), the time and space are variables. From (2.1.16), any 3-D location in the Yee cell can be expressed as

$$(i, j, k) = (i\Delta x, j\Delta y, k\Delta z) \tag{2.1.17}$$

Here, Δx, Δy, and Δz are space increment in *x*, *y*, and *z* direction.

We can define the function *u* in the space and time in the Yee cell as

$$u(i\Delta x, j\Delta y, k\Delta z, n\Delta z) = u_{i,j,k}^{n} \tag{2.1.18}$$

The Δt is time increment and *n* is an integer.

Based on the Yee algorithm, we can obtain the space derivative of *u* in the *x* direction

$$\frac{\partial}{\partial x}u(i\Delta x, j\Delta y, k\Delta z, n\Delta z) = \frac{u_{i+1/2,j,k}^{n} - u_{i-1/2,j,k}^{n}}{\Delta x} + O[(\Delta x)^2] \tag{2.1.19}$$

For time consideration, we can obtain the time derivative of *u*

$$\frac{\partial}{\partial t}u(i\Delta x, j\Delta y, k\Delta z, n\Delta z) = \frac{u_{i,j,k}^{n+1/2} - u_{i,j,k}^{n-1/2}}{\Delta t} + O[(\Delta t)^2] \tag{2.1.20}$$

In (2.1.19) and (2.1.20), $O[(\Delta x)^2]$ and $O[(\Delta t)^2]$ are error terms.

From previous study, it is found that the FDTD is based on the Maxwell's equation. For example, the field component H_x in space and time can be expressed as

$$\frac{H_x\big|_{i,j,k}^{n+1/2} - H_x\big|_{i,j,k}^{n-1/2}}{\Delta t} = \frac{1}{\mu_{i,j,k}}\left(\begin{array}{c} \dfrac{E_y\big|_{i,j,k+1/2}^{n} - E_y\big|_{i,j,k-1/2}^{n}}{\Delta z} \\ -\dfrac{E_z\big|_{i,j+1/2,k}^{n} - E_z\big|_{i,j-1/2,k}^{n}}{\Delta z} \\ -\rho'_{i,j,k} H_x\big|_{i,j,k}^{n} \end{array}\right) \tag{2.1.21}$$

However, there will be some computational calculation problem for $H_x\big|_{i,j,k}^{n}$ and $H_x\big|_{i,j,k}^{n+1/2}$ 、 $H_x\big|_{i,j,k}^{n-1/2}$. We can rewritten $H_x\big|_{i,j,k}^{n}$ as

$$H_x\big|_{i,j,k}^{n} = \frac{H_x\big|_{i,j,k}^{n+1/2} + H_x\big|_{i,j,k}^{n-1/2}}{2} \tag{2.1.22}$$

After substituting (2.1.22) into (2.1.21), we can obtain

$$H_x\big|_{i,j,k}^{n+1/2} - H_x\big|_{i,j,k}^{n-1/2} = \frac{\Delta t}{\mu_{i,j,k}} \left(\begin{array}{l} \dfrac{E_y\big|_{i,j,k+1/2}^{n} - E_y\big|_{i,j,k-1/2}^{n}}{\Delta z} \\ -\dfrac{E_z\big|_{i,j+1/2,k}^{n} - E_z\big|_{i,j-1/2,k}^{n}}{\Delta z} \\ -\rho'_{i,j,k} \dfrac{H_x\big|_{i,j,k}^{n+1/2} + H_x\big|_{i,j,k}^{n-1/2}}{2} \end{array} \right) \tag{2.1.23}$$

(2.1.23) can be further modified as

$$\begin{aligned} H_x\big|_{i,j,k}^{n+1/2} &= \left(\frac{1 - \dfrac{\rho'_{i,j,k}\Delta t}{2\mu_{i,j,k}}}{1 + \dfrac{\rho'_{i,j,k}\Delta t}{2\mu_{i,j,k}}} \right) H_x\big|_{i,j,k}^{n+1/2} \\ &+ \left(\frac{\dfrac{\Delta t}{\mu_{i,j,k}}}{1 + \dfrac{\rho'_{i,j,k}\Delta t}{2\mu_{i,j,k}}} \right) \left(\begin{array}{l} \dfrac{E_y\big|_{i,j,k+1/2}^{n} - E_y\big|_{i,j,k-1/2}^{n}}{\Delta z} \\ -\dfrac{E_z\big|_{i,j+1/2,k}^{n} - E_z\big|_{i,j-1/2,k}^{n}}{\Delta z} \end{array} \right) \end{aligned} \tag{2.1.24}$$

The electric fields E_x, E_y and E_z can be obtained by the same procedure. For example, the electric field E_z can be expressed as

$$\begin{aligned} E_z\big|_{i,j,k}^{n+1} = & \left(\frac{1 - \dfrac{\sigma_{i,j,k}\Delta t}{2\varepsilon_{i,j,k}}}{1 + \dfrac{\sigma_{i,j,k}\Delta t}{2\varepsilon_{i,j,k}}} \right) \cdot E_z\big|_{i,j,k}^{n} \\ & + \left(\frac{\dfrac{\Delta t}{\varepsilon_{i,j,k}}}{1 + \dfrac{\sigma_{i,j,k}\Delta t}{2\sigma_{i,j,k}}} \right) \cdot \left(\begin{array}{l} \dfrac{H_y\big|_{i+1/2,j,k}^{n+1/2} - H_y\big|_{i-1/2,j,k}^{n+1/2}}{\Delta x} \\ -\dfrac{H_x\big|_{i,j+1/2,k}^{n+1/2} - H_x\big|_{i,j-1/2,k}^{n+1/2}}{\Delta y} \end{array} \right) \end{aligned} \tag{2.1.25}$$

We can derive the six field components based on the FDTD method. The field components located in the Yee cell is shown in Fig. 2.1.2. It can be found that the electric field component is surrounded by the magnetic field components and the

magnetic field component is surrounded by the electric field components

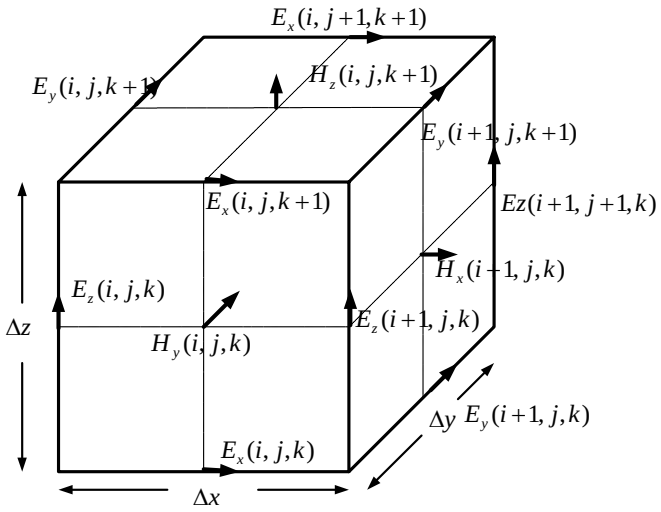

Figure 2.1.2 The field components in the Yee cell.

2.2 Numerical Stability

In the FDTD method, we need to decide the grid size first. The grid size will affect the numerical dispersion. When the grid size is fixed, the time step size Δt can also be decided based on the stability criterion.

The grid size will depend on the highest operation frequency f_u of the modeled structure. The grid size is usually set to be smaller than $\lambda_u/10$ to avoid serious numerical dispersion.

After the grid size is fixed, the time step size Δt can also be calculated. When the wave propagates in one time step, the propagation distance should not be over the grid size. To avoid numerical stability problem, the time step size should meet the FDTD Courant-Friedrich-Levy (CFL) criterion.

$$\Delta t \le \frac{1}{c\sqrt{\frac{1}{(\Delta x)^2}+\frac{1}{(\Delta y)^2}+\frac{1}{(\Delta z)^2}}} \tag{2.2.1}$$

2.3 Material Set

In this research, the material setting for FDTD simulation includes:

A. Metal Structure: The ground plane or the microstrip is metal structure. We usually assume the metal is perfect electric conductor (PEC). The thickness of metal is set to be very small and the tangential electric field is zero for metal structure.

B. Dielectric structure: The dielectric constant ε_r is set in FDTD for different dielectric materials.

C. Interface between air and dielectric structure: We use average value of dielectric

constant between two different materials. For example, we usually set the dielectric constant for air is ε_0 and dielectric constant for dielectric material is ε_r. The dielectric constant of the interface is $\frac{\varepsilon_0 + \varepsilon_r}{2}$.

2.4 Source Condition

For FDTD simulation, the sine wave is usually used with operation frequency f_0. The expression for sine wave is

$$f(t) = E_0 \sin(2\pi f_0 n\Delta t) \tag{2.4.1}$$

In our simulation, the Gaussian source is commonly used. We can set the source that is centered at time step n_0 and has a $1/e$ characteristic decay of n_{decay} time steps, the Gaussian source can be expressed as

$$f(t) = E_0 e^{-[(n-n_0)/n_{decay}]} \tag{2.4.2}$$

In the FDTD simulation, we set the source for electric field directly. For example, if we set the source at i_s for E_z component, it can be written as

$$E_z|_{i_s}^n = f(t) = E_0 \sin(2\pi f_0 n\Delta t) \tag{2.4.3}$$

2.5 Absorbing Boundary Condition

In the FDTD method, the absorbing boundary condition (ABC) is used to simulate open region problem. As shown in Fig 2.5.1, the electric field components at the boundaries should meet a particular condition to avoid reflection wave from the boundary.

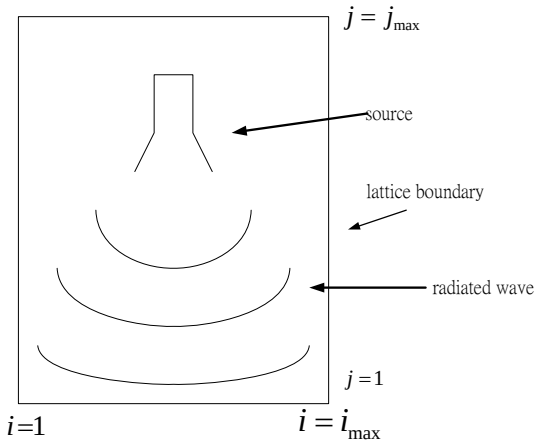

Figure 2.5.1 Absorbing boundary condition for FDTD method.

The commonly used absorbing boundary conditions are Mur's absorbing boundary

condition [34] and perfectly matched layer (PML) [24]. They are discussed briefly.

2.5.1 Mur's ABC

There are two types Mur's ABCs including Mur's first order ABC and Mur's second order ABC. We consider the electric field component E_z in a 2-D space at $x = i\Delta x$ and $y = j\Delta y$. For Mur's first order ABC, E_z can be expressed as

$$E_{i,j}^{n+1} = E_{i-1,j}^{n} + \frac{c\Delta t - \Delta x}{c\Delta t + \Delta x}\left(E_{i-1,j}^{n+1} - E_{i,j}^{n}\right) \tag{2.5.1}$$

If we assume $\Delta x = \Delta y$, the Mur's second order ABC in 2-D domain can be expressed as

$$\begin{aligned} E_{i,j}^{n+1} = & -E_{i-1,j}^{n} + \frac{c\Delta t - \Delta x}{c\Delta t + \Delta x}\left(E_{i-1,j}^{n+1} - E_{i,j}^{n}\right) + \frac{2\Delta x}{c\Delta t + \Delta x}\left(E_{i-1,j}^{n} + E_{i,j}^{n}\right) \\ & + \frac{(c\Delta t)^2}{2(\Delta x)(c\Delta t + \Delta x)}(E_{i,j+1}^{n} - 2E_{i,j}^{n} + E_{i,j-1}^{n} + E_{i-1,j+1}^{n} - 2E_{i-1,j}^{n} + E_{i-1,j-1}^{n}) \end{aligned} \tag{2.5.2}$$

In the Mur's first order ABC, the field component E_z at $x = i\Delta x$ is calculated from E_z at $x = i\Delta x$ at earlier time step and the field component E_z at $x = (i-1)\Delta x$ at the current time step. The Mur's ABC is simple and easy to implement.

2.5.2 Perfectly Matched Layer (PML)

The Berenger proposed the PML absorbing boundary condition in 1994 [24]. By using the electric and magnetic conductivities, the reflection wave can be minimized inside the PML medium. The PML medium can absorb the propagation wave in any direction. When using the PML, we need to split the electric and magnetic field components. For TM wave, the field components E_{zx} and H_x in the PML can be expressed as

$$E_{zx}\big|_{i,j}^{n+1} = \left(\frac{1 - \frac{\sigma_x \Delta t}{2\varepsilon}}{1 + \frac{\sigma_x \Delta t}{2\varepsilon}}\right) E_{zx}\big|_{i,j}^{n} + \left(\frac{\frac{\Delta t}{\varepsilon}}{1 + \frac{\sigma_x \Delta t}{2\varepsilon}}\right)\left(\frac{H_y\big|_{i+1/2,j}^{n+1/2} - H_y\big|_{i-1/2,j}^{n+1/2}}{\Delta x}\right) \tag{2.5.3}$$

$$H_x\big|_{i,j}^{n+1/2} = \left(\frac{1 - \frac{\sigma_y^* \Delta t}{2\mu}}{1 + \frac{\sigma_y^* \Delta t}{2\mu}}\right) H_x\big|_{i,j}^{n-1/2} + \left(\frac{\frac{\Delta t}{\mu}}{1 + \frac{\sigma_y^* \Delta t}{2\mu}}\right)\left(-\frac{E_z\big|_{i,j+1/2}^{n} - E_z\big|_{i,j-1/2}^{n}}{\Delta y}\right) \tag{2.5.4}$$

The σ_x and σ_x^* are electric conductivity and magnetic conductivity, respectively. They are function of PML layers. Fig. 2.5.2 shows the electric conductivity and magnetic

conductivity in the PML medium.

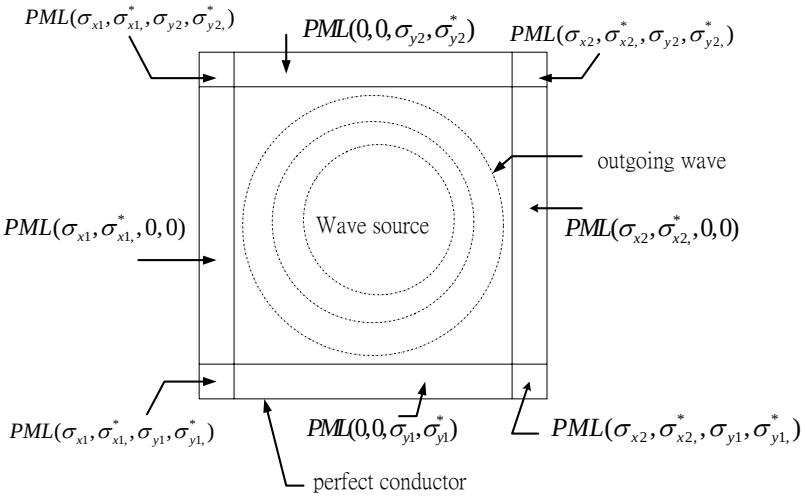

Figure 2.5.2 PML absorbing boundary condition

The PML impedance can be matched to the free space impedance with the condition

$$\frac{\sigma}{\varepsilon}=\frac{\sigma^*}{\mu} \tag{2.5.5}$$

The PML conductivity profile is usually scaled to reduce the reflection error.

$$\sigma_{s\max}=\sigma_{opt}\approx\frac{(m+1)}{150\pi\Delta s}$$

$$\sigma_s(s)=\frac{\sigma_{s\max}|s-s_0|^m}{d^m} \qquad s = x, y, z \tag{2.5.6}$$

where d is the thickness of PML absorber, Δs is the cell size, and s_0 represents the interface. Typically, we choose m = 4 for optimum PML performance [25]

2.6 Near Field to Far Field Transformation

It is not practical to directly simulate the electric and magnetic fields in the far field within the FDTD grid. This will require a large computational domain to include the far field. The field components in the far field can be calculated by near field to far field transformation [35]. First, we calculate the equivalent electric current and equivalent magnetic current in the near field in the region enclosed the computational domain. From the near field equivalent electric current and equivalent magnetic current, we can obtain the field components in the far field. We can calculate the antenna radiation pattern by using this method.

As shown in Fig 2.6.1, we use the virtual surface S_{ab} to enclose the B region. First we can calculate the tangential fields E_s and H_s. After obtaining the E_s and H_s, we can calculate the equivalent surface electric current J_s and equivalent surface magnetic current M_s at the surface of S_{ab}

$$J_s(r) = \hat{n} \times H^s(r) \tag{2.6.1}$$

$$M_s(r) = -\hat{n} \times E^s(r) \tag{2.6.2}$$

where $\hat{n}$ is normal to the surface of S_{ab}

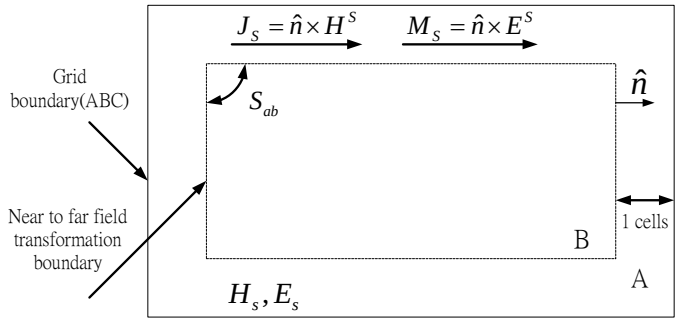

Figure 2.6.1 Near field to far field transformation

In the near field to far field transformation, the near field in the closed volume is calculated first. Then, the field components in the far field can be calculated by Kirchhoff surface integral representation (KSIR) as

$$\psi(\vec{r},t) = \frac{1}{4\pi} \oint_{s'} \hat{n} \left[\frac{\nabla' \psi(\vec{r}',t')}{R} - \frac{\vec{R}}{R^3} \psi(\vec{r}',t') - \frac{\vec{R}}{cR^2} \frac{\partial \psi(\vec{r}',t')}{dt'} \right] da' \tag{2.6.3}$$

where

$\vec{r}$ is any point in the far field

$\vec{r}'$ is the point at the surface of the FDTD computational domain

$\vec{R} = \vec{r} - \vec{r}'$

$R = |\vec{R}|$

$\hat{n}$ is normal to the computational surface

c is light velocity

a' is closed surface for FDTD method

The KSIR can calculate the field components in the far field outside the computational domain. Therefore, we can calculate the field components in the far field as follow

A. The near field components of arbitrary scatter can be calculated by FDTD method easily.

B. The far field components in any direction can be calculated from the KSIR method.

We can use the Gaussian excitation source to obtain the wideband field components

in the far field. The frequency domain field components can be obtained by using Discrete Fourier Transformation (DFT) method.

2.7 Lumped Elements

FDTD method can also be used to simulate linear and non-linear lumped elements [36, 37]. We assume the lumped elements are place in the z-direction, and the FDTD method for lumped elements is described as follow

2.7.1 FDTD Method for Lumped Elements

We consider the Maxwell's equation with current source

$$\nabla \times \vec{H} = \vec{J}_c + \frac{\partial \vec{D}}{\partial t} \tag{2.7.1}$$

where $\vec{J}_c = \sigma \vec{E}$ and $\vec{D} = \varepsilon \vec{E}$, we can discretized the (2.7.1) by central difference method

$$E_z\big|_{i,j,k}^{n+1} = \left(\frac{1-\frac{\sigma_{i,j,k}\Delta t}{2\varepsilon_{i,j,k}}}{1+\frac{\sigma_{i,j,k}\Delta t}{2\varepsilon_{i,j,k}}}\right) E_z\big|_{i,j,k}^{n} + \left(\frac{\frac{\Delta t}{\varepsilon_{i,j,k}}}{1+\frac{\sigma_{i,j,k}\Delta t}{2\varepsilon_{i,j,k}}}\right)\left(\frac{H_y\big|_{i+1/2,j,k}^{n+1/2} - H_y\big|_{i-1/2,j,k}^{n+1/2}}{\Delta x} \quad \frac{H_x\big|_{i,j-1/2,k}^{n+1/2} - H_x\big|_{i,j+1/2,k}^{n+1/2}}{\Delta y}\right) \tag{2.7.2}$$

It should be noticed that the magnetic field is at (n+1/2) time step, which is located between the $E_z\big|_{i,j,k}^{n}$ and $E_z\big|_{i,j,k}^{n+1}$. The J_c is also at the time step (n+1/2)*th* time step and can be calculated by

$$J_c\big|_{i,j,k}^{n+1/2} = \sigma_{i,j,k} E_z\big|_{i,j,k}^{n+1/2} = \frac{\sigma_{i,j,k}}{2}\left(E_z\big|_{i,j,k}^{n} + E_z\big|_{i,j,k}^{n+1}\right) \tag{2.7.3}$$

We assume all the lumped elements are in free space ($\varepsilon = \varepsilon_0$, $\sigma = 0$, and $J_c = 0$). The $\nabla \times H$ for FDTD can be rewritten as

$$\nabla \times H_{i,j,k}^{n+1/2} = \frac{H_y\big|_{i+1/2,j,k}^{n+1/2} - H_y\big|_{i-1/2,j,k}^{n+1/2}}{\Delta x} + \frac{H_x\big|_{i,j-1/2,k}^{n+1/2} - H_x\big|_{i,j+1/2,k}^{n+1/2}}{\Delta y} \tag{2.7.4}$$

Therefore, (2.7.2) can become

$$E_z\big|_{i,j,k}^{n+1} = E_z\big|_{i,j,k}^{n} + \frac{\Delta t}{\varepsilon_0} \nabla \times H_{i,j,k}^{n+1/2} \tag{2.7.5}$$

In the FDTD method, we will introduce the current density J_L for lumped elements

$$\nabla \times \vec{H} = \vec{J}_C + \frac{\partial \vec{D}}{\partial t} + \vec{J}_L \tag{2.7.6}$$

Assuming the element located at $E_z\big|_{i,j,k}$ in the z direction. The relation between the

current density J_L and lumped element current I_L is

$$J_L = \frac{I_L}{\Delta x \Delta y} \tag{2.7.7}$$

$$V = E_z|_{i,j,k}\ \Delta z \tag{2.7.8}$$

From (2.7.5), the FDTD algorithm for lumped element can be written as

$$E_z|_{i,j,k}^{n+1} = E_z|_{i,j,k}^{n} + \frac{\Delta t}{\varepsilon_0}\nabla \times H_{i,j,k}^{n+1/2} - \frac{\Delta t}{\varepsilon_0 \Delta x \Delta y} I_L^{n+1/2} \tag{2.7.9}$$

2.7.2 Resistor

We assume to place a resistor at $E_z|_{i,j,k}$ in the z direction. The relation for voltage and current is

$$I_z|_{i,j,k}^{n+1/2} = \frac{\Delta z}{2R}\left(E_z|_{i,j,k}^{n+1} + E_z|_{i,j,k}^{n}\right) \qquad J_L = \frac{I_z|_{i,j,k}^{n+1/2}}{\Delta x \Delta y} \tag{2.7.10}$$

Substituting the (2.7.10) into (2.7.9), we can obtain the FDTD algorithm for resistor.

$$E_z|_{i,j,k}^{n+1} = \left(\frac{1 - \frac{\Delta t \Delta z}{2R\varepsilon_0 \Delta x \Delta y}}{1 + \frac{\Delta t \Delta z}{2R\varepsilon_0 \Delta x \Delta y}}\right) E_z|_{i,j,k}^{n} + \left(\frac{\frac{\Delta t}{\varepsilon_0}}{1 + \frac{\Delta t \Delta z}{2R\varepsilon_0 \Delta x \Delta y}}\right) \nabla \times H_{i,j,k}^{n+1/2} \tag{2.7.11}$$

2.7.3 Resistive Voltage Source

The FDTD can also simulate the resistive voltage source. We assume the element is placed in z direction and the relation between the voltage and current is

$$I_z|_{i,j,k}^{n+1/2} = \frac{\Delta z}{2R_S}\left(E_z|_{i,j,k}^{n+1} + E_z|_{i,j,k}^{n}\right) + \frac{V_S^{n+1/2}}{R_S} \qquad J_L = \frac{I_z|_{i,j,k}^{n+1/2}}{\Delta x \Delta y} \tag{2.7.12}$$

where $V_S^{n+1/2}$ is excitation source and R_S is matching impedance

The FDTD algorithm for resistive voltage source is

$$E_z|_{i,j,k}^{n+1} = \left(\frac{1 - \frac{\Delta t \Delta z}{2R\varepsilon_0 \Delta x \Delta y}}{1 + \frac{\Delta t \Delta z}{2R\varepsilon_0 \Delta x \Delta y}}\right) E_z|_{i,j,k}^{n} + \left(\frac{\frac{\Delta t}{\varepsilon_0}}{1 + \frac{\Delta t \Delta z}{2R\varepsilon_0 \Delta x \Delta y}}\right) \nabla \times H_{i,j,k}^{n+1/2} + \left(\frac{\frac{\Delta t}{R_S \varepsilon_0 \Delta x \Delta y}}{1 + \frac{\Delta t \Delta z}{2R_S\varepsilon_0 \Delta x \Delta y}}\right) V_S^{n+1/2} \tag{2.7.13}$$

2.8 FDTD Method for Computer Calculation

We have explained the basic algorithm for FDTD method. In the FDTD method, we

calculate the electric and magnetic fields in each time step. Before running the FDTD for each time step, we need to set the FDTD parameters like grid size, time step size, source condition. The flow of FDTD method for computation is explained below

2.8.1 Pre-Processing

A. Define the FDTD grid size

B. Define the time step size to meet the stability condition

C. Calculate the FDTD parameters for different materials

2.8.2 Time Stepping

A. Assign the excitation

B. Calculate the electric field components

C. Employ the absorbing boundary condition to absorb the outgoing wave.

D. Calculate the magnetic field components

2.8.3 Post-Processing

A. Recording the electric and magnetic fields at each time step.

B. Calculate the electric and magnetic fields in far field.

Chapter 3

Study of SAR Reduction with Metamaterials

In this work, the EM interaction between the antenna and the human head is reduced with metamaterials. Preliminary study of SAR reduction with metamaterials is performed by FDTD method with lossy Drude model. It is found that the specific absorption rate (SAR) in the head can be reduced by placing the metamaterials between the antenna and the head. The antenna performances and radiation pattern with metamaterials are analyzed. A comparative study with other SAR reduction techniques is also provided. The metamaterials can be obtained by arranging split ring resonators (SRRs) periodically. In this research, we design the SRRs operated at 900 MHz and 1800 MHz bands. The design procedure will be described. Numerical results of the SAR values in a muscle cube with the presence of SRRs are shown to validate the effect of SAR reduction. These results can provide helpful information in designing the mobile communication equipments for safety compliance.

3.1 Preliminary Studies of SAR Reduction by FDTD Method with Lossy Drude Model

3.1.1 FDTD Method with Lossy Drude Model

Preliminary studies of SAR reduction with metamaterials were performed by FDTD with lossy Drude model. The SAR reduction effectiveness and antenna performance with different positions, sizes, and negative medium parameters of metamaterials will be analyzed. The head model used in this study was obtained from Magnetic resonance imaging (MRI) based head model through The Whole Brain Atlas website. In the MRI human head model, different colors of the human head represent different tissues, as shown in Fig. 3.1.1. In this study, six types of tissues, i.e., bone, brain, muscle, eyeball, fat, and skin, were involved in this model.

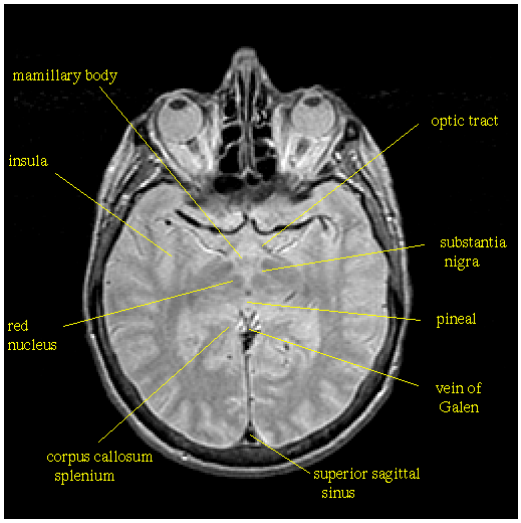

Figure 3.1.1 MRI human head model

The MRI human head model is discretized for FDTD simulation. Fig. 3.1.2 shows a horizontal cross section through the eyes of this head model. The electrical properties of tissues were taken from [3, 4], as shown in Table 3.1.

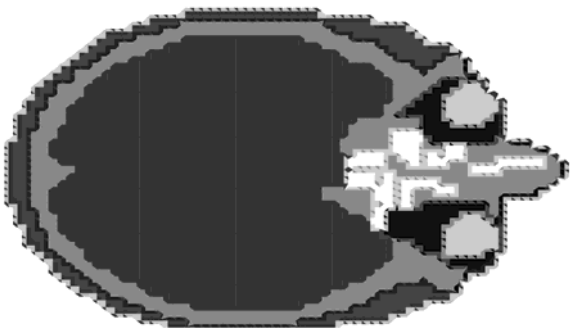

Figure 3.1.2 Human head model for FDTD computation.

Table 3.1 electric properties for human head model

		900MHz		1.8GHz	
Tissue	ρ	ε_r	σ	ε_r	σ
Bone	1810	17.4	0.19	15.5	0.39
Brain	1040	44.1	0.89	42.2	1.18
Muscle	1040	51.8	1.11	49.4	1.53
Eyeball	1010	74.3	1.97	73.7	2.33
Fat	920	10.0	0.17	9.55	0.22
Skin	1010	39.5	0.69	38.9	0.95

The formulation of SAR is defined as $SAR = \sigma|E|^2 / 2\rho$, where E, σ, and ρ are the electric field, conductivity, and mass density in the head, respectively.

Simulations of metamaterials are performed by FDTD method with lossy Drude model [13]. The method is a useful method to understand the wave propagation characteristics of metamaterials. In this method, let μ and ε be modeled by the following expressions

$$\varepsilon = \varepsilon_0\left(1-\frac{\omega_{pe}^2}{\omega(\omega+i\Gamma_e)}\right) \tag{3.1.1}$$

$$\mu = \mu_0\left(1-\frac{\omega_{pm}^2}{\omega(\omega+i\Gamma_m)}\right), \tag{3.1.2}$$

where ω_p and Γ denote the corresponding plasma and damping frequencies, respectively.

We can provide a slight variation of (3.1.1) as

$$\varepsilon = \varepsilon_0\left(1-\frac{\omega_{pe}^2}{(\omega+i\Gamma_{e1})(\omega+i\Gamma_{e1})}\right) \tag{3.1.3}$$

This model is actually Lorentz medium model, e.g.,

$$\varepsilon_L = \varepsilon_0\left(1-\frac{\omega_{pe}^2}{\omega^2+i\Gamma_e\omega-\omega_{0e}^2}\right), \tag{3.1.4}$$

where $\Gamma_e = \Gamma_{e1}+\Gamma_{e2}$ and $\omega_{0e}^2 = \Gamma_{e1}\Gamma_{e2}$.

With this method, we can treat the metamaterials as homogenous materials with frequency-dispersive material parameters.

3.1.2 SAR Calculation Verification

The developed FDTD method for SAR calculation is studied and verified. Fig. 3.1.3 shows the muscle cube and antenna models in this study. The antenna was arranged parallel to the cube axis. The muscle cube was formed by muscle tissue with $\varepsilon_r = 51.8$, $\sigma = 1.11$, and $\rho = 1040$ at 900 MHz.

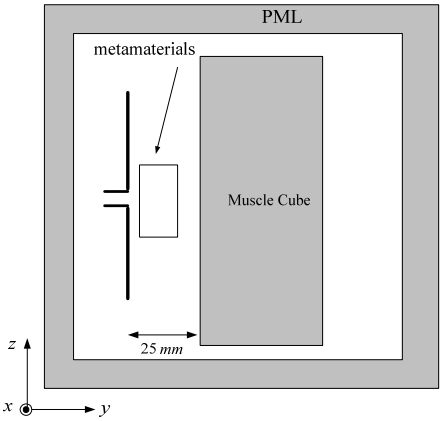

Fig. 3.1.3 Test Structure used in SAR calculation.

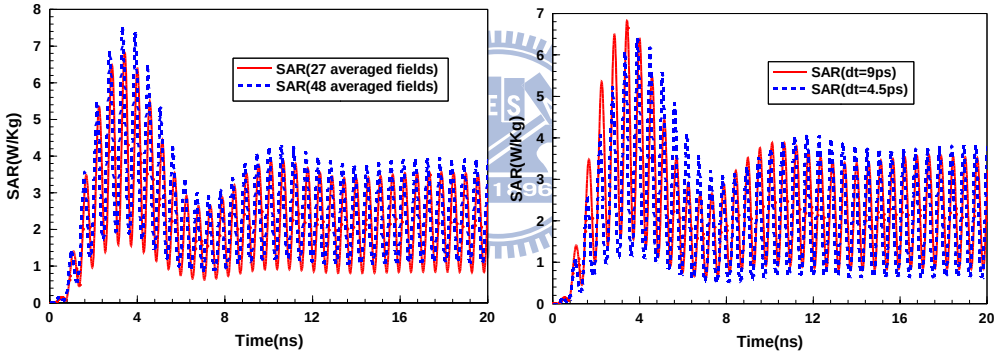

(a) different sampled fields (b) different grid size and time step

Fig. 3.1.4 SAR calculation in the muscle cubic for numerical tests.

The SAR value was calculated for an antenna output power equal to 1 W. In this FDTD simulation, the Δx =5mm, Δy=5mm, Δz=5mm, and Δt=9.0 *ps* were used. The calculated steady-state SAR_{1g} value is shown in Fig. 3.1.4. First, the peak SAR value was calculated from 27 averaged electric fields. It is found that the calculated peak SAR_{1g} without metamaterials was 3.70 W/kg. Then, 48 electric fields were averaged to obtain the SAR values. The calculated peak SAR_{1g} was 3.87 W/kg. Similar results can be obtained for SAR calculation with different sampled electric fields.

Since the grid size will affect the accuracy of the FDTD simulation, the calculated SAR values for different grid size and time step were studied. The smaller grid size with Δx =2.5mm, Δy=2.5mm, Δz=2.5mm, and Δt=4.5 *ps* were also studied. The calculated peak SAR_{1g} with smaller grid size was 3.82 W/kg, which is similar to

previous results.

Then, the metamaterials were placed between the antenna and human head. The distance between the antenna feeding point and edge of metamaterials was 5 mm. The size of metamaterials in *xz* plane was 50 mm × 50 mm and thickness was 10 mm. The metamaterials with μ = 1 and $\varepsilon = -3$ at 900 MHz are employed. As shown in Fig. 3.1.5, it is found that the calculated SAR value is reduced to be 3.25W/kg.

To investigate the EM wave interaction between the muscle cube and antenna, Fig. 3.1.6 shows the SAR distribution in the yz section of the muscle cube. It is found that the peak SAR occurs near the antenna. The SAR distribution of the muscle cube with metamaterials is also studied. A significant SAR reduction in the muscle cube can be observed with the metamaterials placement.

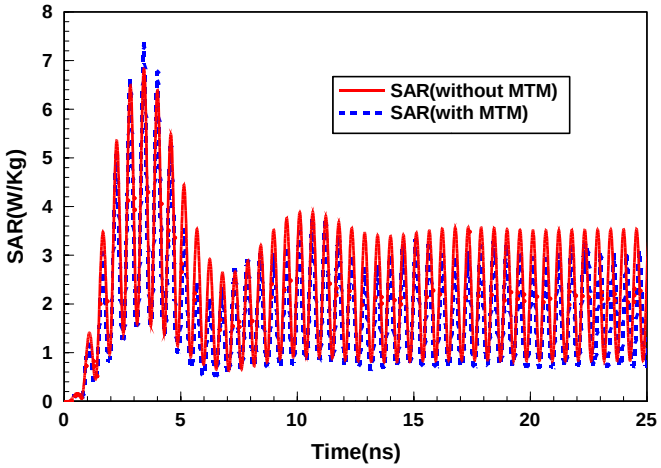

Fig. 3.1.5 SAR calculation in the muscle cubic

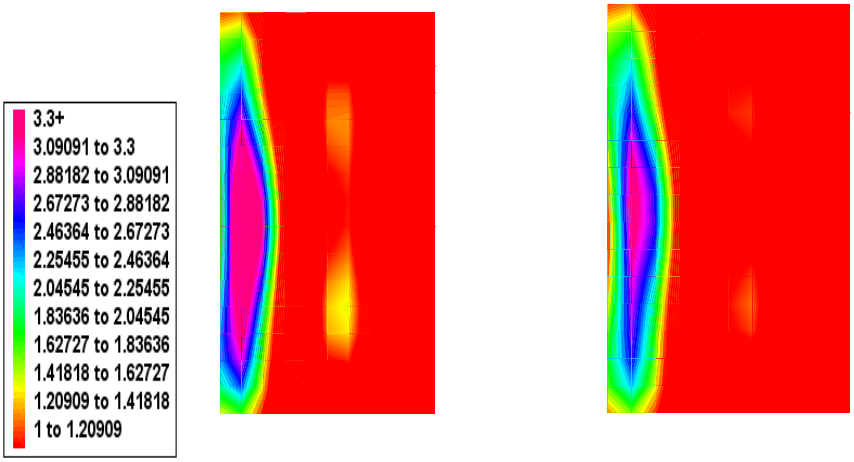

(a) (b)

Fig. 3.1.6 SAR distribution (t=15 ns) in the yz section of the muscle cubic (a) SAR distribution without metamaterials (b) SAR distribution with metamaterials.

To validate the effect of SAR reduction with metamaterials, the commercial tool Ansoft HFSS [47] is utilized for simulation. The radiated power from antenna with μ = 1 and $\varepsilon = -3$ medium is also fixed at 1 W. The SAR distribution in the yz cross section of the muscle cubic is studied, as shown in Fig. 3.1.7. It is found that the calculated SAR value is reduced from 3.45 W/kg to 3.10 W/kg. Peak SAR value occurs close to antenna can also be observed for both HFSS and FDTD results. The SAR reduction with metamaterials can also be observed with Ansoft HFSS simulator to validate our study.

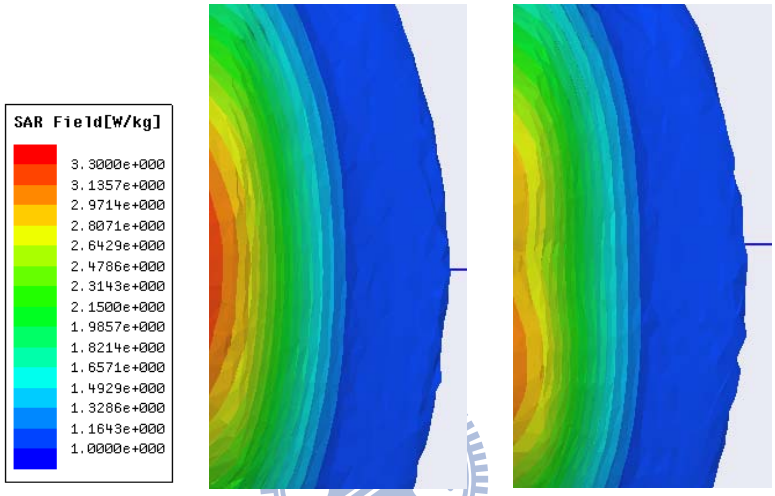

Fig. 3.1.7 SAR distribution with HFSS solver (a) SAR distribution without metamaterials (b) SAR distribution without metamaterials.

3.1.3 SAR Calculation in the Head with Metamaterials

Fig. 3.1.8 shows the human head and antenna models in this study. Numerical simulation of SAR value was performed by FDTD method. The parameters for FDTD computation were as follows. The simulated domain were $128 \times 128 \times 128$ cells. The cell sizes were set as $\Delta x = \Delta y = \Delta z = 3.0$ mm. The computational domain was terminated with 8 cells PML. A dipole antenna was modeled by thin-wire approximation. The antenna was arranged parallel to the head axis. The distance between the antenna and head surface was 3.0 cm. The SAR value was calculated for an antenna output power equal to 600 mW. The calculated steady-state SAR_{1g} value is shown in Fig. 3.1.9. It is found that the calculated peak SAR_{1g} without metamaterials was 2.43 W/kg. The SAR simulation is compared with the results in [3, 4] for validation, as shown in Table 3.2. Although different head and antenna models were used, the simulated SAR_{1g} is similar to their results.

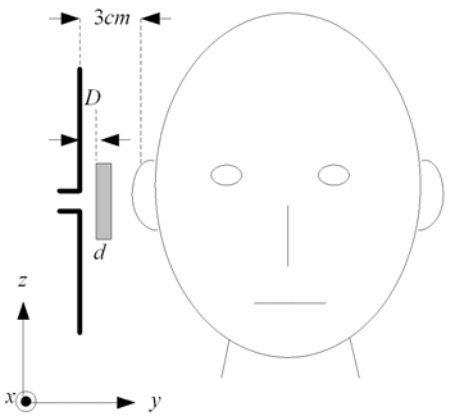

Figure 3.1.8 The head and antenna models for SAR calculation.

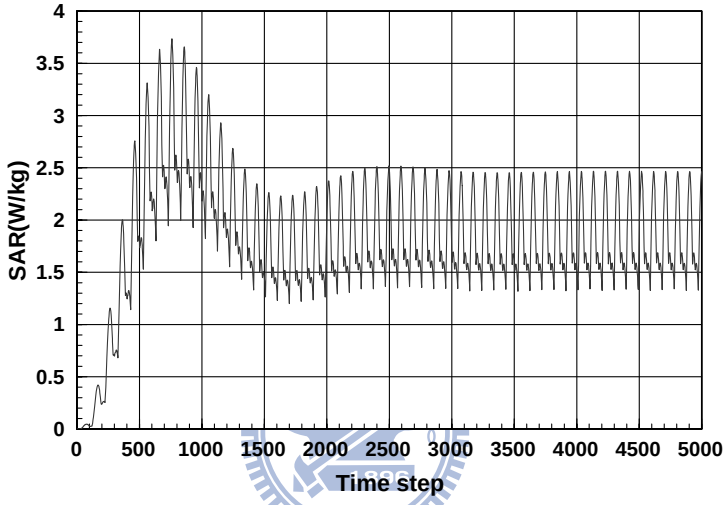

Figure 3.1.9 Calculated SAR_{1g} from FDTD simulation

Table 3.2 Comparisons of peak SAR

Frequency	Tissue	[3]	[4]	This work
900MHz	Whole head	2.17	2.28	2.43

The metamaterials were placed between the antenna and human head. The distance *D* between the antenna feeding point and edge of metamaterials was 3 mm. The size of metamaterials in *xz* plane was 45 mm × 45 mm and thickness *d* was 6 mm. The SAR value and antenna performance with metamaterials were analyzed. To evaluate the power radiated from the antenna, the source impedance (Z_S) was assumed equal to the complex conjugate of the free space radiation impedance (Z_S= 102.14 - *j*83.78 Ω). The source voltage (V_S) was chosen to obtain a radiated power in free space equal to 600 mW ($V_S = \sqrt{0.6 \cdot 8 \cdot R_{R0}}$). When analyzing the influence of the metamaterials and

the human head on the antenna performance, the source impedance and source voltage were fixed at the Z_S and V_S values. The power radiated from the antenna was evaluated by computing the radiation impedance in this situation (Z_R=R_R+jX_R) and used the following equation [38]

$$P_R = \frac{1}{2} V_S^2 \frac{R_R}{|Z_R + Z_S|^2} \tag{3.1.5}$$

The total power absorbed in the head was calculated by

$$P_{abs} = \frac{1}{2} \int_V \sigma |E|^2 dv \tag{3.1.6}$$

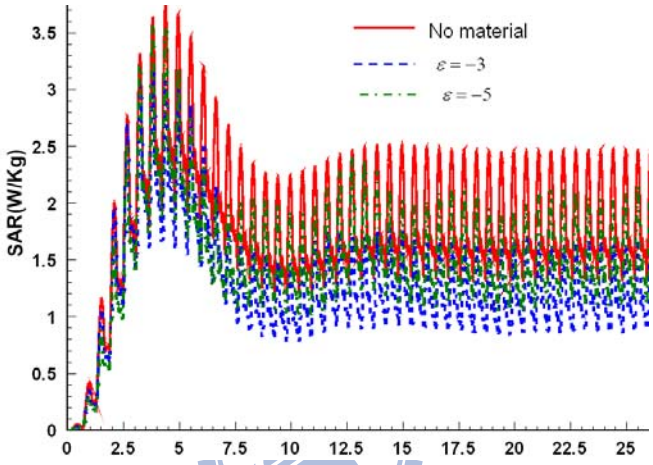

Figure 3.1.10 Calculated SAR_{1g} from FDTD simulation with metamaterials

Different negative medium parameters for SAR reduction effectiveness were analyzed. We placed negative permittivity mediums between the antenna and the human head. First, the plasma frequencies of the mediums were set to be ω_{pe} = 11.309×10^9 *rad/s*, ω_{pm} = 0 which give mediums with μ = 1 and ε = –3 at 900 MHz. The mediums with larger negative permittivity μ = 1 and ε = –5 were also studied. We set Γ_e =1.0×10^8 *rad/s*, suggesting the mediums have losses. Numerical results of SAR value and antenna performance are given in Figure 3.1.10 and Table 3.3.

Table 3.3 Effects of metamaterials on antenna performances and SAR reduction at 900 MHz

	Z_R (Ω)	P_R (mW)	Pabs (mW)	SAR_{1g} (W/kg)
No material	74.59 + j92.75	600	317.98	2.43
μ = 1, ε = -3	57.42 + j99.83	547.3	224.3	1.73
μ = 1, ε = -5	61.63 - j94.43	560.9	271.7	2.07

From the simulation results, it is found that the peak SAR_{1g} becomes 1.73 W/kg with μ = 1 and $\varepsilon = -3$ mediums. Compared to the condition without metamaterials, the radiated power is reduced for 8.78% while the SAR is reduced for 28.8 %. With the use of μ = 1 and $\varepsilon = -5$ mediums, the SAR reduction effectiveness is decreased. However, the radiated power from the antenna is less affected.

To investigate the EM wave interaction between the human head and antenna, Fig. 3.1.11 shows the SAR value in the horizontal cross section through the eyes of this head model. It is found that the peak SAR occurs near the ear close to the antenna. The SAR values with μ = 1 and $\varepsilon = -3$ is also demonstrated for comparison. A significantly SAR reduction in the human head can also be observed.

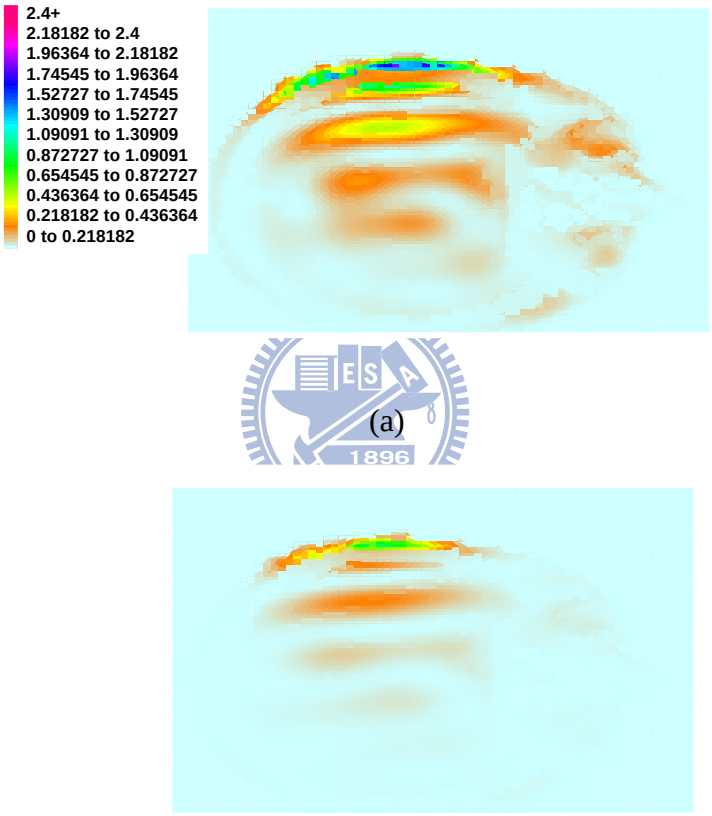

(a)

(b)

Figure 3.1.11 SAR values in the horizontal cross section of this head (a) without metamaterials (b) with metamaterials

Comparisons of the SAR reduction effectiveness with different positions and sizes of metamaterials were analyzed. Simulation results are shown in Table 3.4. In case A, the distance *D* between the antenna and metamaterials was changed from 3 mm to 6 mm. In case B, the metamaterials thickness *d* was reduced from 6 mm to 3 mm. It is found that both the peak SAR_{1g} and power absorbed by the head increase with the

increase of distance *D* or the decrease of thickness *d*. In case C, the size of metamaterials was increased from 45 mm × 45 mm to 48 mm × 48 mm. It can be noted that the peak SAR_{1g} is reduced significantly while the degradation on the radiated power due to metamaterials is insignificant.

Table 3.4 Effects of sizes and positions of metamaterials on antenna performances and SAR values

	$Z_R(\Omega)$	P_R (mW)	*P*abs (mW)	SAR_{1g} (W/kg)
No material	74.59 + j92.75	600	317.98	2.43
$\mu = 1, \varepsilon = -3$	57.42 + j99.83	547.3	224.3	1.73
Case A	65.48 + j93.34	569.4	282.7	2.15
Case B	73.41 + j95.10	581.5	289.7	2.26
Case C	83.93 + j106.63	585.4	235.9	1.78

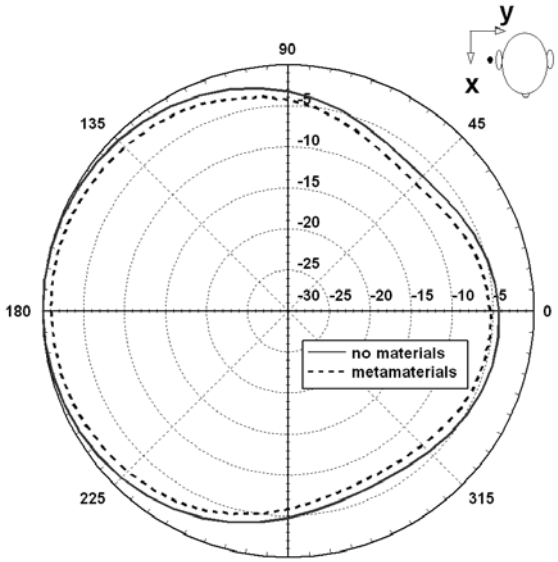

Figure 3.1.12 Calculated ϕ plane radiation pattern at 900 MHz.

To further investigate whether the metamaterials less affected the antenna performance or not, radiation pattern of the dipole antenna with μ = 1 and $\varepsilon = -3$ metamaterials were analyzed. The radiation patterns were obtained by the near- and far-field transformation of the Kirchhoff surface integral representation (KSIR) [35]. All the radiation patterns were normalized to the maximum gain obtained without materials. Fig. 3.1.12 shows the radiation patterns in ϕ plane for $\theta = 90^0$. In [5], the radiation pattern close to the head is reduced about 6 dB and our simulation result is similar to their result. With the use of metamaterials, it can be seen that the maximum degradation of the far field does not exceed 1.21 dB.

The use of metamaterials was also compared with other SAR reduction techniques. The PEC reflector and ferrite material were commonly used in SAR reduction. The PEC reflector and ferrite sheet were analyzed with the same size and position as metamaterials. The relative permittivity and permeability of ferrite sheet were $\varepsilon = 7.0\text{-}j0.58$ and $\mu = 2.83\text{-}j3.25$, respectively. Numerical results are shown in Table 3.5. A PEC placed between human head and antenna is studied. It can be found that the peak SAR_{1g} is increased with the use of PEC reflector. This is because the EM wave can be induced in the neighbor of a PEC reflector due to scattering. When the size of PEC sheet is small compared to human head, the head will absorb more EM energy. Similar results of peak SAR increase with PEC placement was also reported in [5]. The use of ferrite sheet can reduce the peak SAR_{1g} effectively. However, the degradation on radiated power from antenna is also significant. In addition, compare to the use of ferrite sheet, the metamaterials can be designed at the desired operation frequency. The metamaterials are designed on circuit board so it may be easily integrated to the cellular phone. The design procedure will be shown in section 3.2.

Table 3.5 Comparisons of SAR reduction techniques with different materials

	$Z_R(\Omega)$	P_R(mW)	SAR_{1g}(W/kg)
$\mu = 1, \varepsilon = -3$	57.42 + j99.83	547.3	1.73
PEC reflector	71.53 + j33.03	535.61	5.37
Ferrite sheet	180.34 + j161.76	514.7	0.52

To study the effect of SAR reduction with the use of metamaterials, the radiated power from the dipole antenna with $\mu = 1$ and $\varepsilon = -3$ mediums was fixed at 600 mW. Numerical results are shown in Table 3.6. It is found that the use of metamaterials can reduce the peak SAR_{1g} for 22.2%.

Table 3.6 Effect of metamaterials on SAR reduction
(P_R = 0.6 W for 900 MHZ)

	900 MHz	
	No material	$\mu = 1, \varepsilon = -3$
SAR_{1g}	2.43	1.89

3.2 SRRs Design Methodology and SAR Reduction

3.2.1 SRR Structure

From the FDTD analysis, we found that metamaterials can be used to reduce the peak SAR_{1g} in the head. In this section, the metamaterials operated at 900 MHz and 1800 MHz bands of the cellular phone were designed. The metamaterials can be obtained by arranging split ring resonators (SRRs) periodically. The SRRs considered here consisted of two square rings, each with gaps appearing on the opposite sides. The configuration has a geometry that is similar to the SRR structures in [39]. As shown in Fig. 3.2.1, the structure of a single SRR is defined by the following structure parameters: the square ring size *l*, the ring thickness *c*, the ring gap *d*, and the split gap *g*. The resonant frequency of SRRs can be shifted toward higher or lower frequency band by properly choosing these structure parameters.

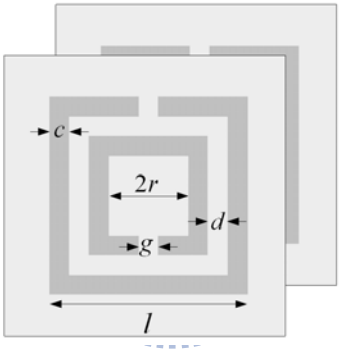

Figure 3.2.1 The structures of split ring resonators (SRRs).

3.2.2 SRR Design and Simulation

Numerical simulation can predict the transmission properties of SRRs with various structure parameters. We used FDTD method to simulate the SRRs structures. For all simulations, EM wave propagated along the *y* direction. The electric field polarization was kept along the *z* axis and magnetic field polarization was kept along *x* axis. Periodic boundary condition was used to reduce the computational domain and absorbing boundary condition was used at the propagation region. The total-field/scatter-field formulation was used to excite plane wave. The region inside of the computational domain and outside of the SRRs was assumed to be vacuum.

To verify our FDTD simulation, the structure parameters of SRRs were chosen the same as [39]. The structure parameters were $d = g = c = 0.33$ mm, and $l = 3$ mm. The thickness and dielectric constant of the circuit board were 0.45 mm and 4.4, respectively. The SRRs were placed in the *yz* plane, as shown in Fig. 3.2.2. The unit elements in the propagation *y* direction were 25 elements. Periodic boundary

conditions were applied normal to the propagation direction. Fig. 3.2.3 shows the transmission spectra of SRRs in this simulation. In [39], the measured results show that the SRRs display a stop band extending from 8.1 to 9.5GHz, which is similar to our simulation results.

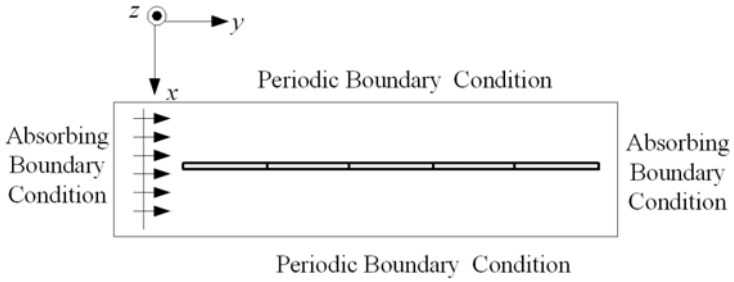

Figure 3.2.2 Top view of the FDTD setup for SRRs simulation ($H_{\parallel}$).

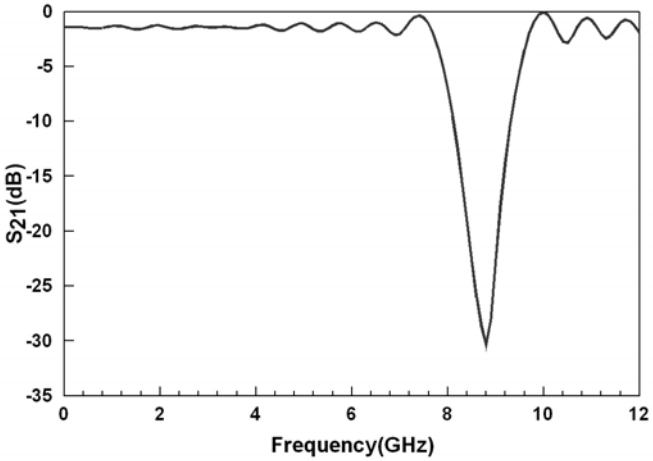

Figure 3.2.3 Modeled transmission spectra of SRRs placed in the *yz* plane.

The SRRs placed in the *xz* plane were considered, as shown in Fig. 3.2.4. The structure parameters of SRRs were the same as previous study in this section. The unit elements in the propagation *y* direction were 20 elements. Periodic boundary conditions were applied normal to the propagation direction. Fig. 3.2.5 shows simulated transmission spectra of SRRs. The stop band is shifted toward higher frequency band and extends from 18 GHz to 24 GHz. From this study, it is found that both of the two incident polarizations can produce stop band. As shown in [40], the stop band corresponds to a region where either permittivity or permeability is negative. When the magnetic field is polarized along the split ring axes $H_{\parallel}$, it will produce a magnetic field that may either oppose or enhance the incident field. A large capacitance in the region between the rings will be generated and the electric field will be strongly concentrated. There is strong field coupling between SRRs and the permeability medium will be negative at stop band. On the other hand, the behavior of the stop band can be contrasted with that occurring for the $H_{\perp}$ case. Because the

magnetic field is parallel to the plane of SRRs, we assume the magnetic effects are small, and that permeability is small, positive, and slowly varying. In the $H_{\perp}$ condition, these structures can be viewed as arranging the metallic wires periodically. The continuous wires behave like high-pass filter, which means the permittivity can be negative below the plasma frequency. For this metallic wire structures, there will be a stop band around the resonance frequency. As shown in Fig 3.2.5, a stop band occurs, but outside of the stop band region of the $H_{\parallel}$ polarization. The contrast between the two stop bands in the $H_{\parallel}$ and $H_{\perp}$ cases illustrates the difference between the magnetic and electric responses of the SRRs. Theoretical investigations in [40] have shown that the $H_{\parallel}$ band gap is due to negative permeability and the $H_{\perp}$ band gap is due to negative permittivity.

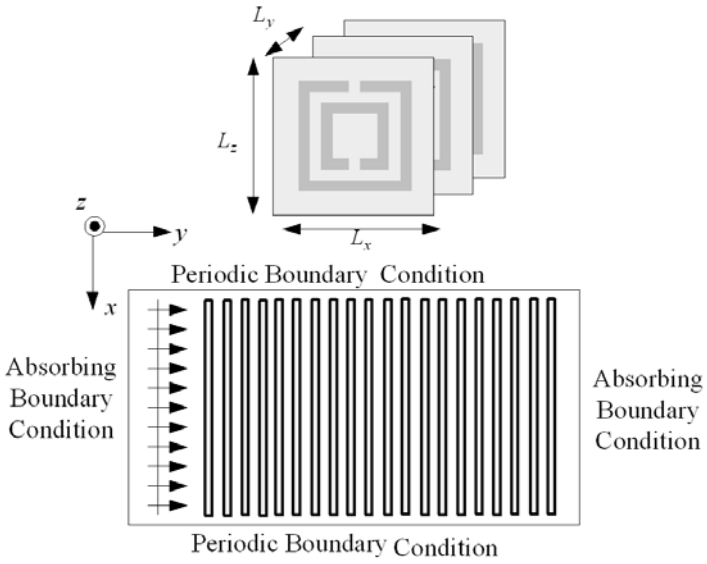

Figure 3.2.4 Top view of FDTD simulation for SRRs placed in the *xz* plane ($H_{\perp}$).

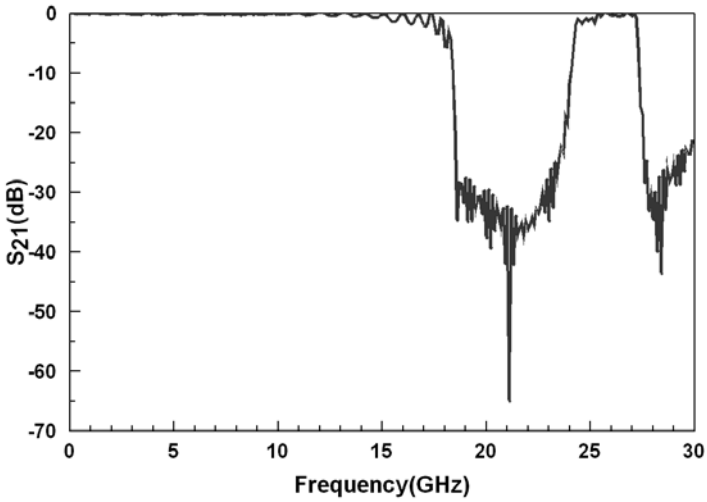

Figure 3.2.5 Modeled transmission spectra of SRRs placed in the *xz* plane.

We will investigate whether the performance of metamaterials is affected or not when placing closely to materials with large dielectric constant and conductivity. The SRRs placed closely to dielectric cube with $\varepsilon = 49.4$ and σ=1.53 was studied, as shown in Fig. 3.2.6. The simulation condition was the same as above study except the presence of dielectric cube. The receiving point of S_{21} is placed between the SRRs and dielectric cube. Fig. 3.2.7 shows the calculated transmission spectra of SRRs. Compared to the condition without dielectric cube, the magnitudes of transmission spectra are changed. However, the frequency of stop band is not affected. The SRRs can still retain their propagation properties if placed closely to large dielectric materials.

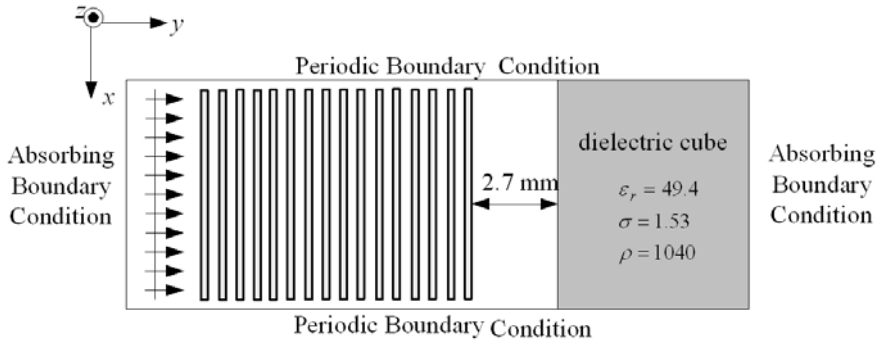

Figure 3.2.6 Top view of FDTD simulation for SRRs with dielectric cube.

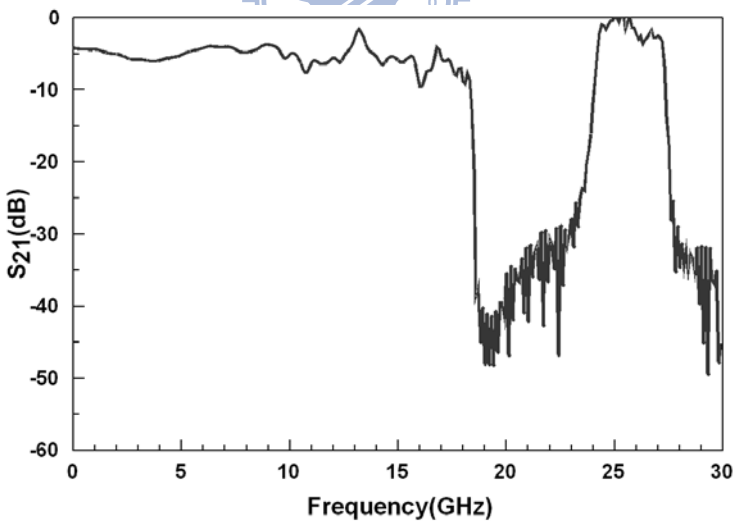

Figure 3.2.7 Modeled transmission spectra of SRRs placed in the *xz* plane with dielectric cube.

From the numerical study by FDTD method with Drude model, we find that the peak SAR value in the human head can be reduced by using negative permittivity mediums. The SRRs placed in the *xz* plane were considered. On the other hand, the size of the metamaterials in the EM propagation direction will not be too large with

this placement. To construct the SRRs for SAR reduction, we have changed the structure parameters of SRRs that the stop band can be designed at 900 MHz and 1800 MHz band, respectively. From FDTD simulation, we found that the ring size l is an important factor for operation frequency. The stop band can be shifted toward lower frequency band by increasing the ring size. To obtain a stop band at 900 MHz, the structure parameters of SRR were chosen as c = 1.8 mm, d = 0.6 mm, g = 0.6 mm, and l = 43.8 mm. The periodicity along x, y, z, axes were L_x = 63 mm, L_y = 1.5 mm, and L_z = 63 mm, respectively. On the other hand, to obtain a stop band at 1800 MHz, the structure parameters of SRR were chosen as c = 1.8 mm, d = 0.6 mm, g = 0.6 mm, and l = 34.2 mm. The periodicity along x, y, z, axes were L_x = 50 mm, L_y = 1.5 mm, and L_z = 50 mm, respectively. Both the thickness and dielectric constant of the circuit board for operating at 900 MHz and 1800 MHz were 0.508 mm and 3.38, respectively. The size of the designed SRRs can also be reduced with the use of high dielectric constant circuit board. As shown in Fig. 3.2.8, the SRRs medium can display a stop band at 900 MHz and 1800 MHz after properly designing structure parameters.

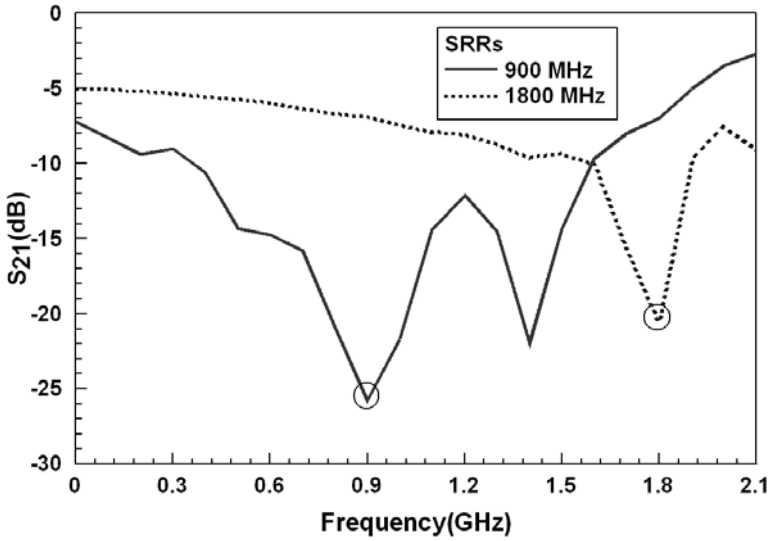

Fig. 3.2.8 Modeled transmission spectra of the designed SRRs.

It is known that a simple frequency selective surface (FSS) can also be used to obtain a stop band. In [41-43], a number of FSS are proposed for antenna application. In [43], the authors also proposed capacitively loaded loop (CLL) structure which is similar to SRR for antenna application. However, these structures display a stop band at several GHz. We have tried to use high impedance surface structure [41] to reduce the peak SAR. However, we found that when these structures are operated at 900 MHz, the sizes of these structures are too large for cellular phone application. A negative permittivity medium can also be constructed by arranging the metallic thin wires periodically [10]. However, we found that when the thin wires are operated at 900

MHz, the size is also too large for practical application. Because the SRR structures are resonant due to internal capacitance and inductance, they are on a scale less than the wavelength of radiation. In this study, it is found that the SRRs can be designed at 900MHz while the size is similar to that of cellular phone.

3.2.3 SAR Calculation in a Muscle Cube

The designed SRRs were used to reduce the SAR value. Since a 3-D model of the whole head with the presence of SRRs structure requires a great amount of memory in FDTD computation, a simplified muscle cube is studied to validate the effect of SAR reduction. Fig. 3.2.9 shows the muscle cube used in SAR simulation. It was formed by muscle tissue with $\varepsilon_r = 51.8$, $\sigma = 1.11$, and $\rho = 1040$ at 900 MHz and $\varepsilon_r = 49.4$, $\sigma = 1.53$, and $\rho = 1040$ at 1800 MHz. The distance between the antenna and the muscle cube was 25 mm. The designed SRRs were placed between the antenna and the muscle cube. The finite sized SRRs with $N_x = 1$, $N_y = 10$, and $N_z = 1$ unit elements along each direction were considered. The radiated power from the antenna was assumed to be 600 mW at 900 MHz and 125 mW at 1800 MHz, respectively. The size of the muscle cube was chosen equal to the length of the dipole antenna.

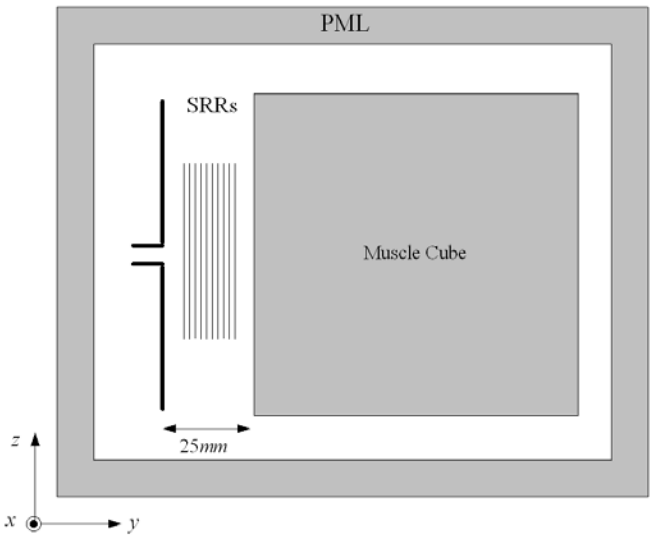

Fig. 3.2.9 Structure used in SAR calculation.

The peak SAR_{1g} and antenna performance with SRRs were studied. The results are given in Table 3.7. The radiated power from the antenna operated at 900 MHz was changed from 600 mW to 528.8 mW. The peak SAR_{1g} became 5.59 W/kg, a reduction of 36.8% with respect to the condition without SRRs. The antenna operated at 1800 MHz with SRRs was also studied. The radiated power changed to 119.2 mW and the peak SAR_{1g} became 0.54, a reduction of 44.3% with respect to the condition without SRRs. It is found that the radiated power is less affected while the peak SAR_{1g} is

reduced significantly with the designed SRRs.

Table 3.7 Effects of SRRs on the antenna performance and SAR reduction

	900 MHz		1800 MHz	
	No SRRs	With SRRs	No SRRs	With SRRs
Z_R	49.48 +*j*48.81	40.77+*j*49.04	63.30+*j*83.26	83.127+*j*91.88
P_R	600 mW	528.8 mW	125 mW	119.2 mW
SAR_{1g}	8.85	5.59	0.97	0.54

To study the effect of SAR reduction with the use of metamaterials, the radiated power from the dipole antenna with SRRs were fixed at 600 mW and 125 mW at 900 MHz and 1800 MHz operation bands, respectively. Numerical results of peak SAR_{1g} are shown in Table 3.8. The peak SAR_{1g} values with SRRs are reduced for 27.57% and 37.62% at 900 MHz and 1800 MHz, respectively. As a consequence, the designed SRRs can be used to reduce the EM interaction between the antenna and the muscle cube.

Table 3.8

Effect of SAR reduction for 900MHz and 1800MHz bands

(P_R = 0.6 W for 900 MHZ AND P_R = 0.125 W for 1800 MHZ)

Frequency	No SRRs	SRRs	Reduction %
900 MHz	8.85	6.41	27.57%
1800 MHz	0.97	0.605	37.62%

In general situation, the bandwidth used for mobile communications is 5% or so. The effect of SAR reduction with the designed SRRs on the 5% frequency bandwidth was studied. Table 3.9 shows the numerical results. Compared to the peak SAR values without SRRs at 900 MHz and 1800 MHz, the performance of SAR reduction on the 5% frequency bandwidth is also significant.

Table 3.9 Effects of SAR reduction on 5% frequency band for 900MHz and1800MHz

	877 MHz	922 MHz	1755 MHz	1845 MHz
Peak SAR_{1g}	5.85	5.24	0.398	0.464

3.3 Discussion

In this work, we have reduced the EM interaction between the antenna and the human head with metamaterials. Based on the 3-D FDTD method with lossy Drude model, it is found that the peak SAR_{1g} in the head can be reduced by placing the metamaterials between the antenna and the human head. The antenna performances can be less affected with the use of metamaterials. Comparisons with other SAR reduction techniques are also demonstrated. We also designed metamaterials from periodically arrangement of split ring resonators (SRRs). By properly designing structure parameters, the stop band of SRRs can be designed at 900 MHz and 1800 MHz bands of the cellular phone. The peak SAR_{1g} in a simplified muscle cube with the presence of the designed SRRs is studied and a significant reduction can be obtained. The designed SRRs also have good performance of SAR reduction on 5% frequency bandwidth. Numerical results can provide useful information in designing communication equipments for safety compliance.

Chapter 4

Stability Analysis of Absorbing Boundary Condition for ADI-FDTD Method

In this chapter, stability analysis of the absorbing boundary conditions (ABCs) for alternating direction implicit (ADI) finite-difference time-domain (FDTD) method is demonstrated. First, the stability analysis of the Mur's first order ABC in the ADI-FDTD method is presented. To analysis the stability of this scheme, the amplification matrix is derived. The effect of wave propagation direction on the stability of this scheme is investigated. The numerical dispersion relation of this scheme is also derived analytically from the amplification matrix. From the theoretical stability analysis and numerical simulation, it is found that the Mur's first order ABC in the ADI-FDTD method will be unstable.

On the other hand, the stability analysis of the split-field PML for ADI-FDTD is studied. The amplification matrix of this scheme is also derived based on the Von Neumann method. From the stability analysis, it is found that the split-field PML scheme for ADI-FDTD will be unstable at the PML interface and inside the PML regions. The instability of this scheme inside the PML regions can be improved with the modified PML conductivity profile. The theoretical results are validated by means of numerical simulations.

The ADI-FDTD method can be seen as a second order perturbation of the Crank-Nicolson FDTD (CN-FDTD) scheme. The difference between the CN-FDTD and ADI-FDTD is the Δt^2 perturbation term. When the PML is introduced for the ADI-FDTD method, the perturbation term will affect the stability of the ADI-FDTD method. In this work, the stability analysis of the PML schemes for the ADI-FDTD and CN-FDTD are demonstrated. It is found that the split-field PML and unsplit-field PML for ADI-FDTD method can lead to unstable condition due to the perturbation term.

The proposed modified PML conductivity profiles can improve the stability of split-field PML scheme for ADI-FDTD method. Numerical simulations of the VLSI interconnect and RF inductor in time domain and frequency domain will be demonstrated to show the efficiency and accuracy of this method

4.1 Analysis of Stability and Numerical Dispersion Relation of Mur's Absorbing Boundary Condition in the ADI-FDTD Method

4.1.1 Stability Analysis of the Mur's First Order ABC in the ADI-FDTD

The stability of the Mur's ABC in the ADI-FDTD method is studied. For simplicity, we consider the 2-D TM ADI-FDTD. This scheme at the $y = j_{\max\text{-}1}$ grid boundary is illustrated. Based on [20], the formulations of H_x, H_y, and E_z components in the first updating step are

$$H_{x\,i,j\,\max-1/2}^{n+1/2} = H_{x\,i,j\,\max-1/2}^{n} - \frac{\Delta t}{2\mu\Delta y}\left(E_{z\,i,j\,\max}^{n} - E_{z\,i,j\,\max-1}^{n}\right) \tag{4.1.1}$$

$$H_{y\,i+1/2,j\,\max-1}^{n+1/2} = H_{y\,i+1/2,j\,\max-1}^{n} + \frac{\Delta t}{2\mu\Delta x}\left(E_{z\,i+1,j\,\max-1}^{n+1/2} - E_{z\,i,j\,\max-1}^{n+1/2}\right) \tag{4.1.2}$$

$$\begin{aligned} E_{z\,i,j\,\max-1}^{n+1/2} = E_{z\,i,j\,\max-1}^{n} &+ \frac{\Delta t}{2\varepsilon\Delta x}\left(H_{y\,i+1/2,j\,\max-1}^{n+1/2} - H_{y\,i-1/2,j\,\max-1}^{n+1/2}\right) \\ &- \frac{\Delta t}{2\varepsilon\Delta y}\left(H_{x\,i,j\,\max-1/2}^{n} - H_{x\,i,j\,\max-3/2}^{n}\right) \end{aligned} \tag{4.1.3}$$

and in the second updating step

$$H_{x\,i,j\,\max-1/2}^{n+1} = H_{x\,i,j\,\max-1/2}^{n+1/2} - \frac{\Delta t}{2\mu\Delta y}\left(E_{z\,i,j\,\max}^{n+1} - E_{z\,i,j\,\max-1}^{n+1}\right) \tag{4.1.4}$$

$$H_{y\,i+1/2,j\,\max-1}^{n+1} = H_{y\,i+1/2,j\,\max-1}^{n+1/2} + \frac{\Delta t}{2\mu\Delta x}\left(E_{z\,i+1,j\,\max-1}^{n+1/2} - E_{z\,i,j\,\max-1}^{n+1/2}\right) \tag{4.1.5}$$

$$\begin{aligned} E_{z\,i,j\,\max-1}^{n+1} = E_{z\,i,j\,\max-1}^{n+1/2} &+ \frac{\Delta t}{2\varepsilon\Delta x}\left(H_{y\,i+1/2,j\,\max-1}^{n+1/2} - H_{y\,i-1/2,j\,\max-1}^{n+1/2}\right) \\ &- \frac{\Delta t}{2\varepsilon\Delta y}\left(H_{x\,i,j\,\max-1/2}^{n+1} - H_{x\,i,j\,\max-3/2}^{n+1}\right) \end{aligned} \tag{4.1.6}$$

where Δt and Δx are the time step size and cell size, respectively.

The Mur's ABC [34] is implemented at the boundary $y = j_{\max}$. The ADI schemes of the Mur's ABC are based on the formulations in [22]. As an explicit direction in the first updating step, the wave equation is written as

$$\frac{\partial}{\partial t} E_{z\,i,j_{\max-1/2}}^{n+1/4} = v_{\max} \frac{\partial}{\partial y} E_{z\,i,j_{\max-1/2}}^{n+1/4} \tag{4.1.7}$$

From (4.1.7), the field component E_z at the boundary $y = j_{\max}$ can be written as

$$E_{z\,i,j\,\max}^{n+1/2} = E_{z\,i,j\,\max-1}^{n} + \left(\frac{v_{\max}\Delta t - 2\Delta y}{v_{\max}\Delta t + 2\Delta y}\right)\left(E_{z\,i,j\,\max-1}^{n+1/2} - E_{z\,i,j\,\max}^{n}\right) \tag{4.1.8}$$

On the other hand, as an implicit direction in the second updating step, the wave equation is written as

$$\frac{\partial}{\partial t} E_{z\,i,j_{\max-1/2}}^{n+3/4} = v_{\max} \frac{\partial}{\partial y} E_{z\,i,j_{\max-1/2}}^{n+1} \tag{4.1.9}$$

From (4.1.9), the implementation of the Mur's first order ABC for the ADI-FDTD should be applied inside the tridiagonal matrix, the field component E_z at the boundary $y = j_{\max}$ becomes

$$E_{z\,i,j\,\max}^{n+1}\left(1 + \frac{v_{\max}\Delta t}{\Delta y}\right) + E_{z\,i,j\,\max-1}^{n+1}\left(1 - \frac{v_{\max}\Delta t}{\Delta y}\right) = \left(E_{z\,i,j\,\max-1}^{n+1/2} + E_{z\,i,j\,\max}^{n+1/2}\right) \tag{4.1.10}$$

Due to the adoption of the Mur's first order ABC at the boundary, the $E_{z\ i,j\max}$ expression in (4.1.10) is substituted into (4.1.1) and (4.1.4), respectively. The H_x components become

$$\begin{aligned} H_{x\,i,j\,\max-1/2}^{n+1/2} &= H_{x\,i,j\,\max-1/2}^{n} \\ &- \frac{\Delta t}{2\mu\Delta y}\left(-E_{z\,i,j\,\max-1}^{n}\left(\frac{2\Delta y}{\Delta y + v_{\max}\Delta t}\right) + \left(E_{z\,i,j\,\max}^{n-1/2} + E_{z\,i,j\,\max-1}^{n-1/2}\right)\left(\frac{\Delta y}{\Delta y + v_{\max}\Delta t}\right)\right) \end{aligned} \tag{4.1.11}$$

$$H_{x\,i,j\max-1/2}^{n+1} = H_{x\,i,j\max-1/2}^{n+1/2} - \frac{\Delta t}{2\mu\Delta y}\left(-E_{z\,i,j\max-1}^{n+1}\left(\frac{2\Delta y}{\Delta y + v_{\max}\Delta t}\right) + \left(E_{z\,i,j\max}^{n+1/2} + E_{z\,i,j\max-1}^{n+1/2}\right)\left(\frac{\Delta y}{\Delta y + v_{\max}\Delta t}\right)\right) \tag{4.1.12}$$

As shown in [20], the stability analysis of the ADI-FDTD method is studied from deriving the amplification matrix or the amplification factor for the two updating steps of this scheme. To derive the amplification matrix for the first updating step, the relation of field components at *nth* time step and (*n*+1/2)*th* time step in the system of the first updating equations are employed. However, the H_x at (*n*+1/2)th time step is calculated from the E_z components at (*n*-1/2)th time step and *n*th time step, as shown in (4.1.11). To write this equation into the matrix from *nth* time step and (*n*+1/2)*th* time step, we need to introduce the amplification factor ξ for E_z components at (*n*-1/2)th time step and rewrite (4.1.11) to be

$$H_{x\,i,j\max-1/2}^{n+1/2} = H_{x\,i,j\max-1/2}^{n} - \frac{\Delta t}{2\mu\Delta y}\left(-E_{z\,i,j\max-1}^{n}\left(\frac{2\Delta y}{\Delta y + v_{\max}\Delta t}\right) + \frac{1}{\xi}\left(E_{z\,i,j\max}^{n} + E_{z\,i,j\max-1}^{n}\right)\left(\frac{\Delta y}{\Delta y + v_{\max}\Delta t}\right)\right) \tag{4.1.13}$$

Since ξ is the amplification factor from (*n*-1/2)th time step to *n*th time step, it is identical to the amplification factor of the second updating step. As a result, the first updating equations (4.1.2), (4.1.3), and (4.1.13) can be formulated in the matrix form.

The numerical stability of this scheme is determined with the Fourier method. The spatial frequencies are assumed to be k_x, k_y, and k_z along the *x*, *y*, and *z* directions, and the field components in the spatial spectral domain are

$$E_{z\,i,j}^{n} = E_z^n e^{j(k_x i\Delta x + k_y j\Delta y)} \tag{4.1.14}$$

$$H_{x\,i,j+\frac{1}{2}}^{n} = H_x^n e^{j(k_x i\Delta x + k_y (j+\frac{1}{2})\Delta y)} \tag{4.1.15}$$

$$H_{y\,i+\frac{1}{2},j}^{n} = H_y^n e^{j(k_x (i+\frac{1}{2})\Delta x + k_y j\Delta y)} \tag{4.1.16}$$

After substituting these equations for the first updating equations, we can obtain

$$H_x^{n+1/2} = H_x^n + \left(\frac{\Delta t}{2\mu\Delta y}\left(\frac{2\Delta y}{\Delta y + v_{\max}\Delta t}\right)\exp\left\{-j\left(k_y\Delta y/2\right)\right\} - \frac{\frac{\Delta t}{\mu\Delta y}\cos\left(k_y\Delta y/2\right)\left(\frac{\Delta y}{\Delta y + v_{\max}\Delta t}\right)}{\xi}\right)E_z^n \tag{4.1.17}$$

$$H_y^{n+1/2} = H_y^n + j\frac{\Delta t}{\mu\Delta x}\sin\left(k_x\Delta x/2\right)E_z^{n+1/2} \tag{4.1.18}$$

$$E_z^{n+1/2} = E_z^n + j\frac{\Delta t}{\varepsilon\Delta x}\sin\left(k_x\Delta x/2\right)H_y^{n+1/2} - j\frac{\Delta t}{\varepsilon\Delta y}\sin\left(k_y\Delta y/2\right)H_x^n \tag{4.1.19}$$

Denote the field vector in the spatial spectral domain as

$$\mathrm{X}^n = \left[E_z^n \quad H_x^n \quad H_y^n\right]^T \tag{4.1.20}$$

The time marching relation of the field components can be written in a matrix form as

$$\mathrm{X}^{n+\frac{1}{2}} = M_1^{-1}P_1\mathrm{X}^n = \Lambda_1\mathrm{X}^n \tag{4.1.21}$$

where

$$M_1 = \begin{bmatrix} 1 & 0 & -j\dfrac{\Delta t}{\varepsilon \Delta x}\sin\left(\dfrac{k_x \Delta x}{2}\right) \\ 0 & 1 & 0 \\ -j\dfrac{\Delta t}{\mu \Delta x}\sin\left(\dfrac{k_x \Delta x}{2}\right) & 0 & 1 \end{bmatrix}$$

$$P_1 = \begin{bmatrix} 1 & -j\dfrac{\Delta t}{\varepsilon \Delta y}\sin\left(\dfrac{k_y \Delta y}{2}\right) & 0 \\ \dfrac{\Delta t}{2\mu \Delta y}\left(\dfrac{2\Delta y}{\Delta y + v_{\max}\Delta t}\right)e^{-jk_y \Delta y/2} + \dfrac{-\dfrac{\Delta t}{\mu \Delta y}\cos\left(\dfrac{k_y \Delta y}{2}\right)\left(\dfrac{\Delta y}{\Delta y + v_{\max}\Delta t}\right)}{\xi} & 1 & 0 \\ 0 & 0 & 1 \end{bmatrix}$$

The growth factor for the first updating step is the eigenvalues of Λ_1. It can be found that the ξ is one element of the matrix P_1. Similar procedure can be applied to the second updating equations (4.1.5), (4.1.6), and (4.1.12), the field components for the second updating equations from (n+1/2)*th* time step to (n+1)*th* time step can also be written in a matrix form

$$\mathrm{X}^{n+1} = M_2^{-1} P_2 \mathrm{X}^{n+\frac{1}{2}} = \Lambda_2 \mathrm{X}^{n+\frac{1}{2}} \tag{4.1.22}$$

where

$$M_2 = \begin{bmatrix} 1 & j\dfrac{\Delta t}{\varepsilon \Delta y}\sin\left(\dfrac{k_y \Delta y}{2}\right) & 0 \\ -\dfrac{\Delta t}{2\mu \Delta y}\left(\dfrac{2\Delta y}{\Delta y + v_{\max}\Delta t}\right)e^{-jk_y \Delta y/2} & 1 & 0 \\ 0 & 0 & 1 \end{bmatrix}$$

$$P_2 = \begin{bmatrix} 1 & 0 & j\dfrac{\Delta t}{\varepsilon \Delta x}\sin\left(\dfrac{k_x \Delta x}{2}\right) \\ -\dfrac{\Delta t}{\mu \Delta y}\cos\left(\dfrac{k_y \Delta y}{2}\right)\left(\dfrac{\Delta y}{\Delta y + v_{\max}\Delta t}\right) & 1 & 0 \\ j\dfrac{\Delta t}{\mu \Delta x}\sin\left(\dfrac{k_x \Delta x}{2}\right) & 0 & 1 \end{bmatrix}$$

The growth factorξ for the second updating step is the eigenvalues of Λ_2. Combing the two half time steps can lead to one time step

$$X^{n+1} = \Lambda_1 \Lambda_2 X^n = \Lambda X^n \tag{4.1.23}$$

In this work, the ξ value is solved first to obtain the matrix Λ.When the matrix Λ is obtained, the amplification factor for the total updating step can be found. The stability of this scheme requires that the eigenvalues of Λ lie within or on the unit circle, i.e., $|\lambda_\Lambda| \le 1$. Due to the complexity of the amplification matrix Λ, it is difficult to get a simplified analytical expression for the eigenvalues. The eigenvalues are

numerically calculated by Matlab®. The amplification matrix Λ is a function of the discrete wavenumber. All propagation directions are considered to study the stability of this scheme. Let $k_x = k\sin\phi$, $k_y = k\cos\phi$, and $k = \sqrt{k_x^2 + k_y^2}$; angle ϕ is incident angle with respective to the *y* axis.

To study the stability of this scheme, a 2-D computation domain is studied and the ratio of $\Delta t/\Delta t_{max}$ is defined as the CFL number (CFLN). The cell size with $\Delta x = \Delta y =$ 1.0 mm and FDTD time step size limit Δt_{max}=2.35 *ps* are used. The stability of this scheme with different propagation direction and time step size is investigated. The calculated maximum eigenvalues of Λ for different time step size and wave propagation direction are shown in Fig. 4.1.1.

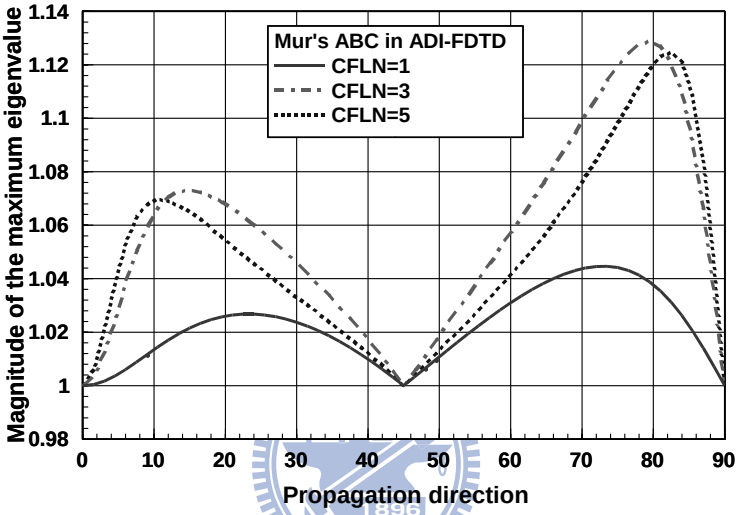

Figure 4.1.1 The maximum eigenvalues for different propagation direction.

The eigenvalues of this scheme will be smaller than unity only when the propagation directions are at ϕ=0°, 45°, and 90° and will become unstable at other propagation directions. It can also be found that the eigenvalues are larger than unity even when CFLN = 1 is used. In a practical ADI-FDTD simulation, the electromagnetic wave will not propagate at a specific direction when it reaches the absorbing boundary condition. Since the ADI scheme of the Mur's ABC is unstable, the field components at the boundary will become unstable.

4.1.2 Numerical Dispersion Relation

In this section, the numerical dispersion of the ADI-FDTD is studied. The time step size of the conventional FDTD needs to set to satisfy the Courant-Friedrich-Levy (CFL) stability condition but the time step size for the ADI-FDTD can set to be as large as the FDTD one. The time step size for the ADI-FDTD is not restricted by the grid side but by the numerical dispersion.

The calculated and measured transmission loss of the power plane is studied, as

shown in Fig. 4.1.2. The Mur's first order absorbing boundary conditions are applied on the outer surface. For conventional FDTD simulation, the grid size Δx = 2mm, Δy = 2mm, and Δz = 1.6 mm are used. The maximum time step size Δt =3.5 ps is used to meet the stability condition. For ADI-FDTD simulation, both $3\Delta t$ and $5\Delta t$ time step are used for comparison.

As shown in Fig. 4.1.2, the calculated transmission loss of the FDTD is similar to the measured data although its response is shifted downward slighted in term of frequency. Comparing the results of the ADI-FDTD method with the FDTD method, we can see that there are differences depending on the time step size, as shown in Table 4.1. The difference is due to the numerical dispersion. It can be seen, quantitatively, that the increase in time step size resulted in a reduction of the resonant frequency. As mentioned, the tradeoff resulting from an increase in time step size, which effects a reduction in CPU time, is an increase in numerical errors. The ADI-FDTD method will have advantage over the FDTD method if a model with smaller grid is studied.

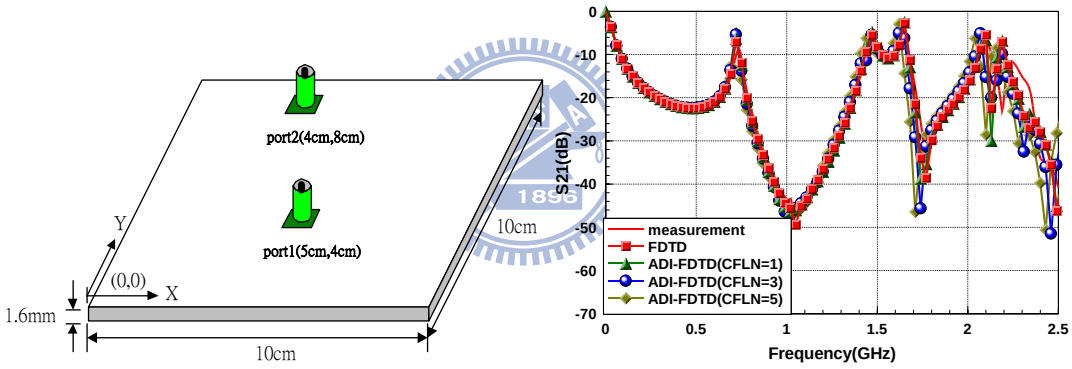

Figure 4.1.2 Transmission characteristics for power plane study.

Table 4.1

Calculated resonant frequency for different schemes

	Measured	FDTD	ADI-FDTD (CFLN=1)	ADI-FDTD (CFLN=3)	ADI-FDTD (CFLN=5)
frequency (GHz)	2.12	2.10	2.10	2.07	2.04
Difference		0.94%	0.94%	2.35%	3.77%

4.1.3 Numerical Simulation

Numerical verifications of instabilities are performed by 3-D ADI-FDTD with Mur's first order ABC. In this study, a uniform mesh with cell size $\Delta x = \Delta y = \Delta z =$ 1.0 mm and the maximum FDTD time step $\Delta t_{max} = 1.92 \times 10^{-12}\ s$ are used. The computation domain is $42 \times 42 \times 42$. The Mur's first order ABCs are applied on the six sides of the computation domain. A differential Gaussian pulse is launched for E_z component. The source is excited at the center position (21, 21, 21) and the observation point is positioned at (21, 20, 21). Numerical simulations of the ADI-FDTD with Mur's ABC for different CFLN are demonstrated. The ADI-FDTD method can be efficient only when large CFLN is used. This scheme with CFLN =3 and CFLN = 5 are studied, as shown in Fig. 4.1.3 and Fig 4.1.4, respectively. It can be found that instability of this scheme will appear after running 1300 time steps and 600 time steps for CFLN = 3 and CFLN = 5, respectively. With the implementation of the Mur's ABC in the ADI-FDTD method, this scheme will become unstable with less time steps when larger CFLN is used.

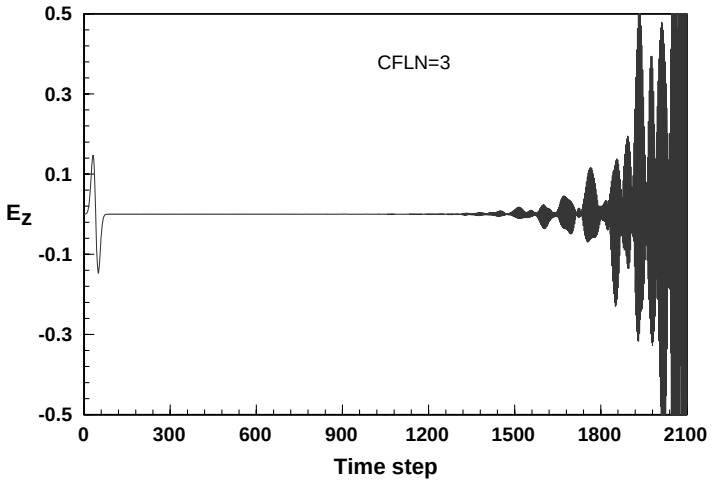

Figure 4.1.3 Numerical simulation of the ADI-FDTD with Mur's ABC (CFLN=3).

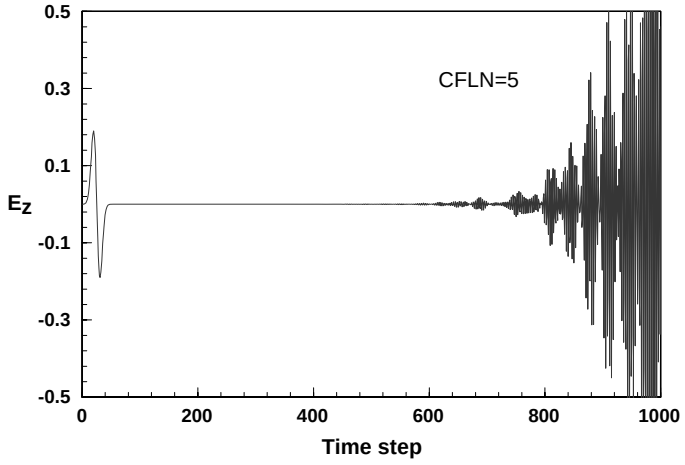

Figure 4.1.4 Numerical simulation of the ADI-FDTD with Mur's ABC (CFLN=5).**4.2**

4.2 A Modified PML Conductivity Profile for the ADI-FDTD Method with Split-field PML

4.2. 1 Theoretical Amplification Matrix

In this section, the amplification matrix of the ADI-FDTD method with split-field PML is derived. For simplicity, a 2-D TM ADI-FDTD is studied. In this scheme, the field components E_{zx}, E_{zy}, H_x, and H_y for the first updating procedure can be written as

$$E_{zy_{i,j}}^{n+\frac{1}{2}} = C_{ay} \cdot E_{zy_{i,j}}^{n} - C_{by} \cdot (H_{x_{i,j+\frac{1}{2}}}^{n} - H_{x_{i,j-\frac{1}{2}}}^{n}) \tag{4.2.1}$$

$$\begin{aligned} & E_{zx_{i,j}}^{n+\frac{1}{2}}\left(1 + C_{bx}D_{bx,1} + C_{bx}D_{bx,2}\right) - E_{zx_{i+1,j}}^{n+\frac{1}{2}} C_{bx}D_{bx,1} - E_{zx_{i-1,j}}^{n+\frac{1}{2}} C_{bx}D_{bx,2} \\ & = C_{ax} \cdot E_{zx_{i,j}}^{n} \\ & + C_{bx} \cdot \left(D_{ax,1} \cdot H_{y_{i+1/2,j}}^{n} - D_{ax,2} \cdot H_{y_{i-1/2,j}}^{n}\right) \\ & - E_{zy_{i,j}}^{n+\frac{1}{2}}\left(C_{bx}D_{bx,1} + C_{bx}D_{bx,2}\right) + E_{zy_{i+1,j}}^{n+\frac{1}{2}} C_{bx}D_{bx,1} + E_{zy_{i-1,j}}^{n+\frac{1}{2}} C_{bx}D_{bx,2} \end{aligned} \tag{4.2.2}$$

$$H_{x_{i,j+\frac{1}{2}}}^{n+\frac{1}{2}} = D_{ay,1} \cdot H_{x_{i,j+\frac{1}{2}}}^{n} - D_{by,1} \cdot (E_{zx_{i,j+1}}^{n} + E_{zy_{i,j+1}}^{n} - E_{zx_{i,j}}^{n} - E_{zy_{i,j}}^{n}) \tag{4.2.3}$$

$$H_{y_{i+\frac{1}{2},j}}^{n+\frac{1}{2}} = D_{ax,1} \cdot H_{y_{i+\frac{1}{2},j}}^{n} + D_{bx,1} \cdot (E_{zx_{i+1,j}}^{n+\frac{1}{2}} + E_{zy_{i+1,j}}^{n+\frac{1}{2}} - E_{zx_{i,j}}^{n+\frac{1}{2}} - E_{zy_{i,j}}^{n+\frac{1}{2}}) \tag{4.2.4}$$

where $C_{as} = \dfrac{1 - \dfrac{\sigma_s \Delta t}{4\varepsilon}}{1 + \dfrac{\sigma_s \Delta t}{4\varepsilon}}$ $C_{bs} = \dfrac{\dfrac{\Delta t}{2\varepsilon \Delta s}}{1 + \dfrac{\sigma_s \Delta t}{4\varepsilon}}$

$D_{as,n} = \dfrac{1 - \dfrac{\sigma_{s,n}^{*} \Delta t}{4\mu}}{1 + \dfrac{\sigma_{s,n}^{*} \Delta t}{4\mu}}$ $D_{bs,n} = \dfrac{\dfrac{\Delta t}{2\mu \Delta s}}{1 + \dfrac{\sigma_{s,n}^{*} \Delta t}{4\mu}}$ $s = x, y;\ n = 1, 2$

$\sigma^{*}_{x,1} = \sigma^{*}_{x\ i+1/2,j}$, $\sigma^{*}_{x,2} = \sigma^{*}_{x\ i-1/2,j}$, $\sigma^{*}_{y,1} = \sigma^{*}_{y\ i,j+1/2}$, $\sigma^{*}_{y,2} = \sigma^{*}_{y\ i,j-1/2}$

Since the electric conductivity σ and magnetic conductivity σ^{*} within the PML are usually scaled for small reflection, the PML parameters σ and σ^{*} in these equations will be position-dependent. In this study, the amplification matrix is derived using the actual updating equations of field components to capture the effect of the PML conductivity profile.

Similarly, for the second updating procedure, the field components can be written as

$$E_{zx_{i,j}}^{n+1} = C_{ax} \cdot E_{zx_{i,j}}^{n+1/2} + C_{bx} \cdot (H_{y_{i+\frac{1}{2},j}}^{n+\frac{1}{2}} - H_{y_{i-\frac{1}{2},j}}^{n+\frac{1}{2}}) \tag{4.2.5}$$

$$
\begin{aligned}
&E_{zy_{i,j}}^{n+1}\left(1+C_{by}D_{by,1}+C_{by}D_{by,2}\right)-E_{zy_{i,j+1}}^{n+1}C_{by}D_{by,1}-E_{zy_{i,j-1}}^{n+1}C_{by}D_{by,2}\\
&=C_{ay}\cdot E_{zy_{i,j}}^{n+1/2}\\
&-C_{by}\cdot\left(D_{ay,1}\cdot H_{x_{i,j+1/2}}^{n+1/2}-D_{ay,2}\cdot H_{x_{i,j-1/2}}^{n+1/2}\right)\\
&-E_{zx_{i,j}}^{n+1}\left(C_{by}D_{by,1}+C_{by}D_{by,2}\right)+E_{zx_{i,j+1}}^{n+1}C_{by}D_{by,1}+E_{zy_{i,j-1}}^{n+1}C_{by}D_{by,2}
\end{aligned}
\tag{4.2.6}
$$

$$
H_{x_{i,j+\frac{1}{2}}}^{n+1}=D_{ay,1}\cdot H_{x_{i,j+\frac{1}{2}}}^{n+1/2}-D_{by,1}\cdot\left(E_{zx_{i,j+1}}^{n+1}+E_{zy_{i,j+1}}^{n+1}-E_{zx_{i,j}}^{n+1}-E_{zy_{i,j}}^{n+1}\right)
\tag{4.2.7}
$$

$$
H_{y_{i+\frac{1}{2},j}}^{n+1}=D_{ax,1}\cdot H_{y_{i+\frac{1}{2},j}}^{n+1/2}+D_{bx,1}\cdot\left(E_{zx_{i+1,j}}^{n+\frac{1}{2}}+E_{zy_{i+1,j}}^{n+\frac{1}{2}}-E_{zx_{i,j}}^{n+\frac{1}{2}}-E_{zy_{i,j}}^{n+\frac{1}{2}}\right)
\tag{4.2.8}
$$

We assume the spatial frequencies to be k_x, k_y, and k_z along the x, y, and z directions and the field components in the spatial spectral domain can be written as

$$
E_{zx_{i,j}}^{n}=E_{zx}^{n}e^{-j(k_x i\Delta x+k_y j\Delta y)}
\tag{4.2.9}
$$

$$
E_{zy_{i,j}}^{n}=E_{zy}^{n}e^{-j(k_x i\Delta x+k_y j\Delta y)}
\tag{4.2.10}
$$

$$
H_{x_{i,j+\frac{1}{2}}}^{n}=H_{x}^{n}e^{-j(k_x i\Delta x+k_y (j+\frac{1}{2})\Delta y)}
\tag{4.2.11}
$$

$$
H_{y_{i+\frac{1}{2},j}}^{n}=H_{y}^{n}e^{-j(k_x (i+\frac{1}{2})\Delta x+k_y j\Delta y)}
\tag{4.2.12}
$$

After substituting these equations into (4.2.1)-(4.2.4), we can obtain

$$
\begin{aligned}
&E_{zx}^{n+\frac{1}{2}}\left(1+C_{bx}\cdot 2j\cdot D_{bx,1}\cdot\sin\left(\frac{k_x\Delta x}{2}\right)e^{-j\frac{k_x\Delta x}{2}}-C_{bx}\cdot 2j\cdot D_{bx,2}\cdot\sin\left(\frac{k_x\Delta x}{2}\right)e^{j\frac{k_x\Delta x}{2}}\right)\\
&=C_{ax}\cdot E_{zx}^{n}\\
&+C_{bx}\cdot\left(D_{ax,1}\cdot H_{y}^{n}e^{-j\frac{k_x\Delta x}{2}}-D_{ax,2}\cdot H_{y}^{n}e^{+j\frac{k_x\Delta x}{2}}\right)\\
&+C_{bx}\cdot\left(-2j\cdot D_{bx,1}\cdot\sin\left(\frac{k_x\Delta x}{2}\right)e^{-j\frac{k_x\Delta x}{2}}+C_{bx}\cdot 2j\cdot D_{bx,2}\cdot\sin\left(\frac{k_x\Delta x}{2}\right)e^{j\frac{k_x\Delta x}{2}}\right)\cdot E_{zy}^{n+\frac{1}{2}}
\end{aligned}
\tag{4.2.13}
$$

$$
E_{zy}^{n+\frac{1}{2}}=C_{ay}\cdot E_{zy}^{n}+2j\cdot C_{by}\cdot\sin\left(\frac{k_y\Delta y}{2}\right)\cdot H_{x}^{n}
\tag{4.2.14}
$$

$$
H_{x}^{n+\frac{1}{2}}=D_{ay,1}\cdot H_{x}^{n}+2j\cdot D_{by,1}\cdot\sin\left(\frac{k_y\Delta y}{2}\right)\cdot\left(E_{zx}^{n}+E_{zy}^{n}\right)
\tag{4.2.15}
$$

$$
H_{y}^{n+\frac{1}{2}}=D_{ax,1}\cdot H_{y}^{n}-2j\cdot D_{bx,1}\cdot\sin\left(\frac{k_x\Delta x}{2}\right)\cdot\left(E_{zx}^{n+\frac{1}{2}}+E_{zy}^{n+\frac{1}{2}}\right)
\tag{4.2.16}
$$

Denote the field vector in the spatial spectral domain as

$$
X^{n}=\left[E_{zx}^{n}\quad E_{zy}^{n}\quad H_{x}^{n}\quad H_{y}^{n}\right]^{T}
\tag{4.2.17}
$$

The time marching relation of field vector can be written in a matrix form as

$$M_1 \mathrm{X}^{n+\frac{1}{2}} = P_1 \mathrm{X}^{n} \tag{4.2.18}$$

where

$$M_1 = \begin{bmatrix} \begin{pmatrix} 1+C_{bx}\cdot 2j\cdot D_{bx1}\cdot\sin\left(\frac{k_x\Delta x}{2}\right)e^{-j\frac{k_x\Delta x}{2}} \\ -C_{bx}\cdot 2j\cdot D_{bx2}\cdot\sin\left(\frac{k_x\Delta x}{2}\right)e^{j\frac{k_x\Delta x}{2}} \end{pmatrix} & \begin{pmatrix} C_{bx}\cdot 2j\cdot D_{bx1}\cdot\sin\left(\frac{k_x\Delta x}{2}\right)e^{-j\frac{k_x\Delta x}{2}} \\ -C_{bx}\cdot 2j\cdot D_{bx2}\cdot\sin\left(\frac{k_x\Delta x}{2}\right)e^{j\frac{k_x\Delta x}{2}} \end{pmatrix} & \begin{matrix} 0 & 0 \\ 0 & 0 \end{matrix} \\ \begin{matrix} 0 \\ 0 \end{matrix} & \begin{matrix} 1 \\ 0 \end{matrix} & \begin{matrix} 0 & 0 \\ 1 & 0 \end{matrix} \\ 2j\cdot D_{bx,1}\cdot\sin\left(\frac{k_x\Delta x}{2}\right) & 2j\cdot D_{bx,1}\cdot\sin\left(\frac{k_x\Delta x}{2}\right) & 0 \quad 1 \end{bmatrix}$$

$$P_1 = \begin{bmatrix} C_{ax} & 0 & 0 & C_{bx}\cdot\begin{pmatrix} D_{ax1}\cdot e^{-j\frac{k_x\Delta x}{2}} \\ -D_{ax2}\cdot e^{j\frac{k_x\Delta x}{2}} \end{pmatrix} \\ 0 & C_{ay} & 2j\cdot C_{by}\cdot\sin\left(\frac{k_y\Delta y}{2}\right) & 0 \\ 2j\cdot D_{by,1}\cdot\sin\left(\frac{k_y\Delta y}{2}\right) & 2j\cdot D_{by,1}\cdot\sin\left(\frac{k_y\Delta y}{2}\right) & D_{ay,1} & 0 \\ 0 & 0 & 0 & D_{ax,1} \end{bmatrix}$$

We can apply the same procedure for the second updating equations.

$$M_2 \mathrm{X}^{n+1} = P_2 \mathrm{X}^{n+\frac{1}{2}} \tag{4.2.19}$$

where

$$M_2 = \begin{bmatrix} 1 & 0 & \begin{matrix} 0 & 0 \\ 0 & 0 \end{matrix} \\ \begin{pmatrix} C_{by}\cdot 2j\cdot D_{by1}\cdot\sin\left(\frac{k_y\Delta y}{2}\right)e^{-j\frac{k_y\Delta y}{2}} \\ -C_{by}\cdot 2j\cdot D_{by2}\cdot\sin\left(\frac{k_y\Delta y}{2}\right)e^{j\frac{k_y\Delta y}{2}} \end{pmatrix} & \begin{pmatrix} 1+C_{by}\cdot 2j\cdot D_{by1}\cdot\sin\left(\frac{k_y\Delta y}{2}\right)e^{-j\frac{k_y\Delta y}{2}} \\ -C_{by}\cdot 2j\cdot D_{by2}\cdot\sin\left(\frac{k_y\Delta y}{2}\right)e^{j\frac{k_y\Delta y}{2}} \end{pmatrix} & \begin{matrix} 0 & 0 \\ 0 & 0 \end{matrix} \\ -2j\cdot D_{by,1}\cdot\sin\left(\frac{k_y\Delta y}{2}\right) & -2j\cdot D_{by,1}\cdot\sin\left(\frac{k_y\Delta y}{2}\right) & \begin{matrix} 1 & 0 \\ 0 & 1 \end{matrix} \\ 0 & 0 & \end{bmatrix}$$

$$P_2 = \begin{bmatrix} C_{ax} & 0 & 0 & -2j\cdot C_{bx}\cdot\sin\left(\frac{k_x\Delta x}{2}\right) \\ 0 & C_{ay} & C_{by}\cdot\begin{pmatrix} D_{ay1}\cdot e^{-j\frac{k_y\Delta y}{2}} \\ -D_{ay2}\cdot e^{j\frac{k_y\Delta y}{2}} \end{pmatrix} & 0 \\ 0 & 0 & D_{ay,1} & 0 \\ -2j\cdot D_{bx,1}\cdot\sin\left(\frac{k_x\Delta x}{2}\right) & -2j\cdot D_{bx,1}\cdot\sin\left(\frac{k_x\Delta x}{2}\right) & 0 & D_{ax,1} \end{bmatrix}$$

We combine the two half time steps to one time step

$$X^{n+1} = M_2^{-1} P_2 M_1^{-1} P_1 X^{n} = \Lambda X^{n} \tag{4.2.20}$$

It can be found that not only $\sigma^*_{\text{xi+1/2,j}}$ and $\sigma^*_{\text{y i,j+1/2}}$ but also $\sigma^*_{\text{xi-1/2,j}}$ and $\sigma^*_{\text{y i,j-1/2}}$ are within the amplification matrix Λ. The stability criterion requires that the eigenvalues of Λ lie within or on the unit circle, i.e., $|\lambda_\Lambda| \le 1$.

4.2.2 Stability Analysis

For the stability analysis of this scheme, the eigenvalues of amplification matrix are evaluated. Due to the complexity of the amplification matrix Λ, it is difficult to get the simplified analytical expression for the eigenvalues. The eigenvalues are numerically

calculated by *Matlab*. The stability matrix is a function of the discrete wavenumber. Since the stability must be independent of the angle of wave propagation, all angles must be considered. We find that the maximum eigenvalues occur when $\sin\left(k_s \Delta s / 2\right) = 1$, s = x, y, z.

A 2-D computation domain contains 42×42 cells is studied. The cell size with $\Delta x = \Delta y = 1.0$ mm and FDTD time step limit Δt_{max}=2.35 *ps* are used. Ten layers of PML are used in x and y direction. The parameters of PML are chosen the same as those in [25]. The polynomial scaling is used for the PML conductivity profile

$$\sigma_{s\max} = \sigma_{opt} \approx \frac{(m+1)}{150\pi\Delta s}$$

$$\sigma_s(s) = \frac{\sigma_{s\max}\left|s - s_0\right|^m}{d^m} \qquad s = x, y, z \tag{4.2.21}$$

where d is the thickness of PML absorber, Δs is the cell size, and s_0 represents the interface. In this simulation, we choose $m = 4$ and $\sigma_{max} = 10.61$S/m for optimum PML performance [25].

In order to validate the proposed amplification matrix, the eigenvalues of amplification matrix are computed for free space condition $\sigma = \sigma^* = 0$ and PML medium with same conductivity $\sigma = \sigma_{max}$. The time step size is $5\Delta t_{max}$. As shown in Table 4.1, this scheme will be stable on these conditions since all eigenvalues are smaller than unity.

Table 4.2

Eigenvalues of Λ for free space and PML mediums $\sigma = \sigma_{max}$

	Free space $\sigma = 0$	PML medium $\sigma = \sigma_{max}$
$\lvert\lambda_\Lambda\rvert$	1.0000000e+000	8.7121313e-001
	1.0000000e+000	8.7121313e-001
	1.0000000e+000	4.8417857e-001
	1.0000000e+000	4.8417857e-001

The ADI-FDTD method with the conventional PML conductivity profile (4.2.21) is studied. Since the σ and σ^* within the PML become position-dependent, the amplification matrix will also be different for different PML coefficients. The eigenvalues of amplification matrix are computed for four PML coefficients, as shown in Fig. 4.2.1 Position 1 is located at free space. The positions within the PML mediums are studied. Position 2 is located at the interface between PML and free space where $\sigma^*_{y\,i,j+1/2} = 0$ and $\sigma^*_{y\,i,j-1/2} = 30.1592$. Position 3 is located at the first layer of PML where $\sigma^*_{y\,i,j+1/2} = 30.1592$ and $\sigma^*_{y\,i,j-1/2} = 934.9371$. Position 4 is located at the

eighth layer of PML where $\sigma^*_{y\,i,j+1/2} = 481372.0127$ and $\sigma^*_{y\,i,j-1/2} = 792615.6173$. The $\sigma_x = \sigma_x^* = 0$ is used for the four positions.

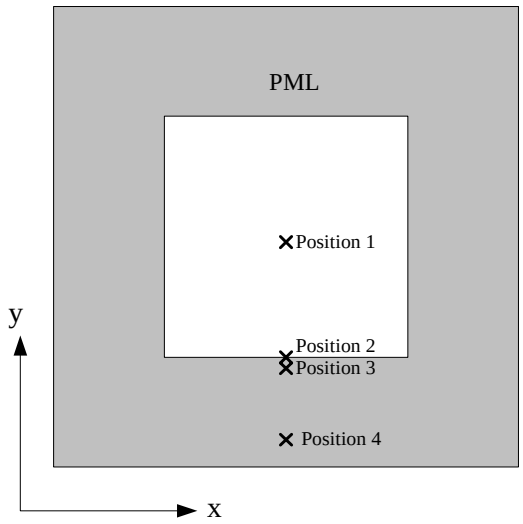

Figure 4.2.1 Four positions for eigenvalue calculation.

The calculated eigenvalues of Λ for different time steps and positions are shown in Table 4.2. We have tested different values for the numerical accuracy to be certain that round-off error does not affect the calculated eigenvalues. As shown in Table 4.2, it is found that the maximum eigenvalue increases with the grow of the time step. This scheme will be unstable at Position 2 and Position 3 because the eigenvalues are larger than unity. In [28], it was commented that the instability of the ADI-FDTD method with the split-field PML is unavoidable. The eigenvalue of this scheme with time step size less than the CFL limit is also investigated. It can bee seen that some eigenvalues are larger than unity at Position 2 and Position 3 even the time step $0.9\Delta t_{max}$ is used.

Table 4.3 Eigenvalues of Λ for 2D ADI-FDTD with PML

	Position 1 (21, 20)	Position 2 (21, 10)	Position 3 (21, 9)	Position 4 (21, 2)
$0.9\Delta t_{max}$	1.0000000e+000	9.9999985e-001	9.9991584e-001	6.9932975e-001
	1.0000000e+000	9.9999985e-001	9.9991584e-001	6.9932975e-001
	1.0000000e+000	1.0000000e+000	9.9977724e-001	6.4315304e-001
	1.0000000e+000	1.0000021e+000	1.0000735e+000	6.4315304e-001
Δt_{max}	1.0000000e+000	9.9999977e-001	9.9990957e-001	6.8325119e-001
	1.0000000e+000	9.9999977e-001	9.9990957e-001	6.8325119e-001
	1.0000000e+000	1.0000000e+000	9.9974524e-001	6.1599183e-001
	1.0000000e+000	1.0000028e+000	1.0001031e+000	6.1599183e-001

2 Δt_{max}	1.0000000e+000	9.9999766e-001	9.9983507e-001	5.8437802e-001
	1.0000000e+000	9.9999766e-001	9.9983507e-001	5.8437802e-001
	1.0000000e+000	1.0000000e+000	9.9940408e-001	3.9758804e-001
	1.0000000e+000	1.0000141e+000	1.0005628e+000	3.9758804e-001
4 Δt_{max}	1.0000000e+000	9.9998999e-001	9.9960137e-001	7.2137644e-001
	1.0000000e+000	9.9998999e-001	9.9960137e-001	5.0510375e-001
	1.0000000e+000	1.0000000e+000	9.9871437e-001	5.0510375e-001
	1.0000000e+000	1.0000451e+000	1.0017621e+000	1.5426083e-002

4.2.3 Modified PML Conductivity Profiles

The PML conductivity profile will affect the stability of the ADI-FDTD method with the split-field PML. As shown in Table 4.2, it is found that all the eigenvalues are smaller than unity at Position 4. We find that there are two conditions for this scheme to be stable inside the PML regions. For the first condition, the ratio of the successive magnetic conductivities in the PML should be small. For the second condition, the electric and magnetic conductivities inside the PML regions should be large enough. Since the PML conductivity is increased from the PML interface to the PEC boundary, we find that the ratio of the successive magnetic conductivities in the PML close to the PML interface should be smaller than 1.3 and that close to the PEC boundary should be smaller than 1.5 to avoid the instability.

The effect of the conductivity profile on the stability of this scheme is investigated. Two modified conductivity profiles are studied, as shown in Fig. 4.2.2. For the first modified conductivity profiles, the σ_{max} = 10.61S/m and the ratio of the successive magnetic conductivities inside the PML regions are arranged as

$$\frac{\sigma^*_{x,2}}{\sigma^*_{x,1}} = \frac{\sigma^*_{y,2}}{\sigma^*_{y,1}} = 1.3 \quad (\text{From } 1^{\text{st}} \text{ layer to } 3^{\text{rd}} \text{ layer})$$

$$\frac{\sigma^*_{x,2}}{\sigma^*_{x,1}} = \frac{\sigma^*_{y,2}}{\sigma^*_{y,1}} = 1.4 \quad (\text{From } 4^{\text{th}} \text{ layer to } 5^{\text{th}} \text{ layer})$$

$$\frac{\sigma^*_{x,2}}{\sigma^*_{x,1}} = \frac{\sigma^*_{y,2}}{\sigma^*_{y,1}} = 1.5 \quad (\text{From } 6^{\text{th}} \text{ layer to } 10^{\text{th}} \text{ layer}) \qquad (4.2.22)$$

The increase of the PML conductivity of (4.2.22) is not polynomially scaled. Therefore the PML performance with the first modified PML conductivity profile (4.2.22) will be significantly affected. A second modified PML conductivity profile with a constant scaling factor m is proposed. In this modified PML conductivity profile, the successive PML conductivity is scaled using the polynomial function (4.2.21) with σ_{max} = 21.22S/m and m = 2

$$\sigma_s(s) = \frac{\sigma_{s\max}|s - s_0|^2}{d^2} \quad s = x, y, z \qquad (4.2.23)$$

The corresponding normal reflection coefficient $R(0)$ of (4.2.23) is 6.8×10^{-24} which is much smaller than the conventional value. Comparisons between the conventional PML conductivity profile (4.2.21), the first modified conductivity profile (4.2.22) and the second modified conductivity profile (4.2.23) are shown in Fig 4.2.2.

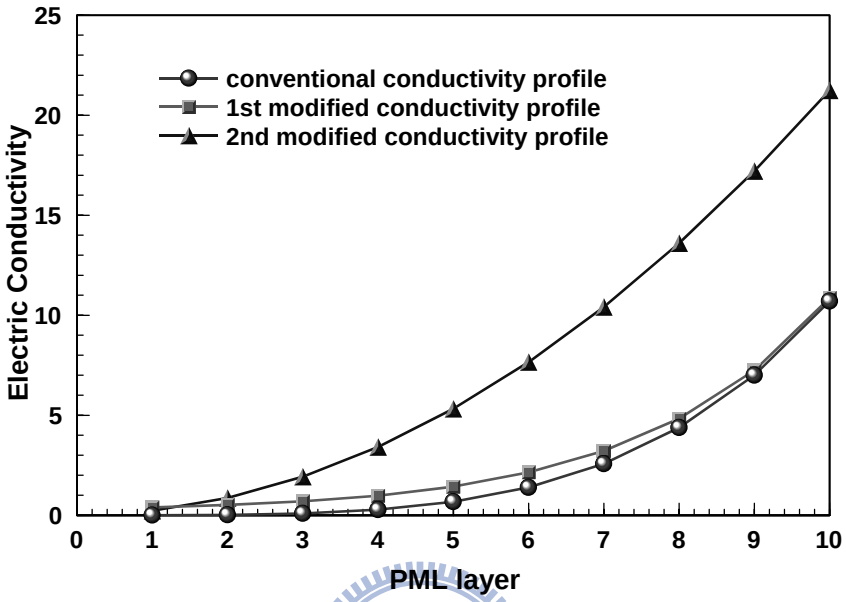

Figure 4.2.2 Conductivity profiles for the PML mediums.

The same 2-D computation domain is studied. The time step is $5\Delta t_{max}$. The calculated eigenvalues of this scheme with different conductivity profiles at different positions are shown in Table 4.3. First, the PML medium with the same conductivity σ = 10.61 is studied. It is found that this scheme can be stable inside the PML regions. However, the maximum eigenvalue at the (21, 10) is larger than unity. The instability of this scheme at the PML interface is unavoidable. Although the instability inside the PML regions can be improved, this scheme will suffer from lager reflection errors since the conductivity is not increased from the PML interface to the PEC boundary. The conventional conductivity profile (4.2.21) for optimum PML performance is studied. As shown in Table 4.3, this scheme will be unstable from position (21, 10) to position (21, 3) and become stable from position (21, 2) with the conventional conductivity profile. This is because the ratio of the successive magnetic conductivities in the PML layers can be less than 1.5 only at the regions close to the PEC boundary.

Table 4.4
The calculated eigenvalues of Λ for different conductivity profiles

	Position (21,10)	Position (21,9)	Position (21,8)	Position (21,7)	Position (21,6)	Position (21,3)	Position (21,2)
PML	8.3167465e-001	8.7121313e-001	8.7121313e-001	8.7121313e-001	8.7121313e-001	8.7121313e-001	8.7121313e-001
medium	8.3167465e-001	8.7121313e-001	8.7121313e-001	8.7121313e-001	8.7121313e-001	8.7121313e-001	8.7121313e-001
$\sigma = 10.61$	1.0000000e+00	4.8417857e-001	4.8417857e-001	4.8417857e-001	4.8417857e-001	4.8417857e-001	4.8417857e-001
	2.2607177e+00	4.8417857e-001	4.8417857e-001	4.8417857e-001	4.8417857e-001	4.8417857e-001	4.8417857e-001
Conventional	9.9998595e-001	9.9947387e-001	9.9501294e-001	9.7672831e-001	9.2963950e-001	8.0873543e-001	8.5231622e-001
conductivity	9.9998595e-001	9.9947387e-001	9.9501294e-001	9.7672831e-001	9.2963950e-001	3.4158314e-001	5.8450767e-001
profile	1.0000607e+00	1.0023617e+000	9.8273693e-001	9.2571923e-001	7.9713001e-001	5.3701283e-002	5.1407068e-001
	1.0000000e+00	9.9837472e-001	1.0149820e+000	1.0462747e+000	1.0958000e+00	1.0400832e+00	3.3159060e-002
1st modified	9.7912834e-001	8.8457772e-001	8.5285313e-001	8.4633346e-001	8.8028977e-001	7.7235998e-001	5.7646377e-001
conductivity	9.7912834e-001	8.8457772e-001	8.5285313e-001	7.7764778e-001	6.3334230e-001	8.6715348e-001	5.7646377e-001
profile	1.0952721e+00	7.6986223e-001	7.1107860e-001	6.1748176e-001	5.0285471e-001	2.5298972e-001	7.4761908e-001
	1.0000000e+00	9.8777229e-001	9.8155369e-001	9.9755841e-001	9.8509416e-001	1.2658093e-002	8.5740395e-002
2nd modified	9.9540604e-001	9.5110019e-001	8.1956499e-001	8.3465030e-001	9.2765962e-001	8.4492806e-001	9.0538676e-001
conductivity	9.9540604e-001	9.5110019e-001	8.1956499e-001	4.6990210e-001	7.5040601e-001	8.4492806e-001	9.0538676e-001
profile	1.0200902e+00	8.1340254e-001	4.9000128e-001	1.7718996e-001	3.0547466e-001	4.7954231e-001	5.2417697e-001
	1.0000000e+00	1.1607705e+000	1.2344384e+000	1.1379080e+000	1.7064586e-002	4.7954231e-001	5.2417697e-001

The ADI-FDTD method with the modified PML conductivity profile is studied. For the first modified conductivity profile (4.2.22), it can be found that all the eigenvalues of this scheme are smaller than unity from position (21, 9) to position (21, 1), which means this scheme can be stable inside the PML. For the second modified conductivity profile (4.2.23), the ratio of the successive magnetic conductivities in the PML is smaller than 1.5 from position (21, 6) to position (21, 1). As shown in Table 4.3, the calculated eigenvalues of this scheme with the second modified conductivity profile can be stable in these positions. Compared to the conventional conductivity profile, the instability inside the PML region can also be improved significantly with the second modified conductivity profile.

The PML performances of this scheme with the modified conductivity profiles are studied. A differentiated Gaussian pulse is launched for the H_x component. The source excitation is located at (21, 21) and the observation position is located ten cells away from the excitation and close to the PML interface. The relative reflection error of the PML is evaluated by

$$R = 20\log_{10}\left(\frac{\left|H^t - H^t_{ref}\right|}{\max\left|H^t_{ref}\right|}\right) \tag{4.2.24}$$

where H^t is the H field component recorded at the observation point and H^t_{ref} is the reference value calculated from a large enough domain. The recorded H components for TM and TE wave are H_x and H_z fields. The calculated relative reflection error of the 2D TM and TE wave are shown in Fig 4.1.3a and Fig 4.1.3b, respectively. In the PML equations, the σ_y^* is used in the H_y equation and both the σ_x^* and σ_y^* are used in the H_{zx} and H_{zy} equations. Therefore, the calculated reflection errors of TM and TE wave are somewhat different. For the first modified PML conductivity profile (4.2.22), it is found that the PML performance will be deteriorated about 22 dB compared to the conventional PML scheme. For the second modified conductivity profile (4.2.23), the maximum reflection error is reduced around 12 dB for TM wave. The PML performance of the ADI-FDTD with the second modified PML conductivity profile is better than that with the first modified PML conductivity profile, as shown in Fig. 4.2.3. Although the PML performance of first modified PML conductivity profile can be improved by increasing the PML thickness, the corresponding conductivity will become small and the instability of this scheme will be increased. From Table 4.3, it is found that the ADI-FDTD scheme with the first modified PML conductivity profile will still be unstable in the vacuum-PML regions. The worse PML performance of first modified PML conductivity profile will make this scheme more unstable since the reflection wave from the boundary will be amplified in the unstable vacuum-PML regions.

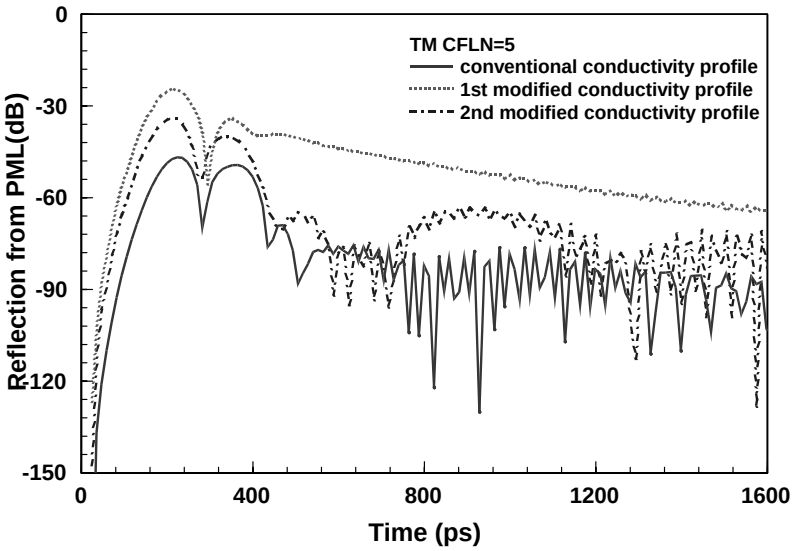

Figure 4.2.3a Relative reflection error of the TM ADI-FDTD method with PML ABC.

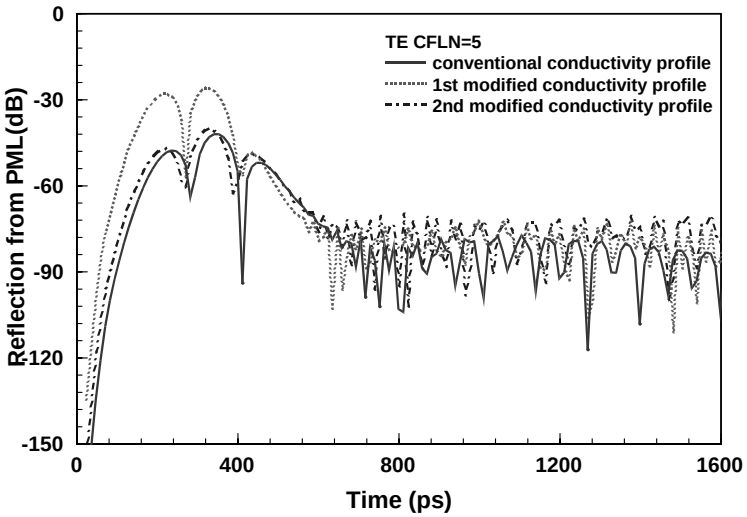

Figure 4.2.3b Relative reflection error of the TE ADI-FDTD method with PML ABC.

As shown in Table 4.3, the instability of the ADI-FDTD with PML can also be improved when the second modified PML conductivity profile is employed and the PML performance can still be maintained. The first modified conductivity can be viewed as a guideline for the design of the stable split-field PML. For considering the PML performance and the stability of this scheme, the second modified PML profile (4.2.23) is more suitable for ADI-FDTD simulation.

4.2.4 Numerical Simulation

The theoretical amplification matrix is derived based on the Von Neumann method. The Von Neumann method assumes the wave propagates in an unbound region. When the calculated eigenvalues of ADI-FDTD with split-field PML are larger than unity, it means that the electromagnetic field will be unstable in the homogenous region with these PML coefficients. Since the ADI scheme can be unstable with these PML coefficients, the ADI-FDTD with PML implementation can become unstable. To validate the instability of the ADI-FDTD with PML implementation, one method is to calculate the amplification matrix of the total computational domain. However, the amplification matrix of the total computational domain will be very complicated and is not suitable for other problems. The simple way to analyze the stability of the total computational domain can be accomplished by numerical simulations. In this section, the numerical tests of the ADI-FDTD method with split-field PML are performed. From the stability analysis, the ADI-FDTD method with split-field PML will be unstable at the vacuum-PML interface and inside the PML regions. For 2-D case, the eigenvalue is small and it requires a large number of time steps to make the field components unstable. Numerical simulation is performed by 3-D ADI-FDTD with split-field PML. A uniform mesh with cell size $\Delta x = \Delta y = \Delta z = 1.0$ mm and FDTD

time step limit Δt_{max}=1.92 ps are used. The computation domain is $42 \times 42 \times 42$. PML layers that are ten cells thick terminated all six sides of the computation domain. A differential Gaussian pulse applied to H_x field is excited at the center position (21, 21, 21) and the time step size in this study is $5\Delta t_{max}$. First, the numerical simulation of this scheme with the conventional PML conductivity profile (4.2.21) is performed. Fig. 4.2.4 shows the time-domain H_x fields recorded at the position (21, 20, 21). As shown in Fig 4.2.4, this scheme will become unstable after running 3500 time steps.

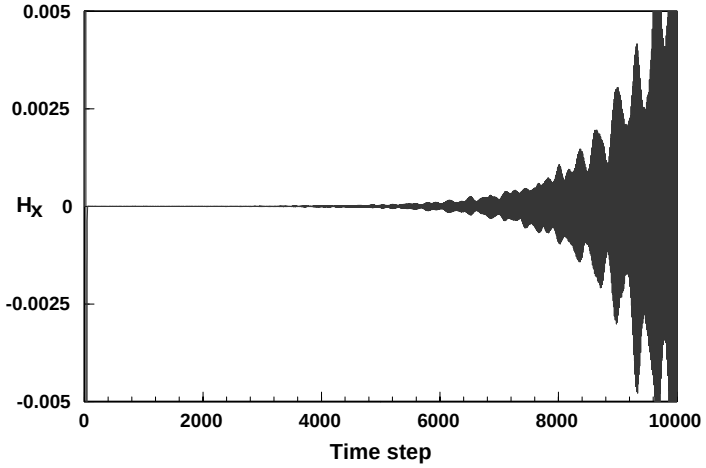

Figure 4.2.4 The H_x component with the conventional conductivity profile.

For considering the theoretical stability analysis and PML performance, the ADI-FDTD method with the second modified PML conductivity profile (4.2.23) is studied. Fig. 4.2.5 shows the simulated time-domain H_x fields. No instability is observed after running 15000 time steps. Although there are several eigenvalues larger than unity and the PML performance will be affected for the second modified conductivity profile, it is found that the stability of this scheme can be significantly improved.

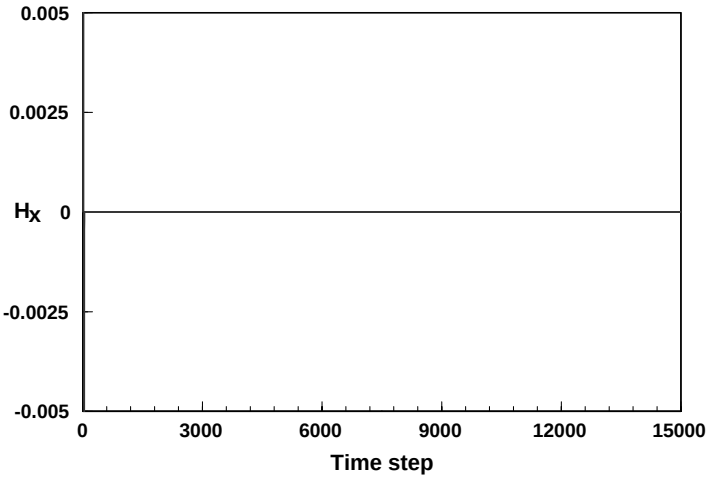

Figure 4.2.5 The H_x component with the modified PML conductivity profile.

4.3 PML for CN-FDTD and ADI-FDTD

The ADI-FDTD can be seen as a second order perturbation of CN-FDTD. Their formulations are described briefly. The Maxwell's curl equations are given by

$$\partial_t \vec{E} = \frac{1}{\varepsilon}\tilde{\Re}\vec{H} \qquad \partial_t \vec{H} = -\frac{1}{\mu}\tilde{\Re}\vec{E} \tag{4.3.1}$$

where ε and μ are the permittivity and permeability, respectively. $\vec{E}$ and $\vec{H}$ are the electric and magnetic fields, and $\tilde{\Re}$ is the curl operator in Cartesian coordinates. One can replace all the derivatives by centered difference operator and average the field affected by the curl operator to derive the CN-FDTD scheme,

$$\left(\vec{\Psi}^{n+1} - \vec{\Psi}^{n}\right) = \tilde{\Re}_T \frac{\Delta t}{2}\left(\vec{\Psi}^{n+1} + \vec{\Psi}^{n}\right) \tag{4.3.2}$$

where $\vec{\Psi} = \left(E_x \quad E_y \quad E_z \quad H_x \quad H_y \quad H_z\right)^T$ is the numerical vector field and the operator $\tilde{\Re}_T$ is the numerical counterpart of $\tilde{\Re}$. Equation (4.3.2) is the CN-FDTD scheme. It will require large computational resources to solve this scheme. Nevertheless, the CN-FDTD can be reformulated to ADI-FDTD scheme that can be solved efficiently. Based on [31], the CN-FDTD method can be split into two step procedure for ADI-FDTD. The space operator $\tilde{\Re}_T$ is decomposed as

$$\tilde{A} + \tilde{B} = \tilde{\Re}_T \tag{4.3.3}$$

and (4.3.2) can be rewritten as

$$\left(\tilde{I} - \frac{\Delta t}{2}\left(\tilde{A} + \tilde{B}\right)\right)\vec{\Psi}^{n+1} = \left(\tilde{I} + \frac{\Delta t}{2}\left(\tilde{A} + \tilde{B}\right)\right)\vec{\Psi}^{n} \tag{4.3.4}$$

The CN-FDTD scheme (4.3.4) can be rewritten as

$$\begin{aligned}\left(\tilde{I} - \frac{\Delta t}{2}\tilde{A}\right)\left(\tilde{I} - \frac{\Delta t}{2}\tilde{B}\right)\vec{\Psi}^{n+1} &= \left(\tilde{I} + \frac{\Delta t}{2}\tilde{A}\right)\left(\tilde{I} + \frac{\Delta t}{2}\tilde{B}\right)\vec{\Psi}^{n} \\ &+ \frac{\Delta t^2}{4}\tilde{A}\tilde{B}\left(\vec{\Psi}^{n+1} - \vec{\Psi}^{n}\right)\end{aligned} \tag{4.3.5}$$

If we neglect the Δt^2 perturbation term, we can get the approximation of CN-FDTD as ADI-FDTD

$$\left(\tilde{I} - \frac{\Delta t}{2}\tilde{A}\right)\left(\tilde{I} - \frac{\Delta t}{2}\tilde{B}\right)\vec{\Psi}^{n+1} = \left(\tilde{I} + \frac{\Delta t}{2}\tilde{A}\right)\left(\tilde{I} + \frac{\Delta t}{2}\tilde{B}\right)\vec{\Psi}^{n} \tag{4.3.6}$$

Therefore, the ADI-FDTD scheme (4.3.6) can be seen as a second order perturbation of the CN-FDTD (4.3.2)

Equation (4.3.6) can be further split into two updating steps

$$\begin{aligned}\left(\tilde{I} - \frac{\Delta t}{2}\tilde{A}\right)\vec{\Psi}^{n*} &= \left(\tilde{I} + \frac{\Delta t}{2}\tilde{B}\right)\vec{\Psi}^{n}, \\ \left(\tilde{I} - \frac{\Delta t}{2}\tilde{B}\right)\vec{\Psi}^{n+1} &= \left(\tilde{I} + \frac{\Delta t}{2}\tilde{A}\right)\vec{\Psi}^{n*}\end{aligned} \tag{4.3.7}$$

where $\vec{\Psi}^{n*}$ is an auxiliary intermediate vector field. The ADI-FDTD equations (4.3.7)

can be solved efficiently.

To simulate unbounded region problems, the PML formulations should be implemented for CN-FDTD and ADI-FDTD. We can use the same procedure to reformulate the PML equations. We can use the same procedure to reformulate the PML equations. For the PML equations, the PML conductivity is incorporated into matrix $\tilde{\Re}_T$. Once we derive the operator $\tilde{\Re}_T$ and split into two operators $\tilde{A}$ and $\tilde{B}$, we can reformulate the PML equations for CN-FDTD and ADI-FDTD. In this study, the unsplit-field PML, split-field PML and CFS PML formulations for CN-FDTD and ADI-FDTD are investigated.

4.3.1. Unsplit-field PML Scheme

The unsplit-field PML scheme is based on the formulations derived in [28]. The unsplit form PML equations are

$$\partial_t \vec{E} = \frac{1}{\varepsilon}\tilde{\Re}\vec{H} - \frac{1}{\varepsilon}\tilde{\sigma}_o\vec{E} - \frac{1}{\varepsilon}(\tilde{\sigma}_e - \tilde{\sigma}_o)\vec{E}_e \tag{4.3.8}$$

$$\partial_t \vec{H} = -\frac{1}{\mu}\tilde{\Re}\vec{E} - \frac{1}{\varepsilon}\tilde{\sigma}_e\vec{H} + \frac{1}{\varepsilon}(\tilde{\sigma}_e - \tilde{\sigma}_o)\vec{H}_o \tag{4.3.9}$$

$$\partial_t \vec{E}_e = \frac{1}{\varepsilon}\tilde{\Re}_e\vec{H} - \frac{1}{\varepsilon}\tilde{\sigma}_e\vec{E}_e \tag{4.3.10}$$

$$\partial_t \vec{H}_o = -\frac{1}{\mu}\tilde{\Re}_o\vec{E} - \frac{1}{\varepsilon}\tilde{\sigma}_o\vec{H}_o \tag{4.3.11}$$

where ∂_u represents the partial derivative with respective to u direction, $\vec{E}_e$ and $\vec{H}_o$ are two auxiliary fields, and

$$\tilde{\Re} = \begin{pmatrix} 0 & -\partial_z & \partial_y \\ \partial_z & 0 & -\partial_x \\ -\partial_y & \partial_x & 0 \end{pmatrix}, \quad \tilde{\Re} = \tilde{\Re}_e + \tilde{\Re}_o$$

$$\tilde{\Re}_e = \begin{pmatrix} 0 & 0 & \partial_y \\ \partial_z & 0 & 0 \\ 0 & \partial_x & 0 \end{pmatrix} \quad \tilde{\Re}_o = \begin{pmatrix} 0 & -\partial_z & 0 \\ 0 & 0 & -\partial_x \\ -\partial_y & 0 & 0 \end{pmatrix}$$

$$\tilde{\sigma}_e = \begin{pmatrix} \sigma_y & 0 & 0 \\ 0 & \sigma_z & 0 \\ 0 & 0 & \sigma_x \end{pmatrix} \quad \tilde{\sigma}_o = \begin{pmatrix} \sigma_z & 0 & 0 \\ 0 & \sigma_x & 0 \\ 0 & 0 & \sigma_y \end{pmatrix} \tag{4.3.12}$$

(4.3.8)-(4.3.11) can be written in a compact form as

$$\partial_t \vec{\Psi}(t) = \tilde{\Re}_T \vec{\Psi}(t) \tag{4.3.13}$$

where $\Psi(t)$ is the compound Cartesian vector

$$\vec{\Psi} = \begin{pmatrix} E_x & E_y & E_z & H_x & H_y & H_z \\ E_{ex} & E_{ey} & E_{ez} & H_{ox} & H_{oy} & H_{oz} \end{pmatrix}^T \tag{4.3.14}$$

and

$$\tilde{\Re}_T = \begin{pmatrix} -\frac{1}{\varepsilon}\tilde{\sigma}_o & \frac{1}{\varepsilon}\tilde{\Re} & -\frac{1}{\varepsilon}(\tilde{\sigma}_e - \tilde{\sigma}_o) & \tilde{0} \\ -\frac{1}{\mu}\tilde{\Re} & -\frac{1}{\varepsilon}\tilde{\sigma}_e & \tilde{0} & \frac{1}{\varepsilon}(\tilde{\sigma}_e - \tilde{\sigma}_o) \\ \tilde{0} & \frac{1}{\varepsilon}\tilde{\Re}_e & -\frac{1}{\varepsilon}\tilde{\sigma}_e & \tilde{0} \\ -\frac{1}{\mu}\tilde{\Re}_o & \tilde{0} & \tilde{0} & -\frac{1}{\varepsilon}\tilde{\sigma}_o \end{pmatrix} \tag{4.3.15}$$

where $\tilde{I}$ and $\tilde{0}$ are 3×3 identity and null matrix, respectively.

The operators $\tilde{A}$ and $\tilde{B}$ are chosen so that

$$\tilde{A} + \tilde{B} = \tilde{\Re}_T \tag{4.3.16}$$

A possible choice of $\tilde{A}$ and $\tilde{B}$ is given by

$$\tilde{A} = \begin{pmatrix} \tilde{0} & \frac{1}{\varepsilon}\tilde{\Re}_e & -\frac{1}{\varepsilon}\tilde{\sigma}_e & \tilde{0} \\ -\frac{1}{\mu}\tilde{\Re}_o & \tilde{0} & \tilde{0} & -\frac{1}{\varepsilon}\tilde{\sigma}_o \\ \tilde{0} & \frac{1}{\varepsilon}\tilde{\Re}_e & -\frac{1}{\varepsilon}\tilde{\sigma}_e & \tilde{0} \\ -\frac{1}{\mu}\tilde{\Re}_o & \tilde{0} & \tilde{0} & -\frac{1}{\varepsilon}\tilde{\sigma}_o \end{pmatrix} \tag{4.3.17}$$

$$\tilde{B} = \begin{pmatrix} -\frac{1}{\varepsilon}\tilde{\sigma}_o & \frac{1}{\varepsilon}\tilde{\Re}_o & -\frac{1}{\varepsilon}\tilde{\sigma}_o & \tilde{0} \\ -\frac{1}{\mu}\tilde{\Re}_e & -\frac{1}{\varepsilon}\tilde{\sigma}_e & \tilde{0} & \frac{1}{\varepsilon}\tilde{\sigma}_e \\ \tilde{0} & \tilde{0} & \tilde{0} & \tilde{0} \\ \tilde{0} & \tilde{0} & \tilde{0} & \tilde{0} \end{pmatrix} \tag{4.3.18}$$

The field components $\vec{E}$, $\vec{H}$, $\vec{E}_e$ and $\vec{H}_o$ can be solved by CN-FDTD (4.3.4) or by two updating steps ADI-FDTD method (4.3.7). The system equation (4.3.7) can be further triangularized in order to solve it efficiently. When we set the PML conductivity $\sigma_x = \sigma_y = \sigma_z = 0$, $\vec{E}$ and $\vec{H}$ formulations will be identical to the ADI-FDTD method.

4.3.2 Split-field PML Scheme

The split-field PML formulations can also be expressed in the partial differential form (4.3.1) and solved by the CN-FDTD scheme. Based on [25], the field vector is defined as

$$\vec{\Psi} = \begin{pmatrix} E_{xy} & E_{yz} & E_{zx} & E_{xz} & E_{yx} & E_{zy} \\ H_{xy} & H_{yz} & H_{zx} & H_{xz} & H_{yx} & H_{zy} \end{pmatrix}^T \tag{4.3.19}$$

and $\tilde{\Re}_T$ is a 12×12 dimensional space operator

$$\tilde{\tilde{\Re}}_T = \begin{pmatrix} -\frac{1}{\varepsilon}\tilde{\tilde{\sigma}}_e & \tilde{\tilde{0}} & \frac{1}{\varepsilon}\tilde{\tilde{R}}_e & \frac{1}{\varepsilon}\tilde{\tilde{R}}_e \\ \tilde{\tilde{0}} & -\frac{1}{\varepsilon}\tilde{\tilde{\sigma}}_o & \frac{1}{\varepsilon}\tilde{\tilde{R}}_o & \frac{1}{\varepsilon}\tilde{\tilde{R}}_o \\ -\frac{1}{\mu}\tilde{\tilde{R}}_e & -\frac{1}{\mu}\tilde{\tilde{R}}_e & -\frac{1}{\varepsilon}\tilde{\tilde{\sigma}}_e & \tilde{\tilde{0}} \\ -\frac{1}{\mu}\tilde{\tilde{R}}_o & -\frac{1}{\mu}\tilde{\tilde{R}}_o & \tilde{\tilde{0}} & -\frac{1}{\varepsilon}\tilde{\tilde{\sigma}}_o \end{pmatrix} \tag{4.3.20}$$

$\tilde{\tilde{\Re}}_T$ can be split into two operators to derive ADI-FDTD scheme and the operators $\tilde{\tilde{A}}$ and $\tilde{\tilde{B}}$ are given by

$$\tilde{\tilde{A}} = \begin{pmatrix} -\frac{1}{2\varepsilon}\tilde{\tilde{\sigma}}_e & \tilde{\tilde{0}} & \frac{1}{\varepsilon}\tilde{\tilde{R}}_e & \frac{1}{\varepsilon}\tilde{\tilde{R}}_e \\ \tilde{\tilde{0}} & -\frac{1}{2\varepsilon}\tilde{\tilde{\sigma}}_o & \tilde{\tilde{0}} & \tilde{\tilde{0}} \\ \tilde{\tilde{0}} & \tilde{\tilde{0}} & -\frac{1}{2\varepsilon}\tilde{\tilde{\sigma}}_e & \tilde{\tilde{0}} \\ -\frac{1}{\mu}\tilde{\tilde{R}}_o & -\frac{1}{\mu}\tilde{\tilde{R}}_o & \tilde{\tilde{0}} & -\frac{1}{2\varepsilon}\tilde{\tilde{\sigma}}_o \end{pmatrix}$$

and

$$\tilde{\tilde{B}} = \begin{pmatrix} -\frac{1}{2\varepsilon}\tilde{\tilde{\sigma}}_e & \tilde{\tilde{0}} & \tilde{\tilde{0}} & \tilde{\tilde{0}} \\ \tilde{\tilde{0}} & -\frac{1}{2\varepsilon}\tilde{\tilde{\sigma}}_o & \frac{1}{\varepsilon}\tilde{\tilde{R}}_o & \frac{1}{\varepsilon}\tilde{\tilde{R}}_o \\ -\frac{1}{\mu}\tilde{\tilde{R}}_e & -\frac{1}{\mu}\tilde{\tilde{R}}_e & -\frac{1}{2\varepsilon}\tilde{\tilde{\sigma}}_e & \tilde{\tilde{0}} \\ \tilde{\tilde{0}} & \tilde{\tilde{0}} & \tilde{\tilde{0}} & -\frac{1}{2\varepsilon}\tilde{\tilde{\sigma}}_o \end{pmatrix} \tag{4.3.21}$$

Compared to the unsplit field PML scheme, the split field PML equation is less complicated and more straightforward. However, this formulation suffers from large reflection error when attempting to absorb low-frequency evanescent wave. The CFS PML scheme can efficiently absorb low-frequency wave and is discussed below.

4.4 Theoretical Stability Analysis

To study the stability of the PML schemes for the CN-FDTD and ADI-FDTD method, the Von Neumann method is employed. Following the similar procedures presented in [20], we assume that for each time step the field components are Fourier-transformed into the spatial spectral domain. From the system equations of (4.3.4), the CN-FDTD scheme can be written in the spatial spectral domain in a matrix form as

$$\mathrm{X}^{n+1} = G\mathrm{X}^{n} \tag{4.4.1}$$

where the vector X^n represents the field components and the auxiliary variables at the nth time step for different PML schemes. From the system equations of (4.3.7), the ADI-FDTD scheme can also be written in the spatial spectral domain in a matrix form as

$$M_1 X^{n^*} = P_1 X^n \tag{4.4.2}$$

$$M_2 X^{n+1} = P_2 X^{n^*} \tag{4.4.3}$$

for the n* and n+1 time steps, respectively. The entries for the matrices M and P are derived from updating equations. The two half time steps can be combined to one time step

$$X^{n+1} = M_2^{-1} P_2 M_1^{-1} P_1 X^n = \Lambda X^n \tag{4.4.4}$$

The stability criterion requires that the eigenvalues of amplification matrices G and Λ lie within or on the unit circle. An attempt to determine the eigenvalues of G and Λ symbolically was made. However, due to the complexity of the amplification matrix, it is difficult to get a simplified analytical expression for the eigenvalues. The maximum eigenvalues are numerically calculated by Matlab®. In this study, we set the cell size to be $\Delta x = \Delta y = \Delta z = 1.0$ mm and FDTD time step limit Δt_{max}=1.92 *ps* is used. The ratio of $\Delta t/\Delta t_{max}$ is defined as the CFL number (CFLN).

4.4.1 Unsplit-field PML Scheme

The eigenvalues of G and Λ are computed when $\sigma_x = \sigma_z$=0 and σ_y=10.66 S/m. The time step sizes are chosen to be Δt_{max}, $2\Delta t_{max}$, and $5\Delta t_{max}$, respectively. Both the unsplit field PML schemes for the CN-FDTD scheme and ADI-FDTD are investigated and the theoretical results are shown in Table 4.4. When CFLN = 1, both the ADI-FDTD and CN-FDTD PML formulations can be stable since the maximum eigenvalues for the two schemes are smaller than unity. However, it is found that the eigenvalues of the unsplit field PML scheme for ADI-FDTD scheme are larger than unity when CFLN = 2 is used. On the other hand, we use different CFLN and σ values and no instability was observed for CN-FDTD PML scheme. As shown in (4.3.5), the difference between CN-FDTD and ADI-FDTD is the Δt^2 perturbation term. The results indicate that perturbation term will affect the stability of PML scheme for ADI-FDTD when large CFLN is used.

Table 4.5

Eigenvalues of for Λ and G unsplit PML scheme

	CFLN=1	CFLN=2	CFLN=5
Unsplit-field PML for ADI-FDTD σ=10.66 $\lvert\lambda_\Lambda\rvert$	1.0000000e+000	1.0000000e+000	1.0000000e+000
	8.7747147e-001	1.0000000e+000	1.0000000e+000
	8.7747147e-001	1.1404158e+000	1.8425689e+000
	8.7747147e-001	1.1404158e+000	1.8425689e+000
	1.0000000e+000	1.0000000e+000	1.8425689e+000
	1.0000000e+000	1.0000000e+000	1.8425689e+000
	8.7747147e-001	1.1404158e+000	1.0000000e+000
	3.0475086e-001	1.1404158e+000	1.0000000e+000
	3.0475086e-001	4.3679841e-001	4.1123514e-001
	3.0475086e-001	4.3679841e-001	4.1123514e-001
	3.0475086e-001	4.3679841e-001	4.1123514e-001
	1.0000000e+000	4.3679841e-001	4.1123514e-001
Unsplit-field PML for CN-FDTD σ=10.66 $\lvert\lambda_G\rvert$	1.0000000e+000	1.0000000e+000	1.0000000e+000
	9.2402257e-001	9.2903235e-001	9.6195689e-001
	9.2402257e-001	9.2903235e-001	9.6195689e-001
	9.2402257e-001	9.2903235e-001	9.6195689e-001
	9.2402257e-001	9.2903235e-001	9.6195689e-001
	2.3259772e-001	4.6207853e-001	7.3695418e-001
	2.3259772e-001	4.6207853e-001	7.3695418e-001
	2.3259772e-001	4.6207853e-001	7.3695418e-001
	2.3259772e-001	4.6207853e-001	7.3695418e-001
	1.0000000e+000	1.0000000e+000	1.0000000e+000
	1.0000000e+000	9.9999998e-001	9.9999997e-001
	1.0000000e+000	1.0000000e+000	1.0000000e+000

4.4.2 Split-field PML Scheme

The split-field PML schemes for CN-FDTD and ADI-FDTD are studied. In [45], it indicated that the split-field PML for the ADI-FDTD method will be unstable when the PML conductivity profile is polynomial scaled and this scheme can be stable with constant PML conductivity. In this study, the smaller PML conductivity $\sigma_x = \sigma_z = 0$ and $\sigma_y = 0.1066$ S/m is used. From Table 4.5, it is found that the split-field PML scheme for ADI-FDTD can be stable when CFLN = 5 and will become unstable when large CFLN =15 is used. No instability is observed when split-field PML for CN-FDTD scheme is used.

Table 4.6

Eigenvalues of Λ and G for split PML scheme

	CFLN=1	CFLN=5	CFLN=15
split-field PML for ADI-FDTD σ=0.1066 $\lvert\lambda_\Lambda\rvert$	9.9422334e-001	9.9590080e-001	1.0066924e+000
	9.9422334e-001	9.9590080e-001	1.0066924e+000
	9.9422334e-001	9.9590080e-001	1.0066924e+000
	9.9422334e-001	9.9590080e-001	1.0066924e+000
	9.8563297e-001	9.4176082e-001	8.3275850e-001
	9.8563297e-001	9.4176082e-001	8.3275850e-001
	9.8563297e-001	9.4176082e-001	8.3275850e-001
	9.8563297e-001	9.4176082e-001	8.3275850e-001
	1.0000000e+000	1.0000000e+000	9.9999972e-001
	9.9999999e-001	1.0000000e+000	1.0000000e+000
	1.0000000e+000	9.9999996e-001	1.000000e+000
	1.0000000e+000	9.9999999e-001	9.9999999e-001
Split-field PML for CN-FDTD σ=0.1066 $\lvert\lambda_G\rvert$	9.9614053e-001	9.9851056e-001	9.9948561e-001
	9.9614053e-001	9.9851056e-001	9.9948561e-001
	9.9614053e-001	9.9851056e-001	9.9948561e-001
	9.9614053e-001	9.9851056e-001	9.9948561e-001
	9.8468627e-001	9.2575790e-001	7.9378279e-001
	9.8468627e-001	9.2575790e-001	7.9378279e-001
	9.8468627e-001	9.2575790e-001	7.9378279e-001
	9.8468627e-001	9.2575790e-001	7.9378279e-001
	1.0000000e+000	1.0000000e+000	9.9999986e-001
	1.0000000e+000	1.0000000e+000	9.9999996e-001
	9.9999999e-001	9.9999996e-001	1.000000e+000
	1.0000000e+000	9.9999998e-001	1.0000000e+000

4.5 Numerical Verification

Numerical simulations are performed by 3-D ADI-FDTD with unsplit-field PML and split-field PML to validate the instability of the two schemes. A uniform mesh with cell size $\Delta x = \Delta y = \Delta z = 1.0$ mm and FDTD time step limit Δt_{max}=1.92 ps are used. The computation domain is $42 \times 42 \times 42$. PML layers that are ten cells thick terminated all six sides of the computation domain. A differential Gaussian pulse applied to H_x field is excited at the center position (21, 21, 21). The polynomial scaling is used for the PML conductivity profile

$$\sigma_{s\max} = \sigma_{opt} \approx \frac{(m+1)}{150\pi\Delta s}$$

$$\sigma_s(s) = \frac{\sigma_{s\max}|s - s_0|^m}{d^m} \qquad s = x, y, z \tag{4.5.1}$$

where d is the thickness of PML absorber, Δs is the cell size, and s_0 represents the interface. In this simulation, we choose scaling factor m = 4 and $\sigma_{\max}$ = 10.61S/m for optimum PML performance [25].

First, numerical simulation of the ADI-FDTD with unsplit-field PML is performed. The time step size in this study is chosen to be $2\Delta t_{\max}$. Fig. 4.5.1 shows the time-domain H_x fields recorded at the position (21, 20, 21). As shown in Fig 4.5.1, this scheme will become unstable after running 400 time steps.

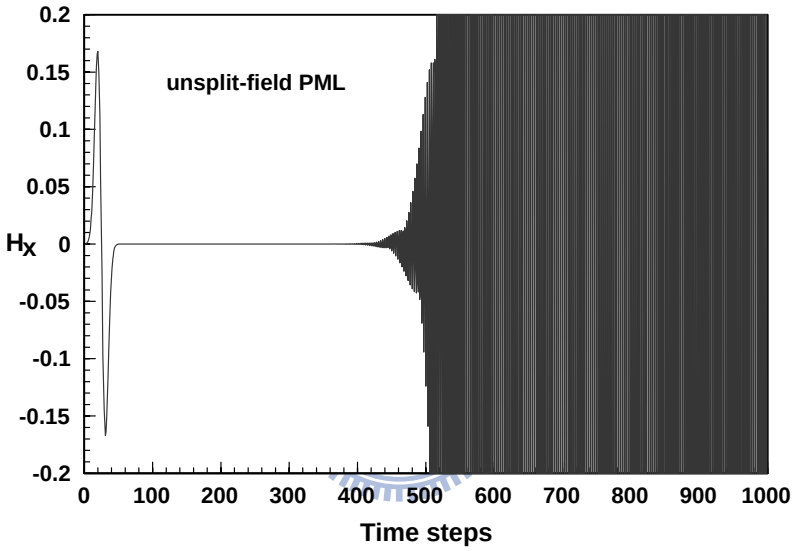

Figure 4.5.1 The H_x component for ADI-FDTD with unsplit-field PML (CFLN=2).

Then, numerical simulation of the ADI-FDTD with split-field PML is performed. The time step size in this study is $7\Delta t_{\max}$. As shown in Fig. 4.5.2, this scheme can also become unstable after running 1200 time steps.

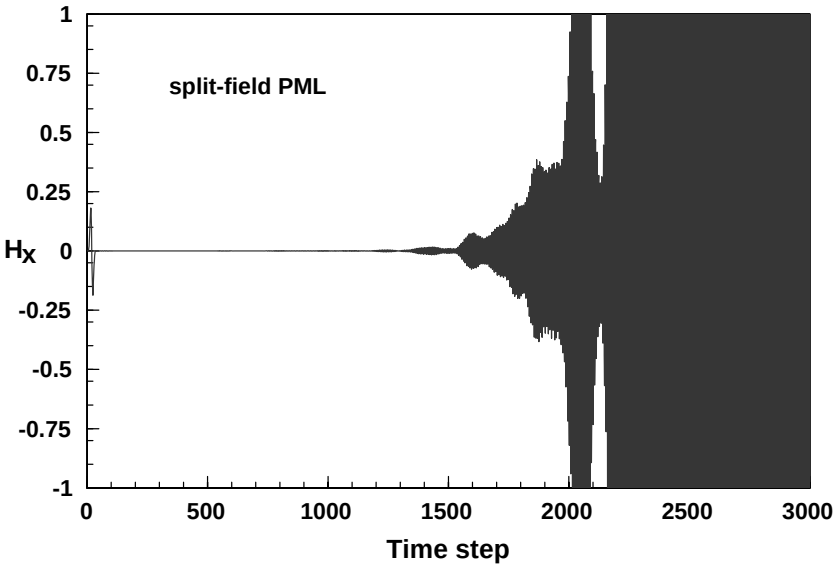

Figure 4.5.2 The H_x component for ADI-FDTD with split-field PML (CFLN=7).

From numerical simulation, it is found that the split-field PML scheme [25] and unsplit-field PML [28] scheme for ADI-FDTD can be unstable. The instability of the split-field PML and unsplit-field PML for ADI-FDTD can not be avoided but can be improved by using the modified PML conductivity profile [30].

4.6 Simulation of VLSI Circuits

From previous studies, it is found that the time step size of the ADI-FDTD method is not restricted by the CFL stability condition, but by the required numerical dispersion of this method. One of the factors that affect the numerical dispersion is the grid size. When employing the ADI-FDTD method for VLSI circuits modeling, the grid cell size will be micron-scale, which is much smaller than $1/10^{th}$ or $1/20^{th}$ of the smallest wavelength of interest. Therefore, the ADI-FDTD is well suited for VLSI circuits modeling since the numerical error of scheme can be small even large time step size is used. In this section, numerical simulations of the VLSI circuits including the multilevel crossover and RF inductor by ADI-FDTD method are demonstrated.

4.6.1 Multilevel Crossover in VLSI Interconnects

The coupling effect of the multilevel crossover in VLSI circuit is analyzed. The structure is taken from [44] and is shown in Fig. 4.6.1. The two-level crossover has two conductors in each level. The conductors are of copper with width 1 μm and thickness 1 μm, respectively. The five S_iO_2 layers are of thickness 1 μm and ε_r = 3.9 and covered by two ground conductors on the top and bottom. The line lengths and separations are 30.8 μm and 1 μm, respectively.

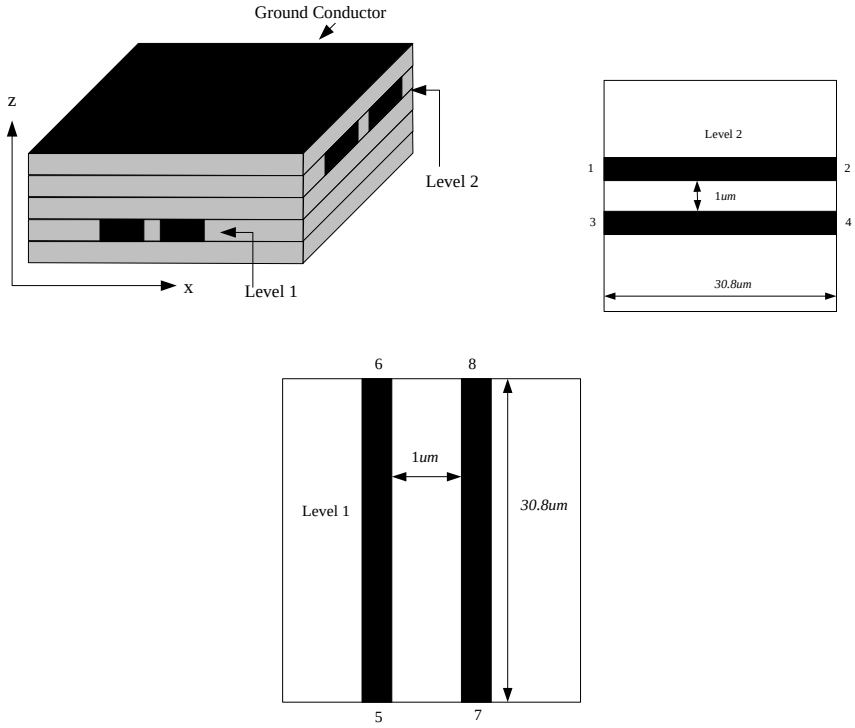

Figure 4.6.1 Multilevel crossover in VLSI interconnect.

In the ADI-FDTD modeling, the computational domain is meshed with cell sizes $\Delta x = \Delta y = \Delta z = 0.2$ μm. The maximum time step size for CFL condition is 0.38 fs. The PML medium with ten layers is employed to truncate the computational domain. The total computational domain is $174 \times 174 \times 45$. For the ADI-FDTD simulation, the CFLN = 10 and CFLN = 20 are used and the corresponding time step size are 3.8 fs and 7.6 fs, respectively.

The simulation results are shown in Fig. 4.6.2 and Fig. 4.6.3 First, the conventional ADI-FDTD with Berenger's PML is studied. As shown in Fig 4.6.2, it can be found that the numerical results will become unstable after running 4800 time step. By employing the modified PML conductivity profile with $m = 1.5$ and $\sigma_{max} = 21.22$S/m for this scheme [45], the instability of this scheme can be improved, as shown in Fig. 4.6.3. We have also extended the running time to 10000 time steps and no instability is observed.

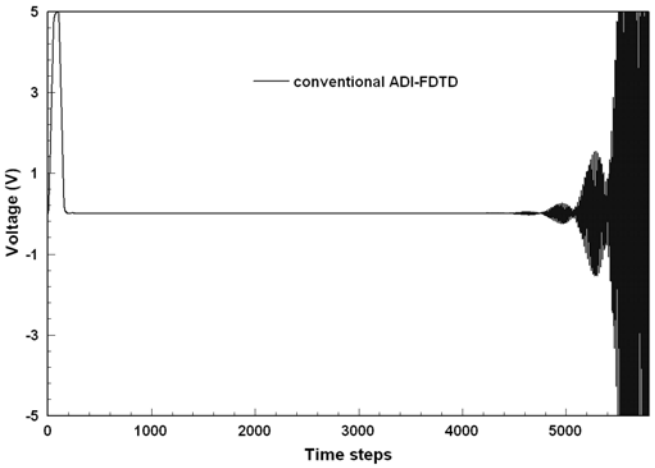

Figure 4.6.2 Voltage at Port 1 with the conventional PML conductivity profile.

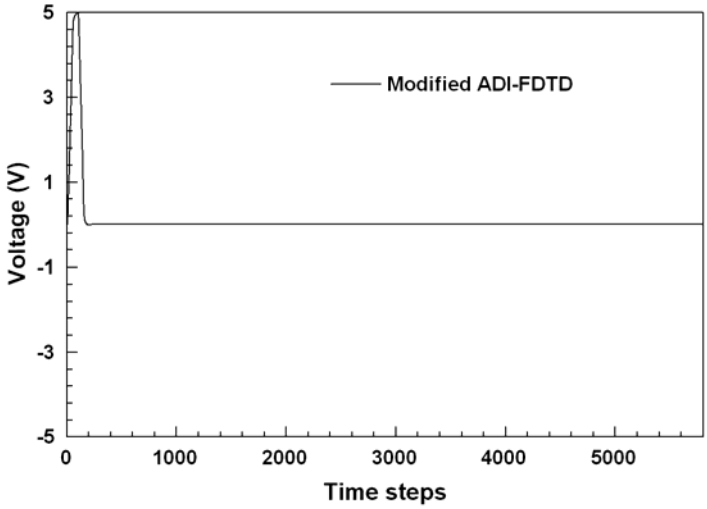

Figure 4.6.3 Voltage at Port 1 with the modified PML conductivity profile.

The coupling effect of the multilevel crossover is investigated by employing the ADI-FDTD method with modified PML conductivity profile. The excitation pulse is trapezoidal with rise time and fall time $\tau_r = \tau_f$ = 380 fs and on-time τ_{on} =380 fs. The simulation result is shown in Fig. 4.3.4. The numerical result of the ADI-FDTD method is similar to that of the FDTD method even CFLN = 20. It is found that there is considerable coupling between the lines in the same level and different levels. The coupled signal amplitudes are near 10% of that of the incident pulse. This shows good match between our result and the result in [44].

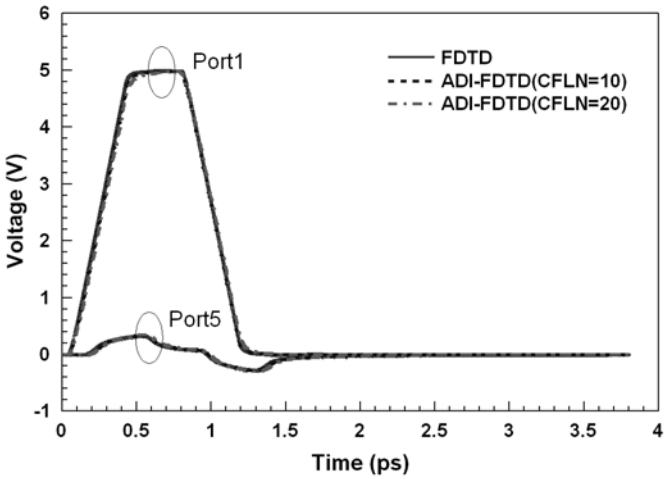

Figure 4.6.4 Voltages at different ports of the multilevel crossover.

The time step size, total time steps, and the CPU time ratio are shown in Table 4.6. Since the time step size is set 10 and 20 times as larger as that of the FDTD method, the total time steps can be reduced. The require memory for the ADI-FDTD method is about 1.9 times as large as that for the conventional FDTD method because of the extra electromagnetic components for two updating steps. Compared to the FDTD method, the CPU time can be reduced to 56.1% and 26.9% for CFLN = 10 and CFLN = 20, respectively.

.

Table 4.7

Multilevel crossover simulation

	Δt	Steps	CPU Time Ratio
FDTD	0.38fs	10000	1.000
ADI-FDTD ($10\Delta t_{max}$)	3.8fs	1000	0.561
ADI-FDTD ($20\Delta t_{max}$)	7.6fs	500	0.269

4.6.2 RF Inductor

Simulations of the VLSI circuit by ADI-FDTD method are performed. A five-turn spiral inductor [46] is studied by the ADI-FDTD method. A cross sectional view of a portion of the structure is illustrated in Fig 4.6.5. The substrate and metal parameters are shown in Table 4.7. The outer dimension is 250 μm, the top conductor microstrip is 8 um wide, and the spacing between conductors is 2.8 μm. The inner space between coupled lines is 150 μm.

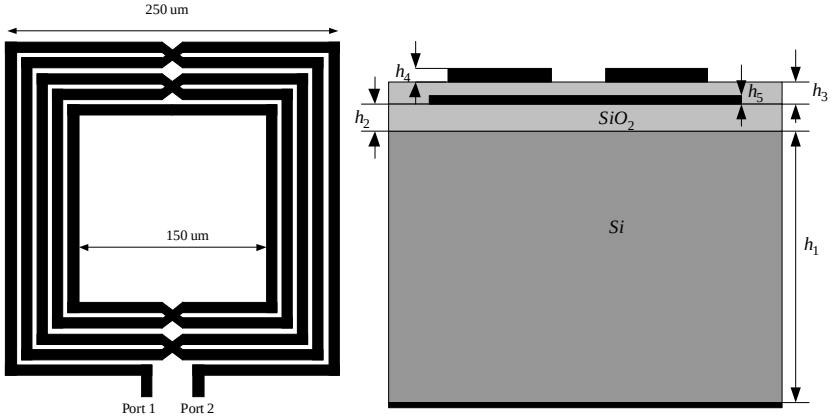

Figure 4.6.5 Cross section view and layout of the spiral inductor with h_3-h_5 = 1.3 μm, h_2 = 3.6 μm, h_1= 200 um, h_4= 2.07 μm, and h_5= 0.84 μm.

Table 4.8
Substrate and metal parameters

Parameter	Value
Oxide thickness over M2,h3-h6	1.3μm
Oxide thickness below M2,h2	3.61 μm
Silicon resistivity	15 Ω-μm
Silicon thickness, h1	200 μm
Metal resistivity	31 mΩ-μm
M3 thickness, h4	2.07 μm
M2 thickness, h5	0.84 μm

For single-ended excitation, Port 2 is grounded. The frequency domain characteristic of the RF inductor can be obtained from the Fourier transform of the time domain transient waveform. The quality factor of the inductor is defined by

$$Q = \frac{2\pi fL}{\mathrm{Re}\left[Z_{input}\right]} \tag{4.6.1}$$

where Z_{input} is the series equivalent input impedance.

In the ADI-FDTD simulation, the cell sizes in the *x*- and *y*-directions are $\Delta x = \Delta y =$ 1.35 μm. We use the nonuniform cells in the *z*-direction to reduce the computational domain and model the fine geometry. The nonuniform cell sizes in z-direction are 3.0 μm, 1.5 μm, and 1.2 μm, respectively. The CFL stability condition is $\Delta t_{max} \leq 2.5$ *fs*. We choose CFLN = 20 and the corresponding time step size $\Delta t = 50$ *fs*.

Since we will study the Q- factor in frequency domain, the total number of the time steps for ADI-FDTD simulation is around 25000 time steps when CFNL = 20 is used. If the conventional FDTD method is used to analyze this inductor, the total time steps will be 5×10^5 and it will be difficult to complete the simulation. When the conventional PML conductivity profile is used for ADI-FDTD method, the numerical results will be unstable after running 1000 time steps. In section 4.2, we find that the ratio of the successive magnetic conductivity should be small to prevent the instability. To validate this viewpoint, the homogeneous PML medium $\sigma_x = \sigma_y = \sigma_{max}$ is employed for the ADI-FDTD to analyze the spiral inductor. The simulation result shows that no instability is observed after running 25000 time steps and the time-domain waveforms are Fourier transformed to obtain the frequency domain result. Comparisons between the experimental measurement and simulation result for Q-factor are shown in Fig. 4.6.6. At frequencies below 2.5 GHz, the simulation results of the Q-factor between measurement and simulation result are matched well. From the measurement result, the peak Q-factor is 6.6 at 1.6 GHz. Our simulation shows that the peak Q is 6.3 at 1.6 GHz, which is similar to the measurement result.

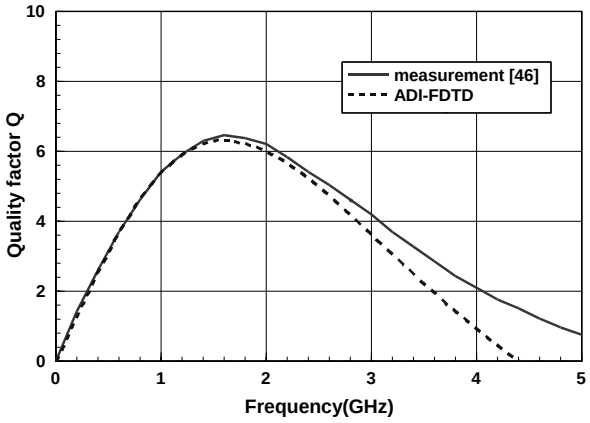

Fig. 4.6.6 Measured and simulated Q-factor

4.7 Discussion

In this work, the stability analysis of the Mur's ABC in the ADI-FDTD is studied. The stability analysis is performed by deriving the amplification matrix of this scheme. The stability of this scheme with different propagation directions and different time step size is investigated. From the stability analysis, we find the eigenvalues of this

scheme will be smaller than unity when the propagation directions are at $\phi = 0^o$, 45^o, and 90^o and will become unstable at other propagation directions. The numerical dispersion relation of the Mur's ABC in ADI-FDTD is derived analytically from amplification matrix. We find that the numerical errors of this scheme are significantly affected by the propagation directions and time step size. We also perform numerical simulations of 3-D ADI-FDTD method to validate the instability of this scheme. On the other hand, the stability analysis of the ADI-FDTD method with split-field PML mediums is studied. It is found that this scheme will be unstable at the vacuum-PML interface and inside the PML regions. The instability of this scheme inside the PML regions can be improved with the modified conductivity profile. The theoretical results are validated from numerical simulations. The stability analysis of the split-field PML and unsplit-field PML CFS PML schemes for the ADI-FDTD and CN-FDTD are studied. The ADI-FDTD can be seen as a second order perturbation of the CN-FDTD method. From the stability analysis, we find that the Δt^2 perturbation term can affect the stability of the PML schemes for ADI-FDTD.

The modified PML conductivity profile is used to improve the stability of the ADI-FDTD with PML absorber. The multilevel crossover in VLSI circuit and RF inductor are studied by ADI-FDTD method. Compared to the conventional FDTD simulation, a significant reduction in calculation time can be achieved. Although the PML performance will be affected by the modified PML conductivity profile, it can be found that the simulation results are matched quite well with the reference results. The modified scheme can provide an efficient and accurate electromagnetic simulation method for VLSI circuits.

Chapter 5

Isolation Enhancement Between Two Packed Antennas with Coupling Element

This paper introduces a coupling element to enhance the isolation between two closely packed antennas for 2.4 GHz wireless local area network (WLAN) application. The proposed structure occupies two antenna elements and a coupling element in between. By putting a coupling element which artificially creates an additional coupling path between the antenna elements, the antenna isolation can be enhanced. The advantage of this design is that no extra space is needed for antenna elements. With the proposed design, more than 15 dB isolation can be achieved for two parallel individual planar inverted F antennas (PIFAs) with 5 mm spacing. Parametric studies for the design are also included to show how to increase isolation bandwidth and control the isolation frequency.

5.1 Antenna Design

The details of our proposed design are shown in Fig. 5.1.1. It can be seen that two identical PIFA antenna elements operated at 2.4 GHz are integrated on a low cost FR4 substrate with a PCB thickness of 1.6 mm and relative permittivity is 4.3. Their edge-to-edge separation is just 5 mm (0.04 λ_0). The PIFAs are located on the top left hand side and right hand side of the PCB respectively and the resonant length is approximately a quarter wavelength. The coupling element is introduced for enhancing isolation. It is located between the two PIFA antenna elements and occupied the dimension of 5 × 13 mm^2. The proposed coupling element is formed by a coupling pad and a thin wire connected to backside ground. The advantage of this design is that no extra space is needed for antenna elements. The concept for isolation enhancement with this design is discussed briefly below.

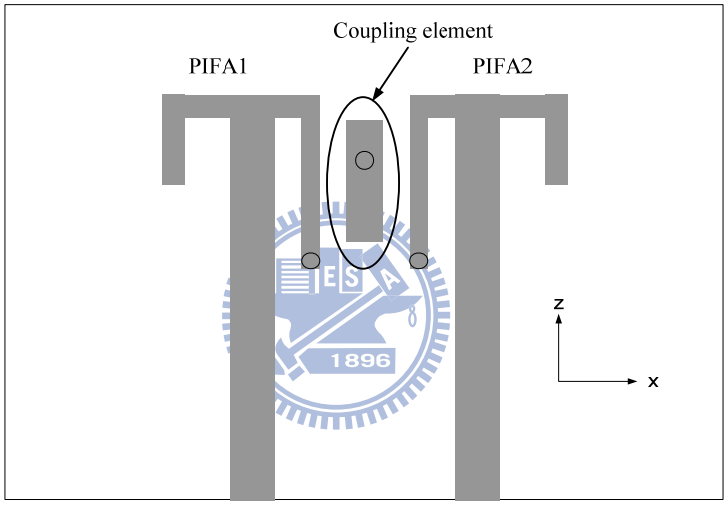

(a) front side

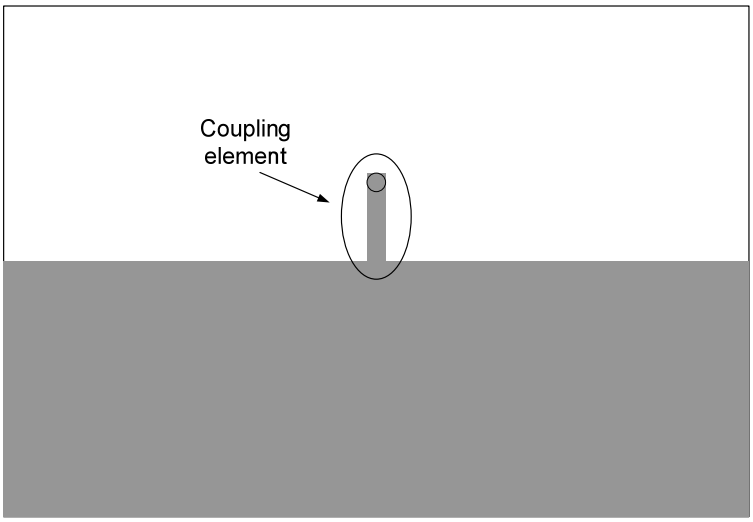

(b) back side

Fig. 5.1.1 Geometry of two PIFAs using coupling element for isolation enhancement

Assume the excited current is fed into PIFA 1. Since PIFA 2 is placed very close to PIFA 1, the strong coupled current on PIFA 2 is approximately 180 degree out of phase with the excited current. The proposed coupling element is placed between the two PIFAs. In this condition, the coupling starts from PIFA 1, through to the coupling element, which, in turn, couples to PIFA 2. The coupled current on coupling element is approximately in phase with excited current on PIFA 1. If the coupling element in this path is adjusted properly, the two coupled currents can be cancelled out so that the overall resultant coupled current is cancelled. The addition of the coupling element will reduce the current in the original PIFA 1, by a similar coupling process. Therefore this design will also affect the self-impedance of the antennas. As long as the cancellation coupling is not too large, this effect can be handled by adjusting the antenna matching appropriately.

5.2 Parametric study of coupling element

We have performed the parametric studies and they explain how to control the center frequency, bandwidth, and level of isolation. The coupling element structure will significantly impact isolation improvement. The circuit model of the proposed design is shown in Fig. 5.2.1. The L_s and C_s are the ground inductance and self capacitance of the coupling element. The L_m and C_m represent the mutual inductance and mutual capacitance between the PIFA and the coupling element. The parameters of the equivalent circuit are studied. The capacitance C_m and ground inductance L_s will significantly affect the isolation level and bandwidth. In this study, L_m and C_s are fixed as 1.5 nH and 0.2 pF, respectively. First, the C_m = 0.25 pF and L_s = 6 nH are used for operation at 2.4 GHz band. The simulated S_{11} is shown in Fig. 5.2.2. The increase of the mutual capacitance and reduce the ground inductance are considered. The C_m and L_s are changed to be 0.45 pF and 4 nH, respectively. From this circuit model, it is found that the bandwidth of the coupling element can be improved with increasing the mutual capacitance.

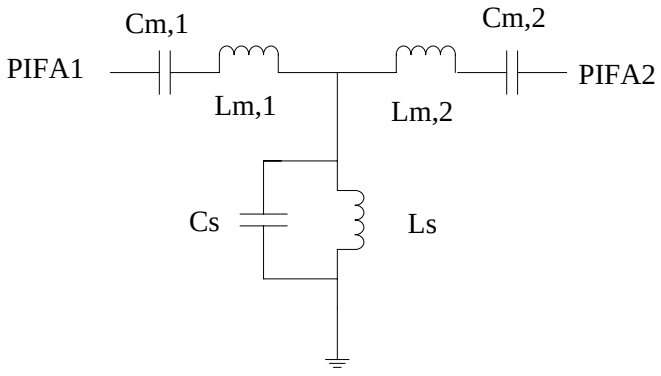

Fig. 5.2.1. Equivalent circuit model of the coupling element.

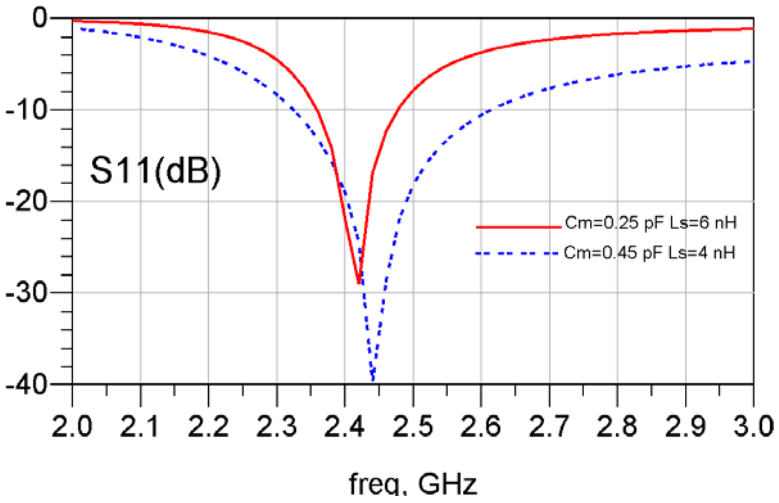

Fig. 5.2.2. Simulated S parameters for equivalent circuit model.

Increasing the bandwidth of the coupling element will also increase the isolation level. The reason is that increase the capacitance will increase the field strength of the coupling element and which cancels out the mutual coupling between antenna elements and thus enhances the isolation. To verify the effect of isolation bandwidth improvement, the antenna structure of Fig. 5.2.3 is studied. By controlling the size of the coupling pad and thin wire, the coupling element can be operated at 2.4 GHz WLAN band. The details geometry of the coupling element is shown in Fig. 5.2.3. For the initial design, the geometry parameters L_1 = 7 mm, W_1= 1 mm, L_2 = 9.5mm, and W_2 = 2.6 mm. The corresponding gap *s* between coupling element and PIFA is 1.2 mm. The coupling element is then modified to increase the capacitance between antenna and coupling element. The width of the ground wire W_1 is also increased to reduce the ground inductance for operation at 2.4 GHz. The proposed design with L_1 = 5.9 mm, W_1= 4 mm, L_2 = 9.1 mm, and W_2 = 4.5 mm is studied. The gap *s* is changed to be 0.25 mm. The simulated isolation for the proposed design is shown in Fig. 5.2.3. The results are compared with reference antenna elements without coupling element. From the simulation results, it is found the bandwidth of this design can be significantly improved and the isolation can be below -15 dB for 2.4 GHz WLAN band.

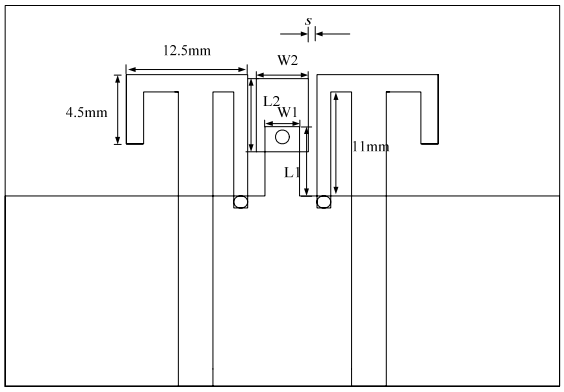

(a)

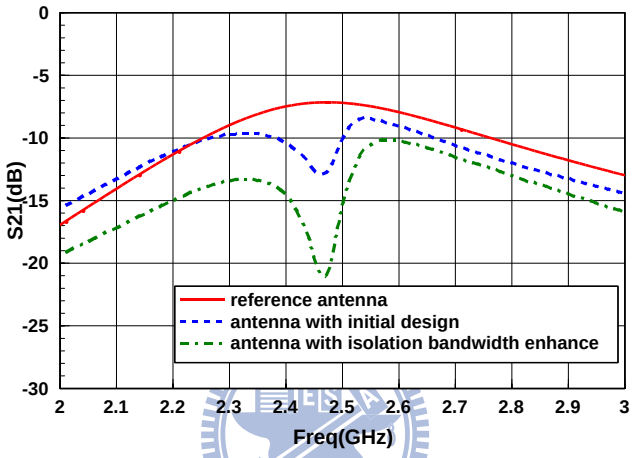

(b)

Fig. 5.2.3. (a) Proposed design for isolation bandwidth enhancement. (b) Simulated S parameters for the proposed design.

The parametric study is based on the geometry given in Fig. 5.2.3. Referring to Fig. 5.2.3, the coupling element has two key parameters which we refer to the L_1 and L_2 as labeled on Fig. 5.2.3. We simulate the proposed structure in Fig. 5.2.3 and vary these two parameters to understand how to control the structure. For the studies on the effect of L_1, firstly we fix the value L_2 and vary the L_1 from 5.3 mm to 5.9 mm. Increasing L_1 will increase the parasitic inductance. In Fig. 5.2.4, we can observe that the position of the maximum isolation shifts to a lower frequency when the L_1 increases. Secondly we fix the value of L_1 and vary L_2 from 9.1 mm to 8.0 mm. The parasitic capacitance between coupling element and antennas will be deceased after decreasing L_2 length. In Fig. 5.2.4, we can observe that the position of the maximum isolation shifts to higher frequency when the L_2 decreases. From the result, we can notice that both the L_1 and L_2 have a significant effect on the position of maximum isolation. It is found that they control the resonant length of the coupling element and shifts the position of maximum isolation in the frequency range.

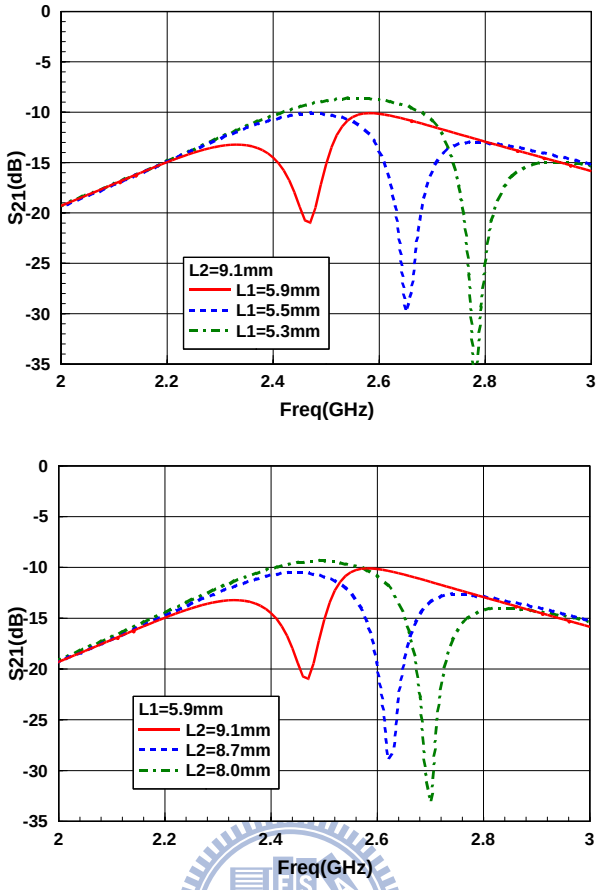

Fig. 5.2.4 Parametric study of the coupling element.

5.3 Simulated and Measured Results

From measurement, the isolation between the two PIFA antennas is -8 dB at 2.45 GHz for the reference antenna without coupling element. With the proposed coupling element occupied between the PIFAs, a maximum isolation below -22 dB for 2.4 GHz WLAN band can be obtained. Although there is a slight frequency shift of the S_{11}, this effect can be compensated by modifying the antenna length. According to the measurement result, it shows that the antenna isolation can be below -15 dB from 2.4 GHz to 2.5 GHz.

The FDTD is employed for antenna simulation. In this simulation, the FDTD parameters $\Delta x = 0.3$ mm, $\Delta y = 0.5$ mm, $\Delta z = 0.8$ mm, and $\Delta t = 0.8$ ps are used. Ten layer PML is employed for boundary condition. The simulation is performed 10000 time step to allow field convergence. The simulated S parameters of FDTD are compared with HFSS simulation and measurement results as shown in Fig. 5.3.2. From FDTD simulation, -10dB insertion loss and -15dB isolation can be observed from 2.4GHz to 2.5GHz.

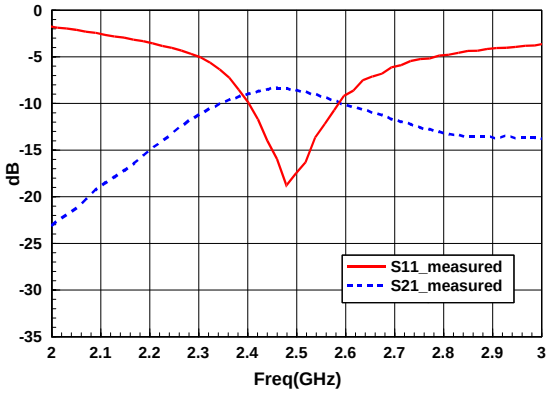

Fig. 5.3.1 Measured S parameters for the reference antenna elements.

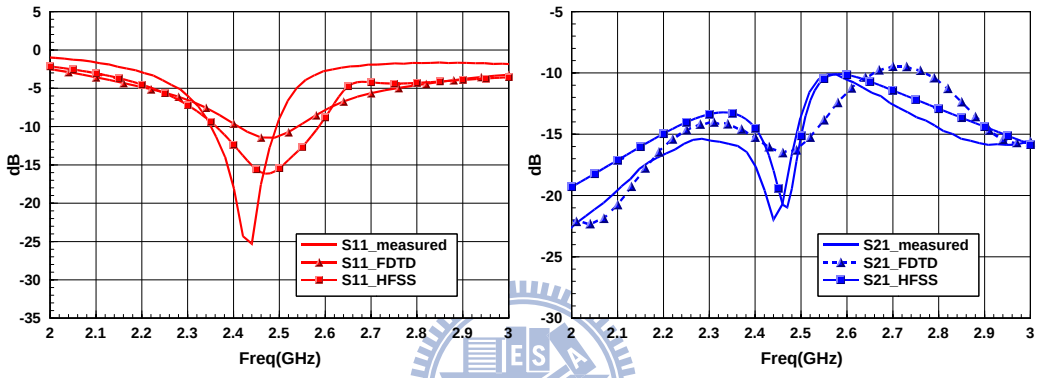

Fig. 5.3.2 Simulated and measured S parameters of the proposed design with isolation enhancement.

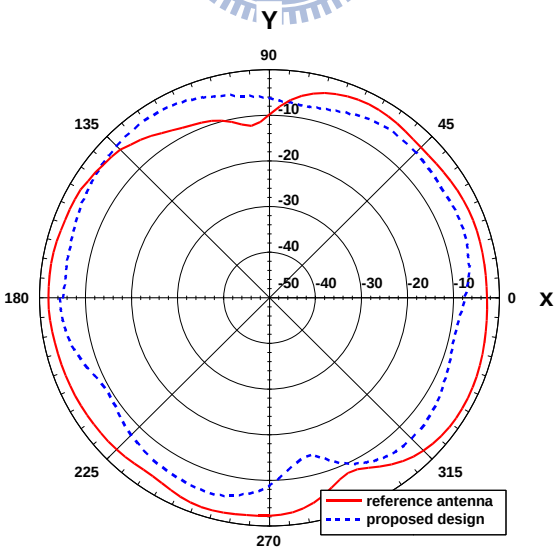

Fig. 5.3.3 Radiation pattern comparison

To further confirm the performance of the design, the antenna gain pattern is also carried out. The measured antenna patterns for exciting port 1 (left Port) at 2.4 GHz is shown in Fig. 5.3.2. The peak gain for the reference antenna and the proposed design

are -1.93 dB and -2.5 dB, respectively. Although the antenna pattern will be somewhat affected with the additional coupling element, the maximum antenna gain can be less affected with the proposed design.

5.4 Discussion

In this paper, a coupling element to enhance isolation for closely packed antennas operating at 2.4 GHz WLAN band is proposed. We artificially create an additional coupling path by utilizing a coupling element to enhance the coupling between the antenna elements. The concept of improving isolation for proposed coupling element is discussed. The antenna isolation below -15 dB can be achieved with their spacing just 5 mm. The parameters of the proposed coupling element are evaluated to control the frequency band of the maximum isolation, peak isolation and the bandwidth of the transmission reduction.

Chapter 6

Conclusion

The basic finite difference time domain (FDTD) method including the absorbing boundary conditions (ABCs), near field to far field transformation, and lumped elements modeling are introduced in Chapter 2. The specific absorption rate (SAR) reduction in the human head with metamaterials is studied. The human head model in this study is obtained from discretization of the MRI human head model and the peak SAR value in the human head is calculated by FDTD method. To study the electromagnetic characteristics of metamaterials, the FDTD with Drude model is developed. From our study, we find that the placement of metamaterials between the antenna and human head can reduce the peak SAR in the human head. The effects of medium parameter, placement location, and size of metamaterials on SAR reduction efficiency and antenna radiation power are discussed in Chapter 3. The metamaterials can be designed at cellular phone operation frequency. In this study, we also design split ring resonators (SRRs) to operate at 900 MHz and 1800 MHz. The operation frequency of SRR is affected by the structure parameters. The detail of the SRR design procedure is also described in Chapter 3. When placing the designed SRRs between the antenna and dielectric cube, it is found that the peak SAR in the dielectric cube can be reduced significantly. The simulation results of SAR reduction with SRRs can validate previous SAR reduction studies by FDTD method with Drude model. The developed method for metamaterials simulation can be used for designing and studying the electromagnetic characteristics of metamaterials in the future work. The SAR reduction with metamaterials can provide helpful information for cellular phone design to meet the safety regulation.

We also develop the ADI-FDTD method. However, when employing the ABCs for ADI-FDTD method, it can cause instability problem. First, the stability analysis of the Mur's first order ABC for ADI-FDTD is investigated. The effect of wave propagation direction and different time step size on the stability of this scheme is studied. It is found that the Mur's first order ABC can also lead to instability. The numerical dispersion relation of this scheme is demonstrated. Then, we study the stability of split-field perfect matched layer (PML) for ADI-FDTD method. The amplification matrix of this scheme is derived with considering different PML conductivity profiles. From the theoretical analysis and numerical simulation, it is found that the split-field

PML for ADI-FDTD method can lead to unstable condition. The effect of the PML conductivity profile on this scheme is investigated. We propose the modified PML conductivity profile to improve the instability of split-field PML for ADI-FDTD method. The ADI-FDTD method can be seen as a second order perturbation of the Crank-Nicolson FDTD (CN-FDTD) scheme. The CN-FDTD can remain unconditionally stable with PML implementation. The stability of split-field PML and unsplit-field PML schemes for ADI-FDTD and CN-FDTD is studied. It is found that the PML equations for ADI-FDTD method will be unstable due to the perturbation term. The stability studies of CN-FDTD and ADI-FDTD can provide information to develop a stable PML scheme for ADI-FDTD in future work.

Finally, we use the proposed modified ADI-FDTD PML scheme to study the time domain and frequency domain characteristics of VLSI circuits. The multilevel crossover of VLSI circuit and high frequency RF inductor are studied. From simulation results, it is found that the proposed scheme can model the VLSI circuits accurately and efficiently.

In this work, a coupling element to enhance isolation for closely packed antennas operating at 2.4 GHz WLAN band is proposed. We artificially create an additional coupling path by utilizing a coupling element to enhance the coupling between the antenna elements. The concept of improving isolation for proposed coupling element is discussed. The antenna isolation below -15 dB can be achieved with their spacing just 5 mm. The parameters of the proposed coupling element are evaluated to control the frequency band of the maximum isolation, peak isolation and the bandwidth of the transmission reduction.

Bibliography

[1] IEEE C95.1-1991, "IEEE Standard for Safety Levels with Respect to Human Exposure to Radio Frequency Electromagnetic Fields, 3kHz to 300GHz," Institute of Electrical and Electronics Engineers, Inc. New York, 1992.

[2] International Non-Ionizing Radiation Committee of the International Radiation Protection Association, "Guidelines on limits of exposure to radiofrequency electromagnetic fields in the frequency range from 100KHz to 300GHz," *Health Physics*, vol. 54: 1, pp. 115-123, 1988.

[3] J. Wang and O. Fujiwara, "FDTD computation of temperature rise in the human head for portable telephones," *IEEE Trans. Microw. Theory Tech.*, vol. 47, no. 8, pp. 1528-1534, Aug. 1999.

[4] C. M. Kuo and C. W. Kuo, "SAR distribution and temperature increase in the human head for mobile communication," in *IEEE Int. Antennas Propagation Symp. Dig.*, Columbus, Ohio, Jun. 2003, pp. 1025-1028.

[5] J. Wang and O. Fujiwara, "Reduction of electromagnetic absorption in the human head for portable telephones by a ferrite sheet attachment," *IEICE Trans. Communicat.*, vol. E80B, no.12, pp.1810-1815, Dec 1997.

[6] A. Hirata, T. Adachi, and T. Shiozawa, "Folded-loop antenna with a reflector for mobile handsets at 2.0 GHz," *Microw. Opt. Technol. Lett.*, vol.40, no.4, pp.272-275, Feb. 2004.

[7] K. H. Chan, K. M. Chow, L. C. Fung, and S. W. Leung, "Effects of using conductive materials for SAR reduction in mobile phones," *Microw. Opt. Technol. Lett.*, vol.44, no.2, pp.140-144, Jan, 2005.

[8] E. Ozbay, K. Aydin, E. Cubukcu, and M. Bayindir, "Transmission and reflection properties of composite double negative metamaterials in free space," *IEEE Trans. Antenna and Propagat.*, vol. 51, no. 10, pp. 2592-2595, Oct. 2003.

[9] R. W. Ziolkowski, "Design, fabrication, and testing of double negative metamaterials", *IEEE Trans. Antenna and Propagat.*, vol. 51, no. 7, pp. 1516-1529, July. 2003.

[10] M. M. Sigalas, C. T. Chan, K. M. Ho, and C. M. Soukoulis, "Metallic photonic band gap materials," *Phys. Rev. B*, vol. 52, no. 16, pp. 11744-11751, Oct. 1995.

[11] J. B. Pendry, A. J. Holen, D. J. Robbins, and W. J. Stewart, "Magnetism from conductors and enhanced nonlinear phenomena," *IEEE Trans. Microw. Theory Tech.*, vol. 47, no.11, pp. 2075-2084, Nov. 1999.

[12] J. N. Hwang and F. C. Chen, “Reduction of the SAR distribution with metamaterials,” in *Proc. 16th Asia Pacific Microw. Conf.*, New Dehli, India, Dec. 2004, pp. 414-415.

[13] R. W. Ziolkowski and E. Heyman, “Wave propagation in media having negative permittivity and permeability,” *Phys. Rev. E*, vol. 64, pp. 1-15, Oct. 2001.

[14] N. Engheta, and R. W. Ziolkowski, “A positive future for double-negative metamaterials,” *IEEE Trans. Microw. Theory Tech.*, vol. 53, no. 4, pp. 1535-1556, Apr. 2005.

[15] D. Correia and J. M. Jin, “3-D-FDTD-PML analysis of left-handed metamaterials,” *Microw. Opt. Technol. Lett.*, vol. 40, no. 3, pp. 201-205, Feb. 2004.

[16] K. S. Yee, “Numerical solution of initial boundary value problems involving Maxwell’s equations in isotropic media,” *IEEE Trans. Antennas Propagat*., vol. AP-14, no. 3, pp. 302-307, May 1966.

[17] A. Taflove and S. Hagness, *Computational Electrodynamics :The Finite-Difference Time-Domain Method*, 3nd ed. Boston, MA: Artech House, 2005.

[18] T. Namiki, “A new FDTD algorithm based on alternating-direction implicit method,” *IEEE Trans. Microw. Theory Tech*., vol. 47, no. 10, pp. 2003-2007, Oct. 1999.

[19] F. Zheng, Z. Chen, and J. Zhang, “A finite-difference time-domain method without Courant stability conditions,” *IEEE Microw. Guided Wave Lett*., vol. 9, no.11, pp. 441-443, Nov. 1999.

[20] F. Zheng, Z. Chen, and J. Zhang, “Toward the development of a three-dimensional unconditionally stable finite-difference t time-domain method,” *IEEE Trans. Microw. Theory Tech*., vol. 48, no. 9, pp. 1550-1558, Sep. 2000.

[21] T. Namiki, “3-D ADI-FDTD method-unconditionally stable time-domain algorithm for solving full vector Maxwell’s equations,” *IEEE Trans. Microw. Theory Tech*., vol. 48, no. 10, pp. 1743-1748, Oct. 2000.

[22] Y. Yang, R. S. Chen, W. C. Tang, K. Sha, and E. K. N. Yung, “Analysis of planar circuits using an unconditionally stable 3D ADI-FDTD method,” *Microw. Opt. Technol. Lett.*, vol.46, no.2, pp.175-179, July, 2005.

[23] T. Namiki and K. Ito, “Numerical simulation of microstrip resonators and filters using ADI-FDTD method,” *IEEE Trans. Microw. Theory Tech*., vol. 49, no. 4, pp. 665-670, Apr. 2001.

[24] J. P. Berenger, “A perfectly matched layer for the absorbing of electromagnetic waves,” *J. Comp. Phys*., vol. 114, no. 1, pp. 185-200, Oct, 1994.

[25] G. Liu and S. D Gedney, “Perfectly matched layer media for an unconditionally stable three-dimensional ADI-FDTD method,” *IEEE Microw. Guided Wave Lett.*, vol. 10, no. 7, pp. 261-263, July 2000.

[26] C. C.-P. Chen, T.-W. Lee, N. Murugensan, and S. C. Hagness, “Generalized FDTD-ADI: an unconditionally stable full-wave Maxwell’s equations solver for VLSI interconnect modeling,” in *Proc. Int. Conf. Computer-Aided Design*, San Jose, CA, Nov. 2000, pp. 156-163.

[27] M. H. Kermani and O. M. Ramahi, “Instable 3D ADI-FDTD open-region simulation,” in *IEEE Int. Antennas Propagation Symp. Dig.*, Washington DC, July, 2005, pp. 142-145.

[28] R. G. Rubio, S. G. Garcia, A. R. Bretones, and R. G. Martin, “An unsplit Berenger-Like PML for the ADI-FDTD method,” *Microw. Opt. Technol. Lett.*, vol.42, no.6, pp. 466-469, Sep, 2004.

[29] J.-N. Hwang and F.-C. Chen, “A rigorous stability analysis of instability in ADI-FDTD method with PML absorber,” in *IEEE Int. Antennas Propagation Symp. Dig.*, Albuquerque, New Mexico, July. 2006, pp. 1739-1742.

[30] J.-N. Hwang and F.-C. Chen, “A modified PML conductivity profile for the ADI-FDTD Method with split-field PML,” *IEE Proc.- Microw. Antennas Propag.*, accepted.

[31] R. G. Rubio, S. G. Garcia, A. R. Bretones, and R. G. Martin, “Crank-Nicolson reformulation of ADI-FDTD PML extensions,” *Antennas Wireless Propaga. Lett.*, vol. 5, pp. 357-360, 2006.

[32] D. Wu and J. Chen, “Perfectly matched layer for Crank-Nicolson (CN) FDTD method,” in *IEEE Int. Antennas Propagation Symp. Dig.*, Monterey, CA, Jun. 2004, pp. 583-586

[33] O. Ramadan. “Unconditionally stable Crank-Nicolson nearly PML algorithm for truncating linear Lorentz dispersive FDTD domains,” *IEEE Trans. Microw. Theory Tech.*, vol. 54, no. 6, pp. 2807-2812, June. 2006.

[34] Mur, G., “Absorbing boundary conditions for the finite-difference approximation of the time-domain electromagnetic field equations,” *IEEE Trans. Electromagn. Compat.*, vol. 23, no. 4, pp. 377-382, 1981.

[35] O. M. Ramahi, “Near- and far-field calculations in FDTD simulations using Kirchhoff surface integral representation,” *IEEE Trans. Antenna and Propagat.*, vol. 45, no 5. pp. 753-759, May. 1997.

[36] W. Sui, D. A. Christen, and C. H. Durney, “Extending the two-dimensional FDTD method to hybrid electromagnetic systems with active and passive lumped elements,” *IEEE Trans. Microw. Theory Tech.*, vol. 40, no. 4, pp. 724-730, April. 1992.

[37] M. Piket-May, A. Taflove, and J. Baron, "FDTD modeling of digital signal propagation in 3-D circuits with passive and active loads," *IEEE Trans. Microw. Theory Tech.*, vol. 42, no. 8, pp. 1514-1523, Aug. 1994.

[38] P. Bernardi, M. Cavagnaro, and S. Pisa, "Evaluation of the SAR distribution in the human head for cellular phones used in a partially closed environment," *IEEE Trans. Electromagn. Compat.*, vol. 38, no. 3, pp. 357-366, Aug. 1996.

[39] M. Bayindir, K. Aydin, and E. Ozbay, "Transmission properties of composite metamaterials in free space," *Appl. Phys. lett.*, vol. 81, no. 1, pp. 120-122, July, 2002.

[40] D. R. Smith, W. J. Padilla, D. C. Vier, S.C. Nemat-Nasser, and S. Schultz, "Composite medium with simultaneously negative permeability and permittivity," *Phys. Rev. lett.*, vol. 84, no. 18, pp. 4184-4187, May. 2000.

[41] D. Sievenpiper, "High-impedance electromagnetic surfaces with a forbidden frequency band," *IEEE Trans. Microw. Theory Tech.*, vol. 47, no. 11, pp. 2059-2074, Nov. 1999.

[42] R. Coccioli, F.-R. Yang, K.-P. Ma, and T. Itoh, "A novel tem waveguide using uniplanar compact photonic-bandgap (UC-PBG) structure," *IEEE Trans. Microw. Theory Tech.*, vol. 47, no.11, pp. 2092-2098, Nov. 1999.

[43] A. Erentok, P. L. Luljak, and R. W. Ziolkowski, "Characterization of a volumetric metamaterial realization of an artificial magnetic conductor for antenna applications," *IEEE Trans. Antennas Propag.*, vol. 53, no. 1, pp. 160-172, Jan, 2005.

[44] P. K. Datta, S. Sanyal, and D. Bhattacharya, "Losses in multilevel crossover in VLSI interconnects," in *Proc. of the 15th international conference on VLSI Design*, pp. 142-146, 2002.

[45] J.-N. Hwang and F.-C. Chen, "A modified PML conductivity profile for the ADI-FDTD Method with split-field PML," accepted for *IET Proc.- Microw. Antennas Propag.*

[46] M. Danesh and J. R. Long, "Differentially driven symmetric microstrip inductors," *IEEE Trans. Microw. Theory Tech.*, vol. 50, no. 1, pp. 332-341, Jan. 2002.

[47] High Frequency Structure Simulator (HFSS). Ansoft Corporation Pittsburgh, PA, 2001.